

NASA

Technical

Paper

3112

October 1991

Benchmark Solutions for the Galactic Heavy-Ion Transport Equations With Energy and Spatial Coupling

Barry D. Ganapol,
Lawrence W. Townsend,
Stanley L. Lamkin,
and John W. Wilson

(NASA-TP-3112) BENCHMARK SOLUTIONS FOR THE
GALACTIC HEAVY-ION TRANSPORT EQUATIONS WITH
ENERGY AND SPATIAL COUPLING (NASA) 58 p

CSCL 20A

N92-13756

Unclass

H1/70 0048241

NASA



1991

Benchmark Solutions for the Galactic Heavy-Ion Transport Equations With Energy and Spatial Coupling

Barry D. Ganapol
University of Arizona
Tucson, Arizona

Lawrence W. Townsend
Langley Research Center
Hampton, Virginia

Stanley L. Lamkin
Old Dominion University
Norfolk, Virginia

John W. Wilson
Langley Research Center
Hampton, Virginia

The use of trademarks or names of manufacturers in this report is for accurate reporting and does not constitute an official endorsement, either expressed or implied, of such products or manufacturers by the National Aeronautics and Space Administration.

Abstract

Nontrivial benchmark solutions are developed for the galactic heavy-ion transport equations in the straight-ahead approximation with energy and spatial coupling. Analytical representations of the ion fluxes are obtained for a variety of sources with the assumption that the nuclear interaction parameters are energy independent. The method utilizes an analytical Laplace transform inversion to yield a closed-form representation that is computationally efficient. The flux profiles are then used to predict ion dose profiles, which are important for shield-design studies.

1. Introduction

With our ever-increasing interest in establishing mankind's presence in space, the protection of personnel from energetic radiation in the space environment has become a relevant concern. As high-energy radiation interacts with target nuclei, the ions undergo nuclear fragmentation and energy degradation. This radiation is composed of heavy ions, called galactic cosmic rays (GCR), originating in deep space and/or protons from the Sun. The nuclear fragments generated by direct nuclear impact or electromagnetic dissociation form a secondary radiation field that again interacts with the target nuclei and fragment to add to the biological radiation hazard represented by the incident ions. Thus, to ensure that the habitat in the space environment is properly shielded from energetic radiation, a knowledge of the changing nature of the incident radiation field as it penetrates protective spacecraft shielding is imperative. To anticipate future space shielding requirements, NASA has initiated an effort to formulate computational methods that simulate radiation effects in space. Deterministic transport algorithms have been developed for the Boltzmann equation that describe GCR interactions with nuclei and cause the inevitable changing composition of the incident radiation field while traversing bulk shielding material. An important component of the NASA program is the assessment of the accuracy of proposed deterministic algorithms. For this reason, analytical benchmark solutions to mathematically tractable, galactic cosmic ray problems have recently been developed (refs. 1 and 2). Even though these problems involve some simplifying assumptions of the associated GCR physics, they still contain the essential features of the transport processes. These solutions, when compared with the corresponding numerical results from algorithms, provide assurance of proper programming and a measure of the accuracy of the numerical methods used in the algorithm. The moti-

vation for such comparison is that algorithms developed for realistic problems must also yield reliable results for the less complicated problems.

In this report, the analytical solution to the galactic ion transport (GIT) equations that describe the straight-ahead motion of energetic heavy ions (HZE) is developed for the first time. An analytical representation of the ion fluxes for a variety of sources is obtained with the assumption that the nuclear interaction parameters are energy independent. The method utilizes an analytical Laplace transform inversion which yields a closed-form representation that is also computationally efficient. From the flux profiles, it is then possible to obtain ion dose profiles, which are important for shield design.

In section 2, the analytical solution technique is presented in detail, along with solutions for several source distributions. In section 3, the numerical implementation of the flux and dose profiles is discussed. Results for selected case studies and comparisons are presented in section 4, with special emphasis on understanding the behavior of the ion flux from both the physical and mathematical points of view. The report concludes with a summary and recommendations for future development.

2. Theory

2.1. Galactic Ion Transport Equations

Because of the high energy of the galactic ions (refs. 3 to 5), the straight-ahead approximation can be introduced into the Boltzmann equation with a high degree of confidence. In this approximation, ions are assumed to move without angular deflection; and, as the colliding ions break up in nuclear fragmentation, the fragments continue in the incident ion direction. Thus, for ions of charge number j , the

appropriate transport equation is (ref. 6)

$$\left[\frac{\partial}{\partial x} - \frac{\partial}{\partial E} S_j(E) + \sigma_j(E) \right] \phi_j(x, E) = \sum_{k=j+1}^J M_{jk}(E) \sigma_k(E) \phi_k(x, E) \quad (1a)$$

where ϕ_j is the flux of the j th ion flux at position x with an energy per nucleon of E . The *macroscopic* absorption cross section is σ_j , M_{jk} is the multiplicity of ion j produced in collision with ion k , and S_j is the absolute value of the change in energy E per unit distance traveled. The added assumptions of continuous slowing-down theory and that target ion fragmentation can be neglected have been made in equation (1a). Source ions are assumed incident on a semi-infinite shield with an initial energy distribution of

$$\phi_j(0, E) = f_j(E) \quad (1b)$$

Because of the success of the analytical investigations applied to previous benchmarks (refs. 1 and 2), the analytical approach is again followed here. To make equation (1a) mathematically tractable, the cross sections and multiplicities are assumed to be energy independent. This is a reasonable assumption at high energy. Also, the well-known scaling law for stopping powers at high energies (ref. 6), or

$$S_j(E) = \nu_j S_p(E) \quad (2a)$$

is introduced into equation (1a), where

$$\nu_j \equiv Z_j^2/A_j \quad (2b)$$

and where S_p is the proton stopping power and A_j is the atomic mass of the j th ion. With this substitution, and with the change of variable from energy to proton path length at a given energy $s(E, E_0)$, equations (1) become

$$\left[\frac{\partial}{\partial x} + \nu_j \frac{\partial}{\partial s} + \sigma_j \right] \phi_j(x, s) = \sum_{k=j+1}^J \beta_{jk} \phi_k(x, s) \quad (3a)$$

and

$$\phi_j(0, s) = f_j(s) \quad (3b)$$

where

$$\beta_{jk} \equiv M_{jk} \sigma_k \quad (3c)$$

The path length is given by

$$s(E, E_0) = \int_E^{E_0} dE' / S_p(E') \quad (3d)$$

which, from the definition of the flux distribution, implies

$$\phi_j(x, s) \equiv S_p(E) \phi_j(x, E) \quad (3e)$$

and

$$f_j(s) = S_p(E) f_j(E) \quad (3f)$$

Some readers may be accustomed to seeing the energy variable in equations (1a) and (1b) transformed by using the residual range $R_p(E)$ (refs. 7 and 8), where

$$R_p(E) = \int_0^E \frac{dE'}{S(E')}$$

The variables $R_p(E)$ and $s(E, E_0)$ are directly related. The variable $s(E, E_0)$ is the penetration distance for a proton of initial energy E_0 to reach present energy E ; $R(E)$ is the remaining distance the proton will travel before stopping.

The major difficulty in applying the path-length transformation is in the determination of $s(E, E_0)$ from the energy E by using equation (3d), since an integral must be inverted to return to the energy-dependent flux given by equation (3e). This added inconvenience, however, is readily acceptable because of the enormous simplification offered by the energy path-length transformation. Indeed, equations (3a) and (3b) now closely resemble the energy-independent case considered in reference 1. This similarity suggests that similar solution methods should therefore be adopted.

While the emphasis here is on generating highly accurate benchmark solutions, the only limiting assumption made to obtain equations (3) is that of constant cross sections and multiplicities. Thus, the analytical results to be presented can be of use as a predictive as well as a benchmarking tool to give insight into realistic shield design.

2.2. Analytical Solution for Monoenergetic Source

Initially, the solution will be obtained for a monoenergetic beam source of ions of charge J and energy E_0 ($s = 0$) incident on the semi-infinite shield [$f_j(E) = \delta(E - E_0) \delta_{iJ}$]. For this case, ϕ_j corresponds mathematically to the Green's function, since the source is of the form

$$\phi_j(0, s) = \delta(s) \delta_{iJ} \quad (3g)$$

which translates into the following volume source:

$$Q(x, s) = \delta(s) \delta(x) \delta_{iJ}$$

The Green's function will be used subsequently to generate solutions for more general sources, including beams composed of several different ion types

(composite beams). For the incident ion J and for ion $J - 1$, produced by target fragmentation, equations (3) can be solved analytically. It can be shown that the solutions for ions J and $J - 1$ are as follows:

$$\phi_J(x, s) = \exp(-\sigma_J x) \delta(s - \nu_J x) \quad (4a)$$

$$\begin{aligned} \phi_{J-1}(x, s) = & \frac{\beta_{J-1,J}}{a_1} \left\{ \exp(-\sigma_J x) \right. \\ & \times \exp[-a_1(s - \nu_J x)/b_1] \theta(s - \nu_J x) - \exp(-\sigma_{J-1} x) \\ & \times \exp[-a_1(s - \nu_{J-1} x)/b_1] \theta(s - \nu_{J-1} x) \left. \right\} \end{aligned} \quad (4b)$$

where $a_1 \equiv \sigma_{J-1} - \sigma_J$, $b_1 \equiv \nu_{J-1} - \nu_J$, and $\theta(a)$ is the Heaviside step function. The increased complexity of these solutions relative to the benchmarks considered in reference 2 is clearly evident. Because of the interaction of x and s through the transport operator, a wave of particles in x, s space is induced. The delta function in the expression for ϕ_J represents that wave for the incident ions. The delta function is a mathematical statement required by the continuous slowing-down approximation. For ions of type J to be at a given position x , measured from the surface, they must have traversed a path length s/ν_J exactly. The leading exponential represents the attenuation (loss) of these ions as they fragment into lighter ions along their trajectories. Ion $J - 1$, produced by the fragmentation of ion J , cannot exist before its source (at $x = s/\nu_J$). Also, because of the finite range of a charged particle, ion $J - 1$ cannot travel farther than $x = s/\nu_{J-1}$. Thus, ϕ_{J-1} is nonzero only in the interval $s/\nu_J \leq x \leq s/\nu_{J-1}$, as indicated by equation (4b). This technique is better illustrated in the (x, s) space diagram in figure 1, where the region of nonzero solution is indicated for each ion. The above analysis holds for all ions j produced by fragmentation, and the farthest nonzero solution boundary approaches $s = x$ as j goes to one. The region $x > s$ is forbidden, since no ion has yet traversed a path long enough to get there.

At first glance, one would not attempt to carry on the analytical manipulation necessary to determine the flux for the lower values of j . Fortunately, the analytical results already derived in reference 2 are very useful in pursuing the solution here.

Taking a Laplace transform of s in equations (3a) and (3b) gives

$$\left(\frac{\partial}{\partial x} + \sigma_j + \nu_j p \right) \bar{\phi}_j(x, p) = \sum_{k=j+1}^J \beta_{jk} \bar{\phi}_k(x, p) \quad (5a)$$

$$\bar{\phi}_j(0, p) = \delta_{ij} \quad (5b)$$

where the transform is defined by

$$\bar{\phi}_j(x, p) \equiv \int_0^\infty ds \exp(-sp) \phi(x, s)$$

Treating equations (5a) and (5b) as a set of ordinary differential equations yields the general solution

$$\bar{\phi}_{J-\ell}(x, p) = \sum_{i=0}^{\ell} \alpha_{i,J-\ell}(p) \exp[-(\sigma_{J-i} + \nu_{J-i} p)x] \quad (6a)$$

where the coefficients $\alpha_{i,J-\ell}$ depend on the transformed variable p and are given recursively by (ref. 2)

$$\begin{aligned} \alpha_{i,J-\ell}(p) = & \frac{1}{(\sigma_{J-\ell} - \sigma_{J-i}) - p(\nu_{J-\ell} - \nu_{J-i})} \\ & \times \sum_{k'=i}^{\ell-1} \beta_{J-\ell,J-k'} \alpha_{i,J-k'}(p) \quad (0 \leq i \leq \ell-1) \end{aligned} \quad (6b)$$

and

$$\alpha_{\ell,J-\ell}(p) = - \sum_{i=0}^{\ell-1} \alpha_{i,J-\ell}(p) \quad (6c)$$

The last expression is necessary to satisfy the boundary condition $\bar{\phi}_j(0, p) = 0$ for $1 \leq j \leq J - 1$.

At this point, a numerical inversion procedure could be attempted. Such an attempt, however, would most likely fail, since it is known a priori that the expression for $\bar{\phi}_{J-\ell}$ contains step functions that characterize the spatially discontinuous ion density waves; and in general, numerical inversions fail near such discontinuities. Thus, a numerical inversion will not work well in this case, even for the heavy ions. Therefore, the only other option is to perform the inversion analytically, as was done for ions J and $J - 1$ (eqs. (4a) and (4b)). To do so, however, requires the explicit knowledge of the dependence of $\alpha_{i,J-\ell}$ on p , which will now be determined.

For ion $J - 1$, we have

$$\left. \begin{aligned} \alpha_{0,J}(p) &= 1 \\ \alpha_{0,J-1}(p) &= \frac{Y_{0,1}^{J-1}}{a_{J-1,J} + pb_{J-1,J}} \\ \alpha_{1,J-1}(p) &= \frac{Y_{1,1}^{J-1}}{a_{J-1,J} + pb_{J-1,J}} \end{aligned} \right\} \quad (7a)$$

where

$$\left. \begin{aligned} Y_{0,1}^{J-1} &= \beta_{J-1,J} \\ Y_{1,1}^{J-1} &= \beta_{J-1,J} \\ a_{\ell m} &\equiv \sigma_\ell - \sigma_m \\ b_{\ell m} &\equiv \nu_\ell - \nu_m \end{aligned} \right\} \quad (7b)$$

For $\ell = 2$ and $i = 0$,

$$\alpha_{0,J-2}(p) = \frac{1}{a_{J-2,J} + pb_{J-2,J}} \times \left(\frac{\beta_{J-2,J-1}\beta_{J-1,J}}{a_{J-1,J} + pb_{J-1,J}} + \beta_{J-2,J} \right) \quad (8)$$

Upon using the partial fraction expansion

$$\begin{aligned} & \frac{1}{a_{J-2,J} + pb_{J-2,J}} \frac{1}{a_{J-1,J} + pb_{J-1,J}} \\ &= -\frac{b_{J-2,J}}{a_{J-2,J} b_{J-1,J} - a_{J-1,J} b_{J-2,J}} \Lambda_1(p) \\ &+ \frac{b_{J-1,J}}{a_{J-2,J} b_{J-1,J} - a_{J-1,J} b_{J-2,J}} \Lambda_2(p) \end{aligned}$$

where

$$\Lambda_1(p) \equiv \frac{1}{a_{J-1,J} + pb_{J-1,J}}$$

and

$$\Lambda_2(p) \equiv \frac{1}{a_{J-2,J} + pb_{J-2,J}}$$

we obtain

$$\alpha_{0,J-2}(p) = Y_{1,1}^{J-2} \Lambda_1(p) + Y_{1,2}^{J-2} \Lambda_2(p) \quad (9a)$$

with

$$Y_{1,1}^{J-2} = \frac{b_{J-1,J} \beta_{J-2,J-1} \beta_{J-1,J}}{a_{J-2,J} b_{J-1,J} - a_{J-1,J} b_{J-2,J}} \quad (9b)$$

and

$$Y_{1,2}^{J-2} = \beta_{J-2,J} - \frac{b_{J-2,J} \beta_{J-2,J-1} \beta_{J-1,J}}{a_{J-2,J} b_{J-1,J} - a_{J-1,J} b_{J-2,J}} \quad (9c)$$

The coefficients of $\Lambda_r(p)$ are independent of p . Similarly, for $\alpha_{1,J-2}(p)$ and $\alpha_{2,J-2}(p)$,

$$\alpha_{1,J-2}(p) = Y_{1,1}^{J-2} \Lambda_1(p) + Y_{1,3}^{J-2} \Lambda_3(p) \quad (10a)$$

and

$$\alpha_{2,J-2}(p) = Y_{2,1}^{J-2} \Lambda_1(p) + Y_{2,2}^{J-2} \Lambda_2(p) + Y_{2,3}^{J-2} \Lambda_3(p) \quad (10b)$$

where

$$\Lambda_3(p) \equiv \frac{1}{a_{J-2,J-1} + pb_{J-2,J-1}}$$

It should be noted that Λ_1 is common to both the $\ell = 1$ and $\ell = 2$ α -coefficients. A condensed expression for $\alpha_{i,J-2}$ is therefore

$$\alpha_{i,J-2}(p) = \sum_{r=1}^3 Y_{i,r}^{J-2} \Lambda_r(p) \quad (11)$$

with the Y coefficients set to zero as appropriate. When the last equation is introduced into equations (6b) and (6c) with $j = J - 3$, the following form for $\alpha_{i,J-3}$ is found:

$$\alpha_{i,J-3}(p) = \sum_{r=1}^6 Y_{i,r}^{J-3} \Lambda_r(p) \quad (0 \leq i \leq \ell)$$

where the rule for expansion in partial fractions

$$\Lambda_m(p) \Lambda_n(p) = \chi_{1mn} \Lambda_m(p) + \chi_{2mn} \Lambda_n(p)$$

has been used. Apparently, with each unit increase in ℓ , new terms appear in the expression for $\alpha_{i,J-\ell}(p)$, with the appropriate Y coefficients again set to zero. Thus, the general expression for $\alpha_{i,J-\ell}(p)$ is

$$\alpha_{i,J-\ell}(p) = \sum_{r=1}^{N_\ell} Y_{i,r}^{J-\ell} \Lambda_r(p) \quad (N_\ell \equiv \ell(\ell+1)/2) \quad (12)$$

and the explicit dependence of $\alpha_{i,J-\ell}(p)$ on p has been established. Table I shows how, given an index r , the appropriate values of $a_{m,n}$ and $b_{m,n}$ for the term

$$\Lambda_r(p) = \frac{1}{a_{m,n} + b_{m,n}p}$$

are determined. A general recurrence relation for $Y_{i,r}^{J-\ell}$ is obtained by introducing equation (12) into the relation for $\alpha_{i,J-\ell}(p)$ (eqs. (6b) and (6c)) to yield (after much algebra)

$$Y_{i,r}^{J-\ell} = \hat{\chi}_{1,i,r}^{J-\ell} \sum_{k=J-\ell+1}^{J-i} \beta_{J-\ell,k} Y_{i,r}^k h(N_{J-k} - r) \quad (1 \leq r \leq N_{\ell-1}, \quad 0 \leq i \leq \ell-1) \quad (13a)$$

$$Y_{i,r^*}^{J-\ell} = \sum_{k=J-\ell+1}^{J-i} \beta_{J-\ell,k} \sum_{r=1}^{N_{J-k}} \hat{\chi}_{2,i,r}^{J-\ell} Y_{i,r}^k + \beta_{J-\ell,J} \delta_{i,0} \quad (r^* = N_{\ell-1} + i + 1, \quad 0 \leq i \leq \ell-1) \quad (13b)$$

$$Y_{i,r}^{J-\ell} = 0 \quad (N_{\ell-1} + 1 \leq r \leq N_{\ell-1} + i, \quad N_{\ell-1} + i + 2 \leq r \leq N_{\ell}) \quad (13c)$$

$$Y_{\ell,r}^{J-\ell} = - \sum_{i=0}^{\ell-1} Y_{i,r}^{J-\ell} \quad (1 \leq r \leq N_{\ell}, \quad i = \ell) \quad (13d)$$

where

$$\hat{\chi}_{1,i,r}^{J-\ell} \equiv - \left(\frac{b_{J-\ell,J-i}}{-a_r b_{J-\ell,J-i} + a_{J-\ell,J-i} b_r} \right)$$

$$\hat{\chi}_{2,i,r}^{J-\ell} \equiv \frac{b_r}{-a_r b_{J-\ell,J-i} + a_{J-\ell,J-i} b_r}$$

$$a_r \equiv a_{m(r),n(r)}$$

$$b_r \equiv b_{m(r),n(r)}$$

and

$$h(m) \equiv \begin{cases} 1 & m \geq 0 \\ 0 & m < 0 \end{cases}$$

Interchanging the summations in equation (13b) yields the following further simplification:

$$\begin{aligned} Y_{i,r^*}^{J-\ell} &= \sum_{r=1}^{N_{\ell}} \hat{\chi}_{1,i,r}^{J-\ell} \sum_{k=J-\ell+1}^{J-i} \beta_{J-\ell,k} Y_{i,r}^k h(N_{J-k} - r) + \beta_{J-\ell,J} \delta_{i,0} \\ &= \sum_{r=1}^{N_{\ell-1}} \left(\frac{b_{J-\ell,J-i}}{b_r} \right) Y_{i,r}^{J-\ell} + \beta_{J-\ell,J} \delta_{i,0} \end{aligned} \quad (13e)$$

The final expression for the transform is obtained by substituting equation (12) into equation (6a) as follows:

$$\bar{\phi}_{J-\ell}(x, p) = \sum_{i=0}^{\ell} \exp(-\sigma_{J-i} x) \sum_{r=1}^{N_{\ell}} Y_{i,r}^{J-\ell} \left[\frac{\exp(-\nu_{J-i} x p)}{a_r + b_r p} \right] \quad (14)$$

The inversion is easily performed analytically, since

$$\mathcal{L}_s^{-1} \left[\frac{\exp(-\nu_{J-i} x p)}{a_r + b_r p} \right] = \frac{1}{b_r} \exp \left[-\frac{a_r}{b_r} (s - \nu_{J-i} x) \right] \theta(s - \nu_{J-i} x)$$

to give the following solution for $1 \leq \ell \leq J-1$:

$$\begin{aligned} \phi_{J-\ell}(x, s) &= \sum_{i=0}^{\ell} \exp(-\sigma_{J-i} x) \theta(s - \nu_{J-i} x) \sum_{r=1}^{N_{\ell}} \frac{Y_{i,r}^{J-\ell}}{b_r} \\ &\times \exp \left[-\frac{a_r}{b_r} (s - \nu_{J-i} x) \right] \end{aligned} \quad (15)$$

Thus, a closed-form analytical solution to the GIT equation for constant properties has been derived. A formulation more fundamental and therefore more appropriate for computational purposes is obtained from equation (15).

As mentioned previously, some of the coefficients, $Y_{i,r}^{J-\ell}$, are identically zero in order to write $\alpha_{i,J-\ell}(p)$ as the simple summation of equation (12). This procedure dramatically increases the required computer storage and also increases the potential for the accumulation of roundoff error. These zero coefficients can be conveniently eliminated by noting the physical requirement that

$$\phi_{J-\ell}(x, s) = 0 \quad (16)$$

for $x < s/\nu_J$ and by interchanging the summations in equation (15) to give

$$\begin{aligned} \phi_{J-\ell}(x, s) &= \sum_{r=1}^{N_{\ell}} \frac{\exp(-\frac{a_r}{b_r} s)}{b_r} \sum_{i=0}^{\ell} \\ &\times \exp \left[-\left(\sigma_{J-i} - \frac{a_r}{b_r} \nu_{J-i} \right) x \right] Y_{i,r}^{J-\ell} \theta(s - \nu_{J-i} x) \end{aligned} \quad (17)$$

Equation (16) comes about because ion fragments cannot be produced before the incident ion has traveled to its position ($x = s/\nu_J$) as mandated by the continuous slowing-down theory. Since in most cases of interest, $\nu_J > \nu_{J-1}$ for $1 \leq i \leq \ell$, we have $\phi(x, s) = 0$, where $s > x\nu_J > x\nu_{J-i}$. Also from equation (17),

$$\begin{aligned} 0 &= \sum_{r=1}^{N_{\ell}} \frac{\exp(-\frac{a_r}{b_r} s)}{b_r} \sum_{i=0}^{\ell} \\ &\times \exp \left[-\left(\sigma_{J-i} - \frac{a_r}{b_r} \nu_{J-i} \right) x \right] Y_{i,r}^{J-\ell} \end{aligned} \quad (18)$$

which must hold for all values of x and s that satisfy the above inequality. Equation (18) is trivially satisfied for $x = 0$ as a result of equation (13d) of the

recurrence relations for $Y_{i,r}^{J-\ell}$. For equation (18) to be satisfied in general, the following must hold at each value of r and ℓ , independently of x :

$$\sum_{i=0}^{\ell} \exp \left[-(\sigma_{J-i} - \frac{a_r}{b_r} \nu_{J-i}) x \right] Y_{i,r}^{J-\ell} = 0 \quad (19)$$

One way for equation (19) to be a true statement is for the coefficient of x to be identically zero. This requirement, however, is obviously too restrictive. A second possibility is that the coefficients vanish at several values of i taken in pairs; when this is not the case, $Y_{i,r}^{J-\ell}$ should be zero. It can be observed that

$$\sigma_{J-i_1} - \frac{a_r}{b_r} \nu_{J-i_1} = \sigma_{J-i_2} - \frac{a_r}{b_r} \nu_{J-i_2} \quad (20)$$

for two values of $i(i_1, i_2)$ at each value of r . Also, as required by equation (19),

$$Y_{i_1,r}^{J-\ell} = -Y_{i_2,r}^{J-\ell} \quad (21)$$

values of i_1 and i_2 for $1 \leq r \leq 15$ are given in table II, from which a recognizable pattern emerges.

By introducing equations (20) and (21) into equation (17), the expression for $\phi_{J-\ell}(x, s)$ then becomes

$$\begin{aligned} \phi_{J-\ell}(x, s) = \sum_{r=1}^{N_\ell} \exp(-\frac{a_r}{b_r} s) \exp \left[- \left(\sigma_{J-i_1} + \frac{a_r}{b_r} \nu_{J-i_1} \right) x \right] \\ \times \tilde{Y}_{i_1,r}^{J-\ell} [\theta(s - \nu_{J-i_1} x) - \theta(s - \nu_{J-i_2} x)] \end{aligned} \quad (22a)$$

where

$$\tilde{Y}_{i_1,r}^{J-\ell} \equiv Y_{i_1,r}^{J-\ell} / b_r \quad (22b)$$

The recurrence relation for $\tilde{Y}_{i_1,r}^{J-\ell}$ becomes

$$\tilde{Y}_{i_1,r}^{J-\ell} = \hat{\chi}_{1,i_1,r}^{J-\ell} \sum_{k=J-\ell+1}^{J-i_1} \beta_{J-\ell,k} \tilde{Y}_{i_1,r}^k h(N_{J-k} - r) \quad (23a)$$

for $1 \leq r \leq N_{\ell-1}$ and

$$\tilde{Y}_{i_1,r}^{J-\ell} = \sum_{r'=1}^{N_{\ell-1}} \left(\frac{b_{J-\ell,J-i}}{b_{r'}} \right) P_{r'} \tilde{Y}_{i_1,r'}^{J-\ell} + \beta_{J-\ell,J} \delta_{i,0} \quad (23b)$$

for $N_{\ell-1} + 1 \leq r \leq N_\ell$, where the sum in equation 23(b) is over the r' , for which $\tilde{Y}_{i_1,r'}^{J-\ell}$ gives a nonzero contribution. A sample of these particular values of r' and the parities $P_{r'}$ are given in table III.

Equation (22a) is the expression for the analytical solution of the GIT equations to be evaluated. One

advantage of the analytical solution (eq. (22a)) in the path-length variable s is that it is independent of the energy range relation. Once the proton stopping power is specified, then $\phi_{J-\ell}(x, E)$ is obtained from equation (3e). Additional quantities of interest, as well as solutions to more comprehensive benchmarks to be considered in the following sections, are obtained from the analytical form of Green's function.

2.3. Dose Profile

The dose profile (in x) for the ion $J - \ell$ (ref. 2) is given by integrating the total track length of ion j over all energy in a differential volume element multiplied by the energy loss per track length as follows:

$$D_{J-\ell}(x) = A_{J-\ell} \int_0^\infty dE S_{J-\ell} \phi_{J-\ell}(x, E) \quad (24)$$

Recall that $A_{J-\ell}$ is the atomic mass of the $J - \ell$ ion. Upon substituting the stopping-power scaling law (eq. (2a)) and equation (3e) into equation (24),

$$D_{J-\ell}(x) = A_{J-\ell} \nu_{J-\ell} \int_0^{R_{p_0}(E_0)} ds S_p(E(s)) \phi(x, s) \quad (25)$$

where R_{p_0} is the proton range in the shield material for incident ions of energy E_0 . When equation (22a) is introduced into the integral, the following closed-form representation for the dose results:

$$D_{J-\ell}(x) = A_{J-\ell} \nu_{J-\ell} \sum_{r=1}^{N_\ell} \exp(-\epsilon_r x) \tilde{Y}_{i_1,r}^{J-\ell} I_r(x) \quad (26a)$$

where

$$\left. \begin{aligned} \epsilon_r &\equiv \sigma_{J-i_1} - \beta_r \nu_{J-i_1} \\ \beta_r &\equiv a_r / b_r \end{aligned} \right\} \quad (26b)$$

$$\begin{aligned} I_r(x) &\equiv \theta(r_0 - \nu_{J-i_1} x) \int_{\nu_{J-i_1} x}^{r_0} ds S_p(E) \exp(-\beta_r s) \\ &\quad - \theta(r_0 - \nu_{J-i_2} x) \int_{\nu_{J-i_2} x}^{r_0} ds S_p(E) \exp(-\beta_r s) \end{aligned} \quad (26c)$$

$$r_0 = \min(R_{p_0}, \nu_{J-x}) \quad (26d)$$

To perform the integration either numerically or analytically, we are now faced with the task of specifying the range energy relation for protons.

Initially, a simplified range energy relation is specified so that the integrals I_r can be performed analytically to guarantee reliable benchmark results. This

relation takes the general form (ref. 9)

$$s = R_{p_o} - \alpha_o \ln(1 + \alpha_1 E^{n_o}) \quad (27)$$

The simplest case is for n_o taken as unity, which yields a simplified stopping power

$$S_p = \alpha \exp[(s - R_{p_o})\beta] \quad (28)$$

where

$$\alpha \equiv \frac{1}{\alpha_1 \alpha_o}$$

$$\beta \equiv \frac{1}{\alpha_o}$$

The following prescription is used to determine the parameters α and β :

- (a) The more accurate proton stopping-power (called the Wilson stopping power) relation ($-dE/ds$) given by equation (27) with (ref. 9)

$$\left. \begin{aligned} n_o &= 1.79 \\ \alpha_o &= 500 \\ \alpha_1 &= 3.66 \times 10^{-6} \end{aligned} \right\} \quad (29a)$$

is used to specify the proton range as follows:

$$R_{p_o} = \alpha_o \ln(1 + \alpha_1 E_o^{n_o}) \quad (29b)$$

- (b) Since, in the energy variable, the simplified stopping power is

$$S_p(E) = \alpha + \beta E \quad (29c)$$

β can be extracted as the slope

$$\beta = [S_p(E_1) - S_p(E_2)] / (E_1 - E_2) \quad (29d)$$

given two values of stopping power $S_p(E_1)$ and $S_p(E_2)$ at energies E_1 and E_2 , respectively. These stopping powers are obtained from the more comprehensive stopping power referred to in (a) above.

- (c) If $E = 0$ when $s = R_{p_o}$ and $E = E_o$ when $s = 0$, then

$$\frac{\alpha}{\beta} = \frac{E_o}{\exp(R_{p_o}\beta) - 1} \quad (29e)$$

gives a consistent value of α with β and the proton range.

When the stopping power, as represented by equation (28), is introduced into the integrand of I_r (eq. (26c)), the integrals can be performed analytically to give

$$I_r(x) = \frac{\alpha \exp(R_{p_o}\beta)}{\beta_r + \beta} \theta(r_o - \nu_{J-i_1} x) \times \left\{ \exp\left[-(\beta_r + \beta)\nu_{J-i_1} x\right] - \exp\left[-(\beta_r + \beta)r_o\right] \right\} - \theta(r_o - \nu_{J-i_2} x) \left\{ \exp\left[-(\beta_r + \beta)\nu_{J-i_2} x\right] - \exp\left[-(\beta_r + \beta)r_o\right] \right\} \quad (30)$$

For the more comprehensive stopping-power formula with α_o , α_1 , and n_o specified by equation (29a), the integrals must be performed numerically. This is most conveniently done by transforming to the energy variable. Then the integrals in equation (26d) are of the form

$$I_{r,i} = \int_{E(r_o)}^{E(\nu_{J-i} x)} dE \exp[-\beta_r s(E)] \quad (31a)$$

where $s(E)$ is given by equation (27) and

$$E(s) = \left\{ \frac{\exp[(R_{p_o} - s)/\alpha_o] - 1}{\alpha_1} \right\}^{1/n_o} \quad (31b)$$

Finally, $I_{r,i}$ is evaluated by using a reliable quadrature scheme. The dose for the uncollided ions, $\ell = 0$, is obtained by substituting equation (4a) into equation (24)

$$D_J(x) = A_J \nu_J \int_0^{R_{p_o}} ds S_p(s) \phi_J(x, s) = A_J \nu_J \exp(-\sigma_J x) S_p(\nu_J x) \theta(R_{p_o} - \nu_J x) \quad (32)$$

for any proton stopping power S_p .

2.4. Source With an Energy Distribution

Since the solution for a beam source is actually Green's function in the energy variable, a source for ions of charge J impinging on the shield surface of the form

$$\phi_j(0, E) = \delta_{iJ} f(E) \theta(E_o - E) \quad (33)$$

can be accommodated. An energy cutoff E_o has been imposed so that the path length given by equation (3d) will again have meaning.

The j th ion flux for this source is therefore

$$\phi_j^*(x, E) = \int_E^{E_0} dE' f(E') \phi_j(x, E') \quad (34)$$

where the explicit dependence of Green's function ϕ_j on the beam energy E' has been included. The appropriate change of variable yields

$$\phi_j^*(x, E) = \phi_j^*(x, s)/S_p(E) \quad (35a)$$

and

$$f(E) = f(s)/S_p(E) \quad (35b)$$

where

$$\phi_j^*(x, s) \equiv \int_0^s ds' f(s - s') \phi_j(x, s') \quad (35c)$$

Then, by substituting equation (22a) into equation (35c), the closed-form representation of the flux from a distributed source is

$$\phi_{J-\ell}^*(x, s) = \sum_{r=1}^{N_\ell} \exp(-\epsilon_r x) \tilde{Y}_{i_{1,r}}^{J-\ell} J_r(x, s) \quad (36a)$$

where

$$J_r(x, s) \equiv \theta(r_0 - \nu_{J-i_1} x) \int_{x\nu_{J-i_1}}^{r_0} ds' f(s - s') \exp(-\beta_r s') \\ - \theta(r_0 - \nu_{J-i_2} x) \int_{x\nu_{J-i_2}}^{r_0} ds' f(s - s') \exp(-\beta_r s') \quad (36b)$$

and

$$r_0 = \min(s, x\nu_J) \quad (36c)$$

Finally, for the incident ions ($\ell = 0$) from equation (4a),

$$\phi_J^*(x, s) = \exp(-\sigma_J x) f(s - \nu_J x) \theta(s - \nu_J x) \quad (36d)$$

To generate benchmark results, we consider, as an example, a source of the form

$$f(s) = Q_0 \exp(-M_0 s) \quad (37a)$$

or in the energy variable

$$f(E) = Q_0 \frac{\exp[-M_0 s(E)]}{S_p(E)} \quad (37b)$$

yields

$$J_r(x, s) = \frac{Q_0}{M_0 - \beta_r} \exp(-M_0 s) \left\{ \theta(r_0 - \nu_{J-i_1} x) \right. \\ \times \left\{ \exp[(M_0 - \beta_r)r_0] - \exp[(M_0 - \beta_r)x\nu_{J-i_1}] \right\} \\ \left. - \theta(r_0 - \nu_{J-i_2} x) \left\{ \exp[(M_0 - \beta_r)r_0] \right. \right. \\ \left. \left. - \exp[(M_0 - \beta_r)x\nu_{J-i_2}] \right\} \right\} \quad (37c)$$

For the source ions,

$$\phi_j^*(x, s) = Q_0 \exp[-(\sigma_J - M_0 \nu_J)x] \exp(-M_0 s) \theta(s - \nu_J x) \quad (37d)$$

A more general class of analytical sources can also provide benchmark flux profiles. If a source $f(s)$ possesses an explicit Laplace transform $\bar{f}(p)$, then since the integral in equation (35c) is of the convolution type, we find after application of a Laplace transform that

$$\bar{\phi}_j^*(x, p) = \bar{f}(p) \bar{\phi}_j(x, p)$$

The transform of $\phi_j(x, s)$ is easily obtained from equation (22a) as

$$\bar{\phi}_j(x, p) = \sum_{r=1}^{N_\ell} \exp(-\epsilon_r x) \tilde{Y}_{i_{1,r}}^{J-\ell} \\ \times \left\{ \frac{\exp[-(\beta_r + p)\nu_{J-i_1} x]}{\beta_r + p} - \frac{\exp[(\beta_r + p)\nu_{J-i_2} x]}{\beta_r + p} \right\} \quad (38)$$

Then, upon inversion of equation (38),

$$\phi_j^*(x, s) = \sum_{r=1}^{N_\ell} \exp(-\epsilon_r x) \tilde{Y}_{i_{1,r}}^{J-\ell} \\ \times \left\{ \exp(-\beta_r \nu_{J-i_1} x) L_r(s - \nu_{J-i_1} x) \theta(s - \nu_{J-i_1} x) \right. \\ \left. - \exp(-\beta_r \nu_{J-i_2} x) L_r(s - \nu_{J-i_2} x) \theta(s - \nu_{J-i_2} x) \right\} \quad (39a)$$

where

$$L_r(x) \equiv \mathcal{L}_x^{-1} \left(\frac{\bar{f}(p)}{\beta_r + p} \right) \quad (39b)$$

If the inversion \mathcal{L}_x^{-1} can be performed analytically, then accurate benchmarks can be generated. In most cases, however, the transform cannot be performed analytically. For a general $\bar{f}(p)$, it is possible to perform the inversion numerically by using a recently developed numerical-inversion algorithm (ref. 10). Since numerous numerical inversions would have to be performed for a heavy incident ion ($J \geq 10$), the required computational time would be considerable. For lighter incident ions ($J \leq 10$), the above method could be applied for a reasonable computational effort. Of course, an even more general class of sources could be accommodated by using

a quadrature scheme to evaluate $J_r(x, s)$ as was done for the dose.

2.5. Composite Beam With Distributed Sources

Another generalization of the beam source is the composite beam. In this case, several ions of different charge are allowed to impinge on the shield surface with the same source incident energy per nucleon of E_o (same velocities). The GIT equations (eqs. (3a and 3b)) then become

$$L_j \phi_j(x, s) = \sum_{k=j+1}^J \beta_{jk} \phi_k(x, s) \quad (1 \leq j \leq J) \quad (40a)$$

and

$$\phi_j(0, s) = \sum_{j'=1}^J d_{j'} \delta_{j,j'} \delta(s) \quad (40b)$$

where

$$L_j \equiv \frac{\partial}{\partial x} + \nu_j \frac{\partial}{\partial s} + \sigma_j$$

and d_j is the abundance of ion j in the beam.

Since the GIT equations are linear, the composite beam can be decomposed into its individual ion components with a source at $x = 0$. Thus,

$$\left. \begin{aligned} L_j \phi_j^J(x, s) &= \sum_{k=j+1}^J \beta_{jk} \phi_k^J(x, s) & \phi_j^J(0, s) &= d_J \delta_{j,J} \delta(s) \\ L_{J-1} \phi_{J-1}^{J-1}(x, s) &= \sum_{k=j+1}^{J-1} \beta_{jk} \phi_k^{J-1}(x, s) & \phi_{J-1}^{J-1}(0, s) &= d_{J-1} \delta_{j,J-1} \delta(s) \\ &\vdots & &\vdots \\ L_2 \phi_2^2(x, s) &= \sum_{k=j+1}^2 \beta_{jk} \phi_k^2(x, s) & \phi_2^2(0, s) &= d_2 \delta_{j,2} \delta(s) \\ L_1 \phi_1^1(x, s) &= 0 & \phi_1^1(0, s) &= d_1 \delta_{j,1} \delta(s) \end{aligned} \right\} \quad (41)$$

where the superscript indicates the incident ion charge. When equations (41) are summed, we obtain

$$L_j \sum_{\ell'=0}^{J-1} \phi_j^{J-\ell'}(x, s) = \sum_{k=j+1}^{J-1} \beta_{jk} \sum_{\ell'=0}^{J-1} \phi_k^{J-\ell'}(x, s) \quad (42a)$$

and

$$\begin{aligned} \sum_{\ell'=0}^{J-1} \phi_j^{J-\ell'}(0, s) &= \sum_{\ell'=0}^{J-1} d_{J-\ell'} \delta_{j,J-\ell'} \delta(s) \\ &= \sum_{j'=1}^J d_{j'} \delta_{j,j'} \delta(s) \end{aligned} \quad (42b)$$

where use was made of the requirement that

$$\phi_j^{J-\ell'}(x, s) = 0$$

for $j \geq J - \ell'$. Therefore, because of the uniqueness of the GIT equations, a comparison of equations (40) and (42) yields

$$\phi_j(x, s) = \sum_{\ell'=0}^{J-1} \phi_j^{J-\ell'}(x, s) \quad (43)$$

Since $\phi_j^{J-\ell'}(x, s)$ is Green's function, the sum in equation (41) is obtained from equation (22a). Similarly, for a distributed source, the sum in equation (43) is obtained from equation (36a).

2.6. Distinction Between Neutrons and Protons

As currently written, the GIT equations treat all the ions with a mass number of one as protons. They all have an associated stopping power and range. To make the GIT equations more realistic, a neutron component has been added. Neutrons are given the charge number zero ($j = 0$), and the equation that describes their straight-ahead neutron motion is

$$\left(\frac{\partial}{\partial x} + \sigma_0\right) \phi_0(x, s) = \sum_{k=2}^J M_{0,k} \sigma_k \phi_k(x, s) \quad (44)$$

where $\nu_0 = 0$ and where it is assumed that protons cannot act as a source of neutrons. The absorption cross section is taken to be the same as for protons, and the multiplicities are assumed to be a fraction f_n of those for protons as follows:

$$\left. \begin{aligned} M_{0,1} &= 0 \\ M_{0,k} &= f_n M_{1,k} \quad (k \geq 2) \end{aligned} \right\} \quad (45)$$

The proton multiplicities are then modified by a factor $1 - f_n$.

The formulation also assumes that the neutrons are monoenergetic and do not have scattering interactions. The inclusion of neutrons here is done only for completeness; a more substantial model is currently under development.

3. Numerical Implementation

3.1. Nuclear Fragmentation Model and Stopping Power

To numerically evaluate the ion flux and dose for benchmarking purposes, the following simplified nuclear model is assumed:

$$\sigma_j = \bar{\sigma} j^{\frac{2}{3}} \quad (46a)$$

$$M_{jk} = \begin{cases} \frac{2}{k-1} & (k \geq j) \\ 0 & (k < j) \end{cases} \quad (46b)$$

The choice of σ_j is based on nuclear liquid drop model considerations. The multiplicities are chosen so that charge is conserved in each interaction. The cross-section normalization is an input parameter that is taken to be representative of an air shield as follows:

$$\bar{\sigma} = 0.01247 \text{ cm}^2/\text{g}$$

Unless otherwise stated, the simplified stopping power is used in the computations of this report. The values of energy for the determination of β from equation (29d) were taken as $E_1 = 10$ MeV/nucleon and $E_2 = 10^4$ MeV/nucleon, which provided a representation over the energy interval of interest.

3.2. Round-off Error

Because the solution for the ion flux that results from an incident beam is an analytical representation, discretization and truncation errors are not relevant to the numerical evaluation. However, a very real concern is the error that results from round off. The central numerical procedure used to evaluate the flux is the recurrence relation for the coefficients $Y_{i1,r}^{J-\ell}$ (eqs. (23)), which is rather involved. It is well-known that significant round-off error can accumulate when using recurrence relations. For this reason, the simplifications described in section 2.1 play an important role in round-off error mitigation.

The major cause of round-off error can be traced to the r summation in equation (22a). Table IV shows each term calculated in Control Data Corporation (CDC) double-precision arithmetic (≈ 29 digits) and the corresponding partial sums of the summation over r in equation (22a) for $x = 16.004$ g/cm², $E = 100$ MeV/nucleon, and $j = 16$. The incident ion is nickel ($J = 28$) at $E_0 = 5$ GeV/nucleon. The summation is remarkable, in that the partial sum oscillates between $\pm 10^{11}$ with a final result of $\approx 10^{-3}$. Thus, a precision of at least 14 digits is required for this computation to have one correct digit. The corresponding single-precision calculation fails to give a positive flux. The failure of single-precision arithmetic is expected because of the significant loss of precision. All computations are performed in double-precision arithmetic. Even though round-off error will cause failure of the r sum for the light ions produced from the heavy incident ions for $J \gtrsim 30$, there is no apparent ill effect for $J \lesssim 30$. If necessary and available, quadruple-precision routines could be employed. Round-off error is also expected to limit the dose and distributed source evaluations to only heavy ions when the integrals I_r and J_r cannot be performed analytically.

4. Results

The flux and dose expressions determined in section 2 are numerically evaluated for air shields in this section by using the nuclear model and stopping power discussed in section 3.

4.1. Flux Profile From a Monoenergetic Beam Source

According to the continuous slowing-down approximation, the incident ion that impacts the shield surface with energy E_0 has lost a known amount of energy after having traversed a given path length s . Thus, at a particular energy E_1 , a fraction of the incident ions given by $\exp(-\sigma_J x)$ have survived to the distance $x_J = s_1(E_1)/\nu_J$, where s_1 is determined from equation (27). At this point, $\sigma_J \phi_J(x, s) dx$ incident ions/sec per cross-sectional area fragment into lighter ions ($0 \leq j \leq J-1$). Because of their finite velocities, the secondary ions of charge $J-1$ that originate at x_J can then propagate to a maximum range of $x_{J-1} = s_1(E_1)/\nu_{J-1}$ at this energy (fig. 2). The flux profile decays with x because there is no source of secondary ions between the creation and allowable range. The fluxes $\phi_J(x, s)$ for several energies $E_1 < E_2 < \dots < E_5$ are displayed in figure 2(b). In keeping with the range energy relation, the region for which $\phi_{J-1}(x, E)$ is nonzero moves farther into the shield with decreasing energy (increasing path length). Also, the flux decreases with decreasing energy, because the penetration distances are greater at lower energies; these greater distances allow more of the $J-1$ ions to fragment into lighter ions. Figures 3(a) and 3(b) show the variation of $\phi_{J-1}(x, E)$ with E at a fixed position x and at several positions $x_1 < x_2 < \dots < x_5$. The decrease in the flux at lower energies is clearly evident.

In the region $s_1(E_1)/\nu_J \leq x \leq s_1(E_1)/\nu_{J-1}$, the secondary ions ($J-1$) continuously generate lighter ions. Figure 4(a) shows both $\phi_{J-1}(x, E)$ and $\phi_{J-2}(x, E)$ at energy E_1 . In the region where ions $J-2$ are produced ($s_1/\nu_J \leq x \leq s_1/\nu_{J-1}$), the flux increases as it should. When the source abates, the flux decreases until the ions reach their allowable range $x_{J-2} \equiv s_1/\nu_{J-2}$. At x_{J-1} , the slope of ϕ_{J-2} changes dramatically (being infinite), which indicates the reduction of the source abruptly to zero. Figure 4(b) shows the secondary and tertiary ion fluxes for several energies ($E_1 < E_2 < \dots < E_5$).

Considering the lighter ions ($J-3$, $J-4$, $J-5$) with representative fluxes shown in figures 5(a) and 5(b), we observe similar behavior. In the region $s_1/\nu_J \leq x \leq s_1/\nu_{J-1}$, where ions $J-1$ and $J-2$ produce ion $J-3$, the flux increases as a result of the increasing source. The slope again changes when the source from ϕ_{J-1} becomes zero. Because of the production of ion $J-2$ in the region $s_1/\nu_{J-1} \leq x \leq s_1/\nu_{J-2}$, and because of the attendant competition with loss from fragmentation, the flux for ion $J-3$ initially increases but then decreases. In the region of no $J-3$ ion source ($s/\nu_{J-2} \leq x \leq s_1/\nu_{J-3}$), the

flux is monotonically decreasing. The flux profiles become increasingly smooth for the lighter ions. This increase is a consequence of the smaller fraction that the discontinuous source represents of the total source at x_{J-i} , $1 \leq i \leq \ell-2$ for ion $J-\ell$. In addition, at $x_{J-\ell+1}$, where the only source is from the preceding ion, attenuation has reduced the source contribution significantly. However, a kink in the ϕ_{J-5} flux curve can still be observed at x_{J-4} .

When neon ions of energy 1 GeV/nucleon are incident on the shield surface, the resulting fluxes of the ions produced by fragmentation are shown in figures 6(a) to 6(c) for $E = 995$ MeV/nucleon, 950 MeV/nucleon, and 100 MeV/nucleon. For the energy nearest the source energy, $E = 995$ MeV/nucleon, the fluxes are a series of waves of almost uniform density that originate at $x \approx 0.6$ and extend to the maximum range of the proton ($j = 1$) at this energy. Since the ions have penetrated only a short distance into the shield, significant fragmentation has not yet occurred. For this reason, the maximum flux for each successive ion is less than that of the preceding ion until $j = 1$. Because all ions for which $j > 1$ can produce protons, the proton source starts to become significant and results in an increase in the flux near the end of the proton trajectory. This increase in fragmentation is clearly evident at 950 MeV/nucleon; these are indicated by significant increases in the fluxes of light ions $j = 1, 2, 3$. At 100 MeV/nucleon, the ions have almost penetrated to their maximum ranges ($309.75/\nu_j$), and the light ions now have the largest fluxes. Figure 6(d) displays the three energies and clearly shows the changing nature of the particle flux with penetration that results from fragmentation. Figures 7(a) and 7(b) show the flux energy dependence at several positions and show that the energy spectrum broadens with penetration.

The incident ion energy influences the flux profiles significantly, as shown in figures 8(a) and 8(b), where profiles at $E = 100$ MeV/nucleon for neon ions of incident energies 500 MeV/nucleon and 2 GeV/nucleon are shown. The heavy-ion flux is still present for an incident energy of 500 MeV/nucleon; however, for 2 GeV/nucleon, so much penetration has occurred that the heavy ions have almost all fragmented and left a negligible heavy-ion flux.

The cross-section normalization has a major effect on the profiles. Figures 9(a) and 9(b) show the flux profiles at 995 MeV/nucleon for neon incident at 1 GeV/nucleon with cross-section normalizations of 10^{-4} cm²/g and 1.0 cm²/g. The normalization is proportional to the shield density. Thus, for the rarefied shield ($\bar{\sigma} = 10^{-4}$), the ions behave as expected with only a small amount of light ion

production because of the relatively few interactions that cause fragmentation. However, for the dense shield ($\bar{\sigma} = 1.0$), a significant flux of light ions has already been generated after a penetration of only 3 g/cm^2 .

To demonstrate the general applicability of the analytical solution, the flux profiles for $E = 4.995$ and 2 GeV/nucleon for nickel incident on a shield at 5 GeV/nucleon are presented in figure 10. To obtain better resolution for the 2-GeV case, ϕ_j for $8 \leq j \leq 27$ and $1 \leq j \leq 7$ are plotted on separate plates. With CDC double precision, incident ions of charge up to ≈ 30 can be considered. For $J > 30$, the round-off error becomes a problem and higher precision routines must be used at the expense of storage and computational time.

4.2. Dose Profiles From a Monoenergetic Beam Source

The dose profiles given by equations (26a) to (26d) for the stopping power of equation (27) are evaluated here. Figures 11 to 13 show the dose profiles for incident neon beams of energies 670 MeV/nucleon , 2 GeV/nucleon , and 10 GeV/nucleon ; part a of each figure presents the individual ion doses and part b the normalized total dose $D(x)/D(0)$. In each case, the Bragg profile for the incident ion is clearly seen. As the incident energy increases, the maximum flux for the lighter ions moves farther into the shield and away from the Bragg cutoff at R_{p0}/ν_J . This movement causes the total dose to extend past the Bragg cutoff.

Unlike in the previous cases, when 5-GeV/nucleon cobalt ions are the incident ions (figs. 14(a) and 14(b)), a significant amount of the dose occurs after the Bragg cutoff ($\approx 105 \text{ g/cm}^2$). This is a result of the larger number of fragments produced and the deeper penetration of these fragments at a given energy per nucleon. Also, the larger number of ions gives rise to an increase in the dose near $x = 0$, rather than a decrease as seen for incident neon.

The following dose calculations were performed with the more realistic stopping power given by equations (27) and (29a). The integrals in equation (26c) were performed numerically by using a reliable Romberg integration routine (ref. 6). For incident neon of 670 MeV/nucleon , figure 15(a) shows the familiar Bragg peak and cutoff, and the contribution of the lighter ions is shown in figure 15(b). The profile of ion $j = 9$ seems to follow the dose profile of the incident ion near the Bragg peak. This aspect of course results from the simple fact that the incident ion is the sole producer of ion $j = 9$. As j decreases,

the maximum dose for each value of j moves farther into the medium away from the Bragg peak as the production of each subsequent ion becomes less dependent on the source ion. The similarity of the dose profiles for ions $j = 9$ and 10 is even more striking for an incident energy of 1 GeV/nucleon . (See figs. 16(a) and (b).) For higher incident energies (figs. 17(a) and (b)), the Bragg peak dissipates as a result of the increased fragmentation at larger penetration distances. Figure 18 presents the total dose for the previous three cases. The Bragg peaks again stand out for the lower incident energies. Figures 19 and 20 show the doses for nickel incident at energies of 1 GeV/nucleon and 5 GeV/nucleon , respectively. The curves represent only ions $18 \leq j \leq 28$, because, for $j \leq 18$, catastrophic round-off error accumulation occurs and limits the evaluation.

As an example of the use of the analytical solution as a predictive tool, the experimental dose from a neon beam incident on water (ref. 11) was compared with that obtained from the analytical solution. The comparison of the normalized doses is shown in figure 21. The curves are normalized to the dose at $x = 0$, and cross-section normalization $\bar{\sigma}$ was adjusted slightly to obtain a reasonable fit to the data. If desired, the fragmentation parameter could also be adjusted to obtain an even better fit.

4.3. Distributed Sources

Numerical results are now presented for analytical and solar distributed sources. An analytic source is one that allows the integral value of J_r to be expressed in closed form; the solar source requires a numerical quadrature evaluation.

4.3.1. Analytic source. Figures 22 and 23 show the flux profiles for neon ions that are incident with a distributed source in s (or E), given by equation (37a) or (37b), and a source cutoff taken at 10^4 MeV/nucleon . For small values of M_0 (0.01) and an energy very near the cutoff ($E = 9999.9 \text{ MeV/nucleon}$), the incident ion source dominates all other sources from fragmentation. Thus, in the region where the incident ion has a nonzero flux ($0 \leq x \leq s/\nu_J$), all lighter ion flux profiles are essentially identical. For this energy, the ions have only penetrated $\approx 0.01 \text{ g/cm}^2$, and significant fragmentation has not occurred. As the energy decreases (s increases) to 1 GeV/nucleon , the lighter ions build up similar to the beam source.

Similar behavior is observed in the flux profiles for a source that is more peaked at $s = 0$ ($M_0 = 1.0$). As shown in figure 23(a), the profiles are

virtually identical to the preceding case, since over the very short penetrations both sources look alike. For an energy of 1 GeV/nucleon (fig. 23b) the source resembles a delta function because of its rapid decay in s , and the profiles look like those for a beam source.

4.3.2. Solar source. A source of the form

$$f(E) = Q_0/(b_1 + E)^n$$

is typically taken to represent solar ions from the Sun. The J_r integral in equation (37c) cannot be performed analytically, so the numerical Romberg integration must be used. (See ref. 12.) Because of the excessive computer time required for these calculations, only a few ions (<10) can be considered. Figures 24(a) and (b) show the resulting ion fluxes (to $j = 19$) as a function of E for incident nickel with $Q_0 = 28446$, $b_1 = 1000$, and $n = 2.5$ at positions $x = 1 \text{ g/cm}^2$ and 10 g/cm^2 . As the distance into the shield increases, the lighter ion fluxes again increase because of fragmentation. All ion fluxes seem to have an energy variation similar to the incident ion source; this similarity suggests that a scaling law may apply.

4.4. Composite Beam

Figures 25(a) to 25(c) show the flux profiles using the Wilson stopping power for an artificial cosmic ray beam composed of the elements neon through iron with the assumed abundances given in table V. The jagged appearance of the flux profiles near the source energy 4.9 GeV/nucleon is a result of the relatively short penetration distances and the associated lack of fragmentation so close to the source energy. For this reason, the profiles for the ions with a charge near that of the incident ion still reflect the source distributions. The lighter ions, however, have smoother flux profiles as more fragmentation occurs at lower energies.

4.5. Generation of Neutrons

The parameter f_n in the cross-section model (eq. (45)) has been introduced to make the distinction between the neutron and proton components. (See section 2.6.) In figures 26(a) and (b), the resulting ion fluxes at $E = 500 \text{ MeV/nucleon}$ for an incident neon beam of $E_0 = 1 \text{ GeV/nucleon}$ are shown for $f_n = 0$ and 0.5. In addition, the Wilson stopping power has been used. As expected when f_n is increased from zero to one, the neutron component also increases with an attendant decrease in the proton component. The neutron component does not go to zero at a finite distance as for charged particles. After a distance equal to the proton range

($\approx 200 \text{ g/cm}^2$), the neutron flux decays exponentially (not shown), since there is no longer a neutron source in this region—only absorption.

4.6. Comparisons With Numerical Solutions

4.6.1. Finite-difference/power series expansion solution. For G intervals, if the GIT equations are discretized in the path-length variable, equations (3a) and (3b) become

$$\left[\frac{\partial}{\partial x} + \left(\sigma_j^g + \frac{\nu_j}{\Delta s} \right) \right] \phi_j^g(x) = \frac{\nu_j}{\Delta s} \phi_j^{g-1}(x) + \sum_{k=j+1}^J \beta_{jk}^g \phi_k^g(x) \quad (47a)$$

$$\phi_j^g(0) = f_j \delta_{jJ} \quad (g = 1, 2, \dots, G) \quad (47b)$$

The advantage of the discretized model is that energy-dependent cross sections and multiplicities can now readily be included. The solution to equations (47a) and (47b) is most easily obtained by applying the power series method, where the expansion

$$\phi_{j,g}^r(x) = \sum_{n=0}^{\infty} \frac{h_{n,j}^{g,r}}{n!} (x - a_{r-1}) \quad (48a)$$

is introduced into equations (47) to yield the following recursion relation for $h_{n,j}^{g,r}$:

$$\left. \begin{aligned} h_{n,j}^{g,r} = & - \left(\sigma_{j,g} + \frac{\gamma_j}{\Delta s} \right) h_{n,j}^{g,r} + \frac{\gamma_j}{\Delta s} h_{n-1,j}^{g-1,r} \\ & + \sum_{k=j+1}^J \beta_{jk}^g h_{n-1,k}^{g,r} \\ h_{0,j}^{g,r} = & \phi_{n,j}^{r-1}(a_{r-1}) \end{aligned} \right\} \quad (48b)$$

The particular form of equation (48a) is valid for x in the interval $[a_{r-1}, a_r]$. For incident neon at $E_0 = 670 \text{ MeV/neutron}$, a flux comparison of the above interval solution with the analytical solution (eq. (22a)) is given in figure 27. The flux energy spectrum is shown at a position of 10 g/cm^2 from the surface. Even for relatively large values of Δs , the proton flux ($j = 1$) is in relatively good agreement; there is poor agreement for the heavy ions. This poor agreement is probably a result of the highly singular nature of the incident beam (eq. (4a)), which leads to discontinuous distributions for ions 9 and 10; these ions are poorly simulated with finite differences. However, as Δs is reduced, the general agreement

improves. Another area of disagreement is at the beginning and end of the ion travel, where the flux falls sharply to zero. Because of numerical diffusion, the finite-difference solution does not exhibit step function behavior, but the fluxes do become steeper with increasing Δs . The finite-difference solution does, however, give the correct flux average at these discontinuities as Δs decreases.

4.6.2. Integral transport finite-difference solution. Our final comparison is with the GCR code (ref. 11) currently in use at Langley Research Center and Johnson Space Center. The GCR code solves the GIT equations by integration along the ion trajectories on a spatial and energy grid. From previous benchmark comparisons, the code is expected to be accurate to better than 10 percent.

Figure 28 shows the flux profiles for the GCR code and benchmark for a distributed source of neon of the form

$$f(s) = \exp(0.01s)\theta(10^5 - E)$$

impinging on an air shield. The nuclear fragmentation model specified by equations (46) was used along with the simplified stopping power given by equations (29). To provide a contrast, the benchmark calculation begins at $E = 20$ MeV, whereas the GCR calculation begins at $E = 100$ MeV. The two evaluations are in excellent agreement even at 100 g/cm^2 . Figure 29 shows the flux profiles for incident nickel with the same source; these profiles again indicate virtually complete agreement. These comparisons provide added confidence that the GCR code employs a very accurate transport algorithm.

5. Summary and Recommendations

Based on its success in generating previous benchmark solutions, a straightforward analytical approach has been adopted to solve the full GIT equations. As a result, a closed-form analytical representation of the ion fluxes that result from a monoenergetic incident ion source has been derived. While there are no truncation errors to contend with, round-off error does present a problem. The problem becomes serious only when the incident ion is very heavy ($J \geq 28$) and when the energies are near the source energy; otherwise, 64-bit, double-precision arithmetic adequately allows the evaluation of the

flux representation. The dose profiles can also be obtained from the analytical representation with the additional evaluation of an integral.

Since the flux for the beam source is actually a Green's function, the flux profiles for sources distributed in energy can be obtained by integration over the source energy. This integration, unless it is performed analytically, introduces round-off error contamination that may limit the total number of isotope flux profiles that can be evaluated. A more general beam source composed of several ions with the same velocity can also be accommodated.

Finally, a distinction between neutrons and protons is made to more correctly take into account the attenuation of neutrons. The neutrons, however, are still monoenergetic, and therefore do not contribute to the overall dose. It is this last point that deserves further attention.

An improved neutron flux model, including scattering interactions, should be the first step of a future effort. By using the ions where $j \geq 3$ to specify a neutron source, it is possible to formulate a more realistic Boltzmann equation for the neutron component. A multigroup treatment can then be applied to this equation both with and without the straight-ahead assumption. In this way, the neutron energy spectrum can be obtained either by a discretization in the spatial variable or a discrete-ordinates formulation in the angular variable. Once angular dependence has been introduced into the formulation, two- and three-dimensional shields can be considered.

In addition to continuing to develop benchmarks for more realistic problems, such as including energy dependence in the cross sections or angular dependence, the benchmark solutions developed thus far should be compared with existing transport algorithms to establish a common basis of comparison for these algorithms. The benchmark solutions should be considered as a package that includes the energy-independent, spatially independent and coupled energy-space solutions. Each solution should be checked to verify each specific part of a transport algorithm.

NASA Langley Research Center
Hampton, VA 23665-5225
August 26, 1991

6. References

1. Wilson, John W.; and Townsend, L. W.: A Benchmark for Galactic Cosmic-Ray Transport Codes. *Radiat. Res.*, vol. 114, no. 2, May 1988, pp. 201-206.
2. Ganapol, Barry D.; Townsend, Lawrence W.; and Wilson, John W.: *Benchmark Solutions for the Galactic Ion Transport Equations: Energy and Spatially Dependent Problems*. NASA TP-2878, 1989.
3. Wilson, John W.: *Analysis of the Theory of High-Energy Ion Transport*. NASA TN D-8381, 1977.
4. Alsmiller, R. G., Jr.; Irving, D. C.; Kinney, W. E.; and Moran, H. S.: The Validity of the Straightahead Approximation in Space Vehicle Shielding Studies. *Second Symposium on Protection Against Radiations in Space*, Arthur Reetz, Jr., ed., NASA SP-71, 1965, pp. 177-181.
5. Alsmiller, R. G., Jr.; Irving, D. C.; and Moran, H. S.: Validity of the Straightahead Approximation in Space-Vehicle Shielding Studies, Part II. *Nucl. Sci. & Eng.*, vol. 32, no. 1, Apr. 1968, pp. 56-61.
6. Wilson, John W.: *Heavy Ion Transport in the Straight Ahead Approximation*. NASA TP-2178, 1983.
7. Wilson, John W.; Townsend, Lawrence W.; Nealy, John E.; Chun, Sang Y.; Hong, B. S.; Buck, Warren W.; Lamkin, S. L.; Ganapol, Barry D.; Khan, Ferdous; and Cucinotta, Francis A.: *BRYNTRN: A Baryon Transport Model*. NASA TP-2887, 1989.
8. Wilson, John W.; and Lamkin, Stanley L.: Perturbation Theory for Charged-Particle Transport in One Dimension. *Nucl. Sci. & Eng.*, vol. 57, no. 4, Aug. 1975, pp. 292-299.
9. Wilson, John W.; and Badavi, F. F.: Methods of Galactic Heavy Ion Transport. *Radiat. Res.*, vol. 108, 1986, pp. 231-237.
10. Ganapol, B. D.: The Solution of the Time-Independent Neutron Slowing Down Equation Using a Numerical Laplace Transform Inversion. *Transp. Theory & Stat. Phys.*, vol. 19, no. 1, 1990, pp. 1-27.
11. Wilson, John W.; Townsend, L. W.; Bidasaria, H. B.; Schimmerling, Walter; Wong, Mervyn; and Howard, Jerry: ^{20}Ne Depth-Dose Relations in Water. *Health Phys.*, vol. 46, no. 5, May 1984, pp. 1101-1111.
12. Miller, Alan R.: *FORTTRAN Programs for Scientists and Engineers*, 1st ed. SYBEX, Inc., 1982.

7. Symbols

A_j	mass number of j th ion	r_o	defined in equation (26d)
a_i	position of i th interval boundary, g/cm ²	S_j	stopping power of j th ion, MeV-cm ² /g
$a_{\ell m}$	$\equiv \sigma_{\ell} - \sigma_m$	S_p	proton stopping power, MeV-cm ² /g
a_1	$\equiv \sigma_{J-1} - \sigma_J$	$s(E, E_o)$	proton path length, g/cm ²
$b_{\ell m}$	$\equiv \nu_{\ell} - \nu_m$	x	position, g/cm ²
b_1	$\equiv \nu_{J-1} - \nu_J$	Y_{ij}^k	defined by equation (7b)
D_j	dose due to j th ion, MeV/g	\tilde{Y}_{ij}^k	defined by equation (22b)
d_j	abundance of j th beam ion	α	$\equiv \frac{1}{\alpha_1 \alpha_o}$
E	energy per nucleon, MeV/nucleon	a_{ij}	recursion coefficient
f_j	monoenergetic beam source term	α_o, α_1, n_o	parameters used in equation (27)
\bar{f}_j	Laplace transform of f_j	β	$\equiv \frac{1}{\alpha_o}$
$h_{n,j}^{g,r}$	power series coefficient	β_{jk}	$= M_{jk} \sigma_k$ (eq. (3c))
I_r	defined by equation (26c)	Δs	finite-difference interval, g/cm ²
$I_{r,i}$	defined by equation (31a)	$\delta(s)$	Dirac δ -function
J	charge number of incident ion	δ_{ij}	Kronecker delta
J_r	defined by equation (36b)	$\theta(x)$	Heaviside step function
j	charge number of j th ion	Λ_r	defined by equation on page 4
L_j	defined by equation (40a)	ν_j	$\equiv \frac{Z_j^2}{A_j}$ (eq. (2b))
L_r	defined by equation (39b)	$\bar{\sigma}$	cross-section parameter, cm ² /g
M_{jk}	multiplicity of ion j produced by ion k	σ_j	macroscopic absorption cross section for j th ion, cm ² /g
N_{ℓ}	defined by equation (12)	ϕ_j	flux of j th ion
N_p	number of intervals	$\tilde{\phi}_j$	Laplace transform of ϕ_j
$Q(x, s)$	volume source coefficient	$\hat{\chi}$	defined by equation on page 5
Q_o, M_o	parameters in equation (37a)		
R	range, g/cm ²		

Table I. Relation of r Index to ℓ

$$\left[\Lambda_r(p) = \frac{1}{a_{mn} + b_{mnp}} \right]$$

r	ℓ	m	n	N_ℓ
1	1	$J-1$	J	1
2	2	$J-2$	J	3
3	3	$J-2$	$J-1$	6
4		$J-3$	J	
5	4	$J-3$	$J-1$	10
6		$J-3$	$J-2$	
7		$J-4$	J	
8		$J-4$	$J-1$	
9		$J-4$	$J-2$	
10		$J-4$	$J-3$	
\vdots	\vdots	\vdots	\vdots	\vdots

Table II. Variation of i_1 and i_2 To Satisfy Equation (20) With r

ℓ	r	i_1	i_2
1	1	0	1
	2	0	2
3	3	1	2
	4	0	3
	5	1	3
4	6	2	3
	7	0	4
	8	1	4
	9	2	4
5	10	3	4
	11	0	5
	12	1	5
	13	2	5
	14	3	5
	15	4	5

Table III. Nonzero Contributions to Sum in Equation (23b)

	r'	$P_{r'}$		r'	$P_{r'}$
$i = 0$	0	1	$i = 1$	1	-1
	1	1		3	1
	2	1		5	1
	4	1		8	1
	7	1		12	1
	11	1		17	1
$i = 2$	2	-1	$i = 3$	4	-1
	3	-1		5	-1
	6	1		6	-1
	9	1		10	1
	13	1		14	1
	18	1		19	1
$i = 4$	7	-1	$i = 5$	8	-1
	8	-1		9	-1
	9	-1		10	-1
	10	-1		11	-1
	15	1		12	-1
	20	1		16	1

Table IV. Partial Sums in Evaluation of Equation (22a)

$$\left[S_m = \sum_{r=1}^m T_r \right]$$

r	T_r	S_m	r	T_r	S_m
37	3.9228E+07	3.9228E+07	79	-1.1811E+08	-7.5948E+10
38	9.7776E+08	1.0170E+09	80	-8.1489E+09	-8.4097E+10
39	1.1020E+10	1.2037E+10	81	1.2471E+10	-7.1626E+10
40	-1.5280E+06	1.2035E+10	82	1.6089E+11	8.9259E+10
41	8.7956E+06	1.2044E+10	83	1.6572E+10	1.0583E+11
42	-1.5549E+02	1.2044E+10	84	3.8245E+05	1.0583E+11
43	1.3975E+02	1.2044E+10	85	2.2172E+08	1.0605E+11
44	1.2963E+01	1.2044E+10	86	-1.1062E+11	-4.5652E+09
45	1.7750E+01	1.2044E+10	87	1.2098E+06	-4.5640E+09
46	-1.7809E+03	1.2044E+10	92	2.2978E+10	1.8414E+10
47	-3.3768E+04	1.2044E+10	93	-1.8297E+09	1.6584E+10
48	1.6875E+04	1.2044E+10	94	-7.1510E+09	9.4334E+09
49	2.2094E+03	1.2044E+10	95	-1.6057E+08	9.2729E+09
50	-1.1694E+05	1.2044E+10	96	3.5538E+08	9.6282E+09
51	-5.3195E+01	1.2044E+10	97	8.8145E+04	9.6283E+09
52	1.3282E+05	1.2044E+10	98	-1.7218E+06	9.6266E+09
53	6.4344E+02	1.2044E+10	99	2.4350E+07	9.6510E+09
54	-3.7529E-02	1.2044E+10	100	-1.4887E+08	9.5021E+09
56	-3.8850E+06	1.2040E+10	106	1.3371E+08	9.6358E+09
57	-5.6258E+09	6.4145E+09	107	1.2474E+10	2.2110E+10
58	2.7668E+08	6.6911E+09	108	-1.1917E+10	1.0192E+10
59	-1.1491E+11	-1.0821E+11	109	8.1157E+08	1.1004E+10
60	-2.0332E+10	-1.2855E+11	110	5.9305E+09	1.6934E+10
61	-1.7720E+05	-1.2855E+11	111	2.4703E+04	1.6934E+10
62	1.9891E+07	-1.2853E+11	112	-4.6283E+06	1.6930E+10
63	6.6318E+10	-6.2209E+10	113	-2.2498E+09	1.4680E+10
64	-5.9047E+03	-6.2209E+10	114	-1.3697E+07	1.4666E+10
67	-1.3597E+10	-7.5806E+10	121	-9.4346E+09	5.2317E+09
68	-2.5725E+08	-7.6063E+10	122	2.3988E+09	7.6304E+09
69	1.8921E+08	-7.5874E+10	123	-4.8884E+09	2.7420E+09
70	1.0403E+07	-7.5864E+10	124	6.2213E+09	8.9633E+09
71	-3.9645E+07	-7.5903E+10	125	-2.4306E+09	6.5326E+09
72	-5.2003E+02	-7.5903E+10	126	-3.1752E+05	6.5323E+09
73	1.1232E+04	-7.5903E+10	127	-2.3539E+08	6.2969E+09
74	-7.1222E+04	-7.5903E+10	128	-6.3879E+09	-9.0967E+07
75	7.3132E+07	-7.5830E+10	129	9.0967E+07	9.7023E-04

Table V. Composite Cosmic Ray Beam*

Element	Abundance, percent
Fe	1.3
Mn	0.6
Cr	1.7
V	1.4
Ti	2.0
Sc	2.0
Ca	1.8
K	2.5
Ar	1.8
Cl	2.6
S	2.5
P	5.1
Si	7.2
Al	11.5
Mg	16.3
Na	14.7
Ne	23.1
Fe [†]	1.9

* Portion of cosmic ray spectrum from neon to iron.

† Added to make 100 percent.

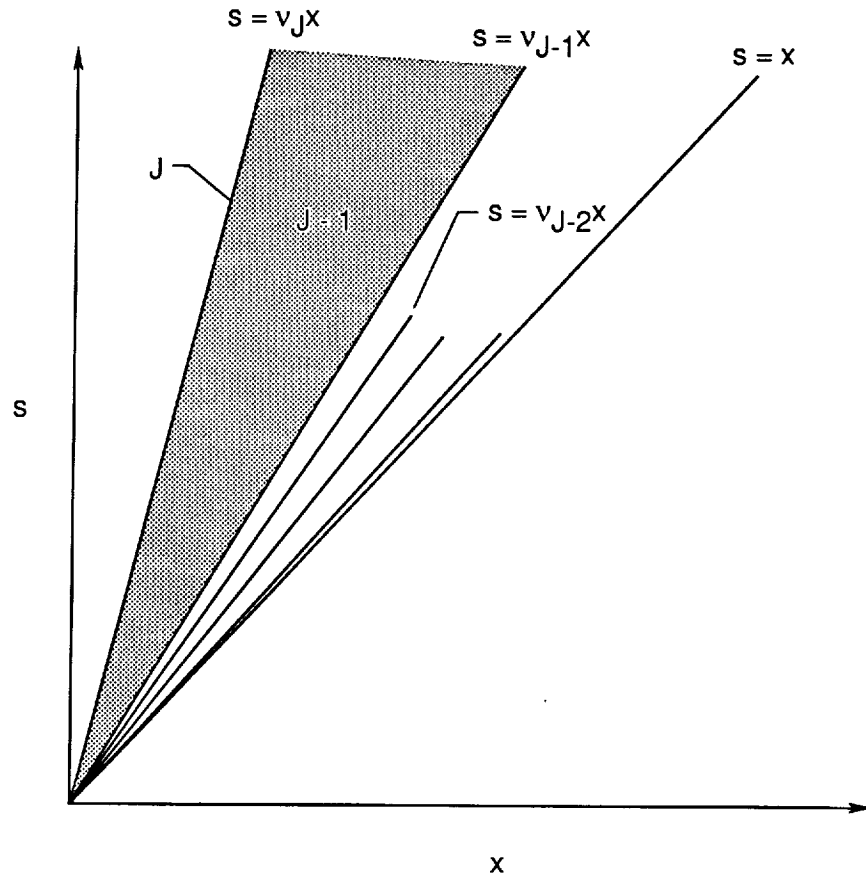
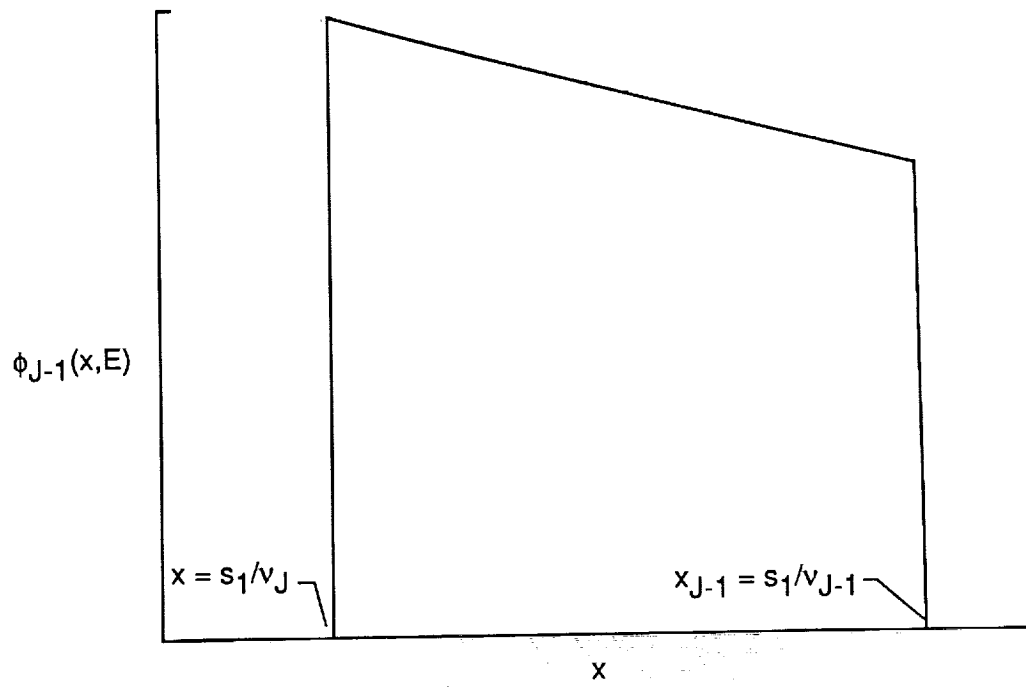
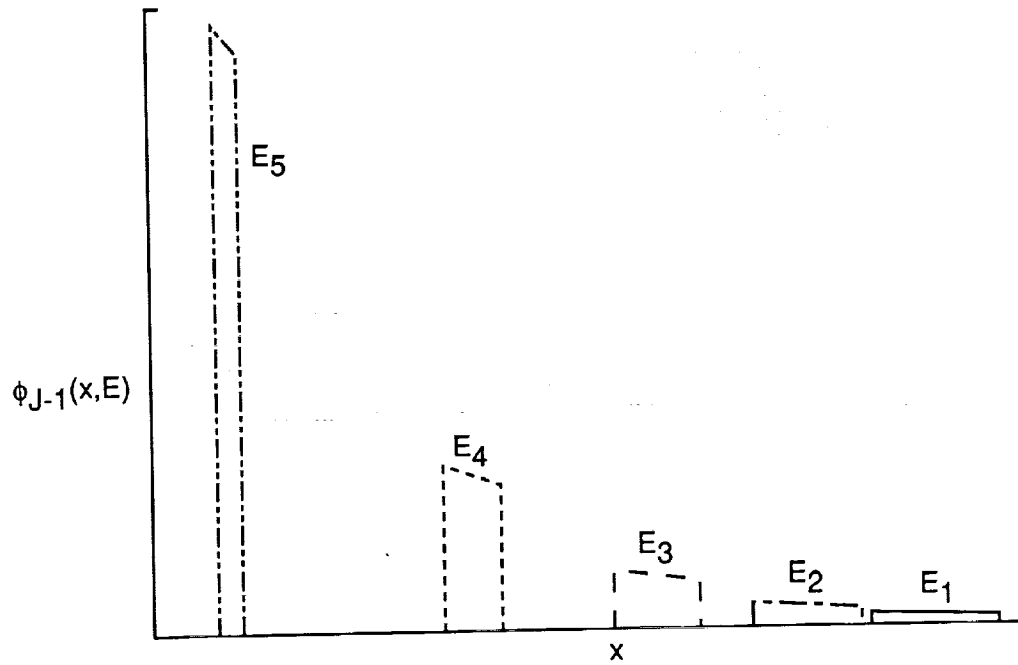


Figure 1. The x, s representation of nonzero region of j th ion flux $\phi_j(x, s)$.

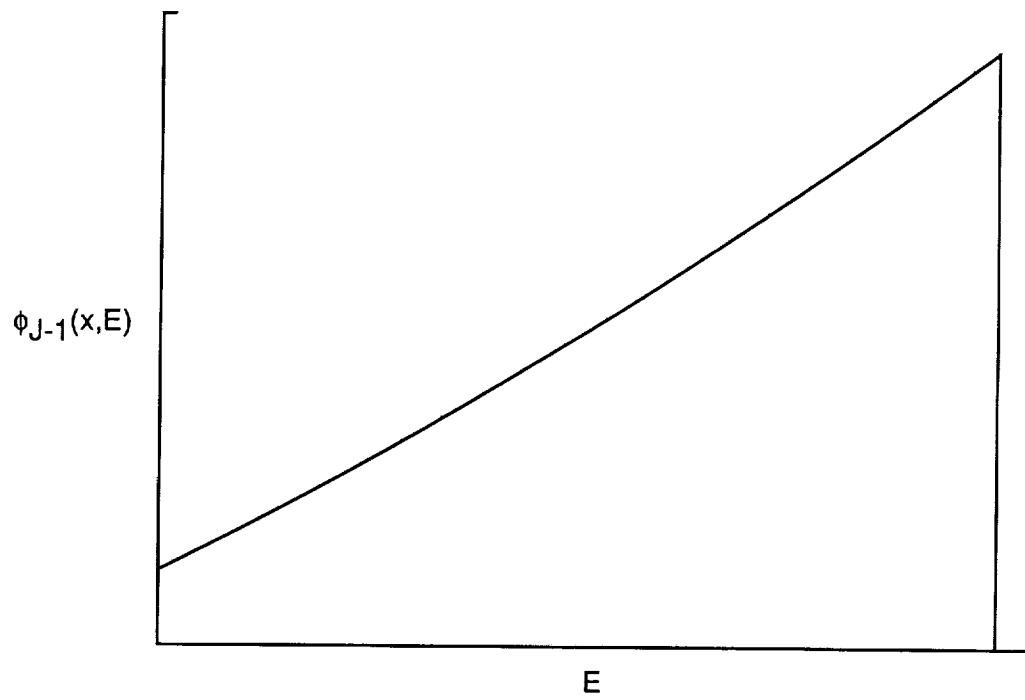


(a) Energy E_1 .

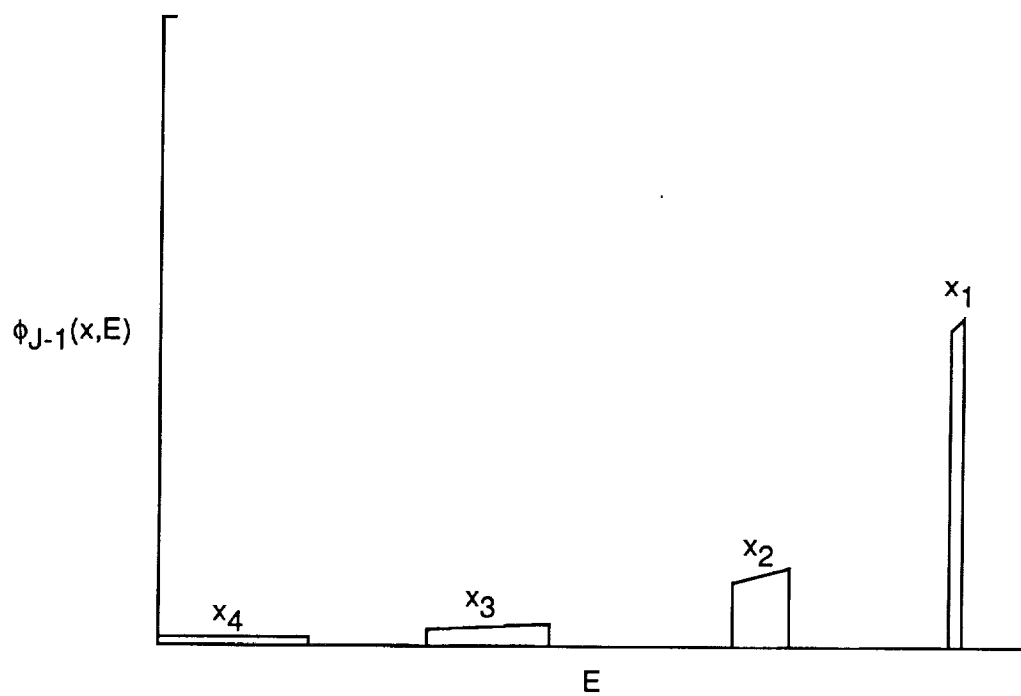


(b) Energies $E_1 < E_2 < \dots < E_5$.

Figure 2. Variation of flux for ion $J - 1$ with x .

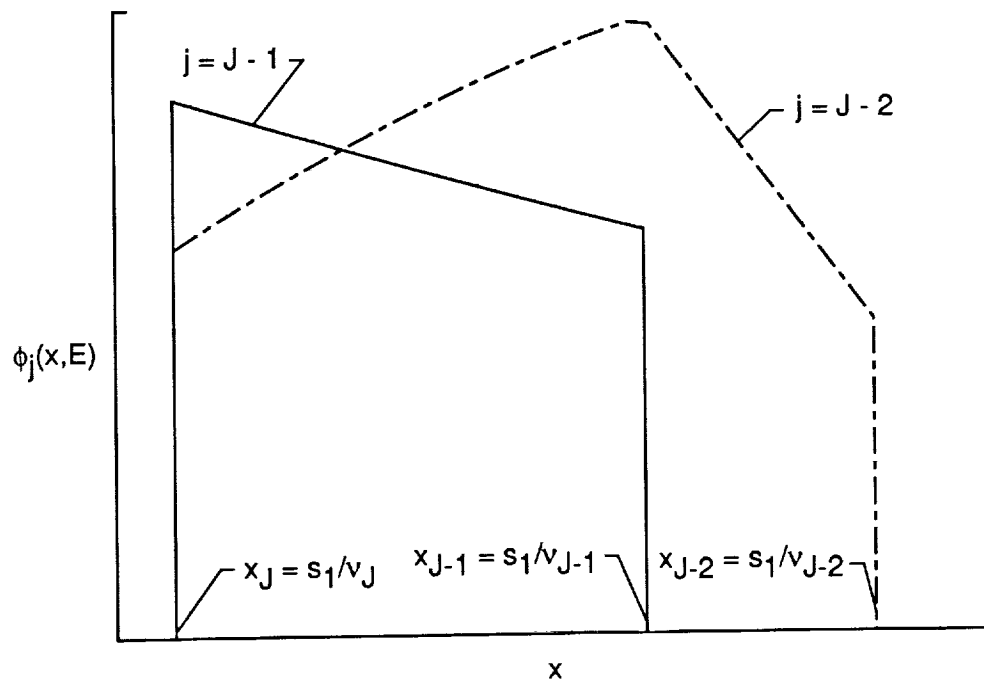


(a) Position x_1 .

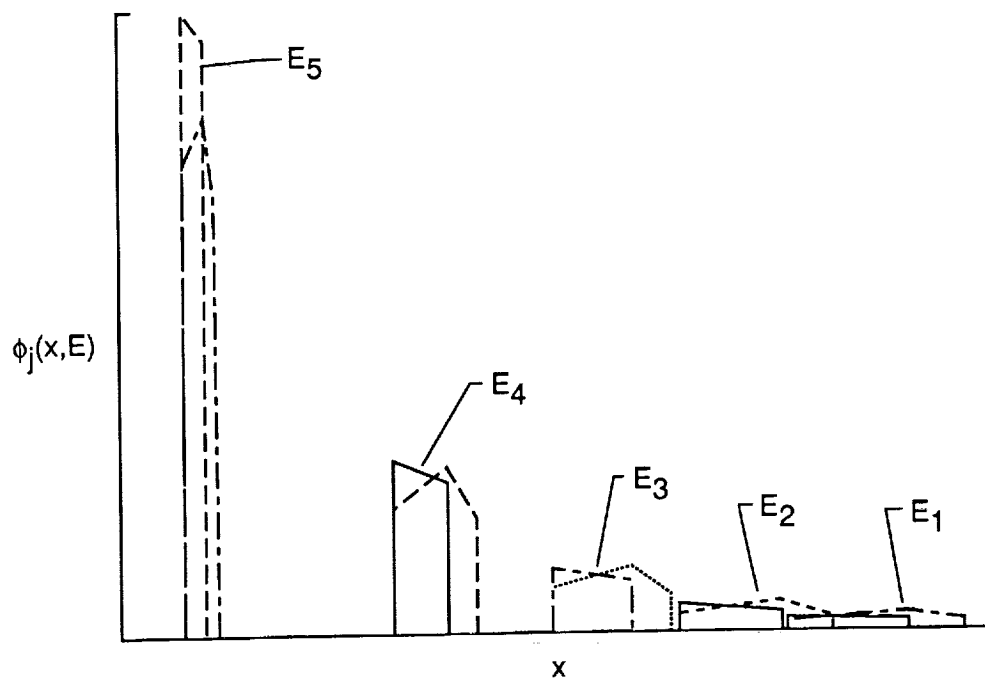


(b) Positions $x_1 < x_2 < \dots < x_5$.

Figure 3. Variation of flux for ion $J - 1$ with E .

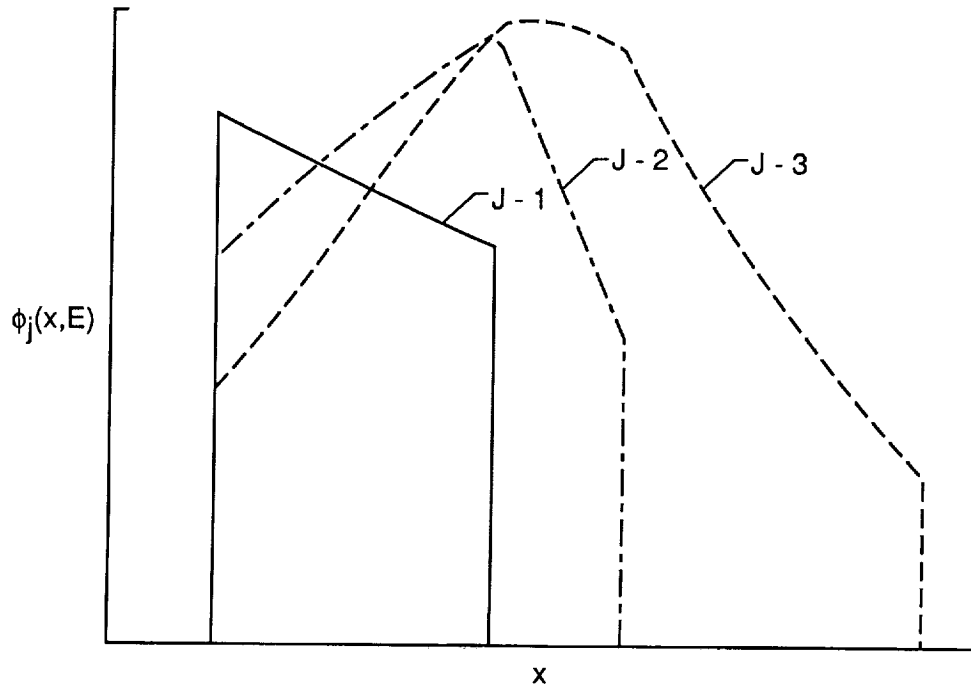


(a) Energy E_1 .

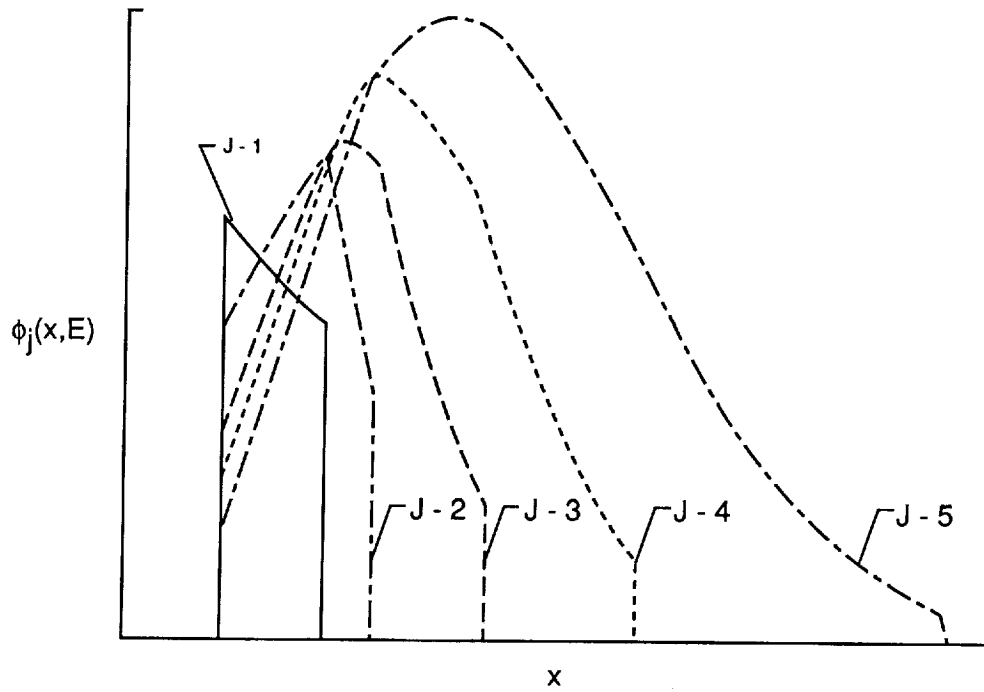


(b) Energies $E_1 < E_2 < \dots < E_5$.

Figure 4. Variation of flux for ions $J - 1$ and $J - 2$ with x .

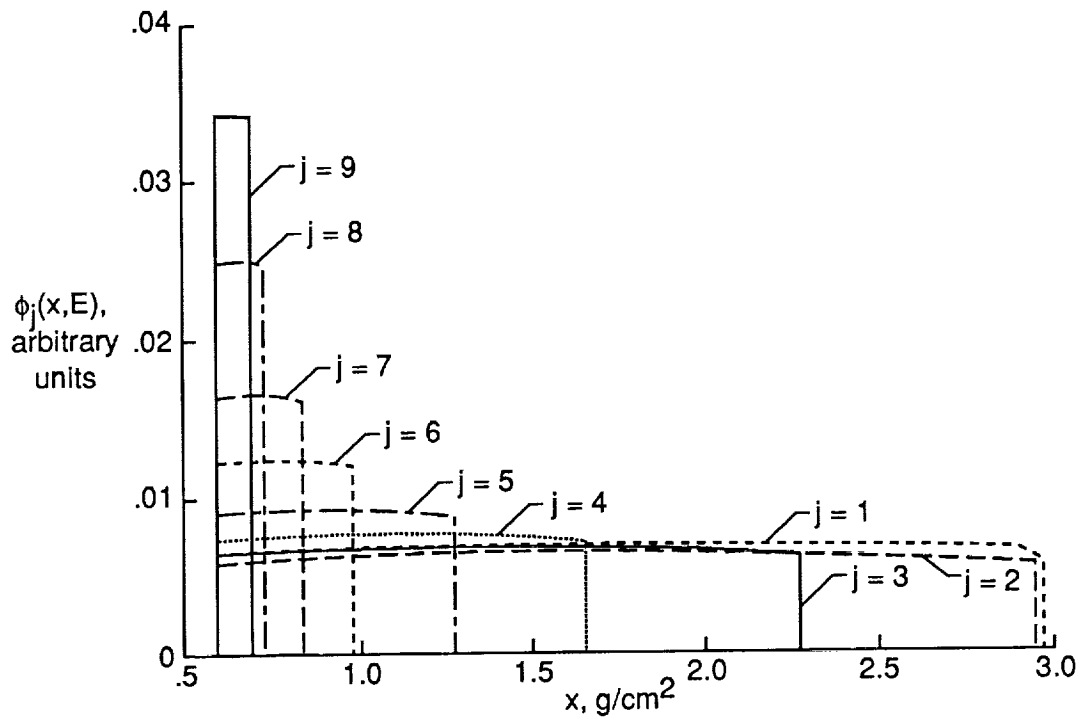


(a) $\ell = 1, 2, 3$.

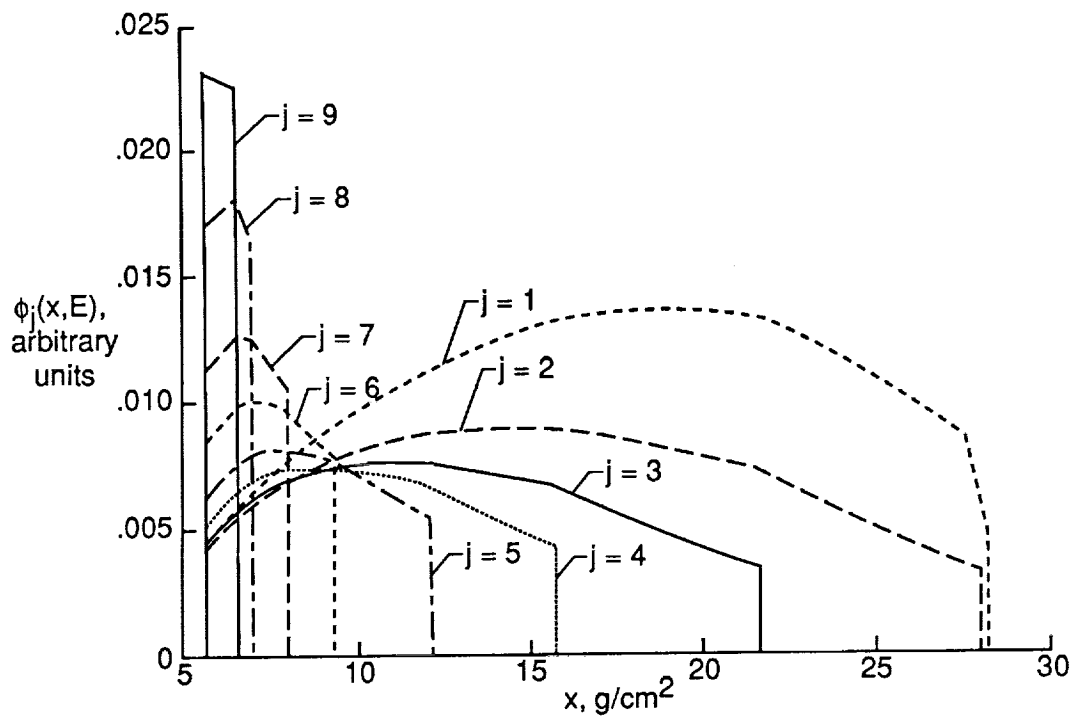


(b) $\ell = 1, 2, \dots, 5$.

Figure 5. Variation of flux for ions $J - \ell$ at energy E_1 .

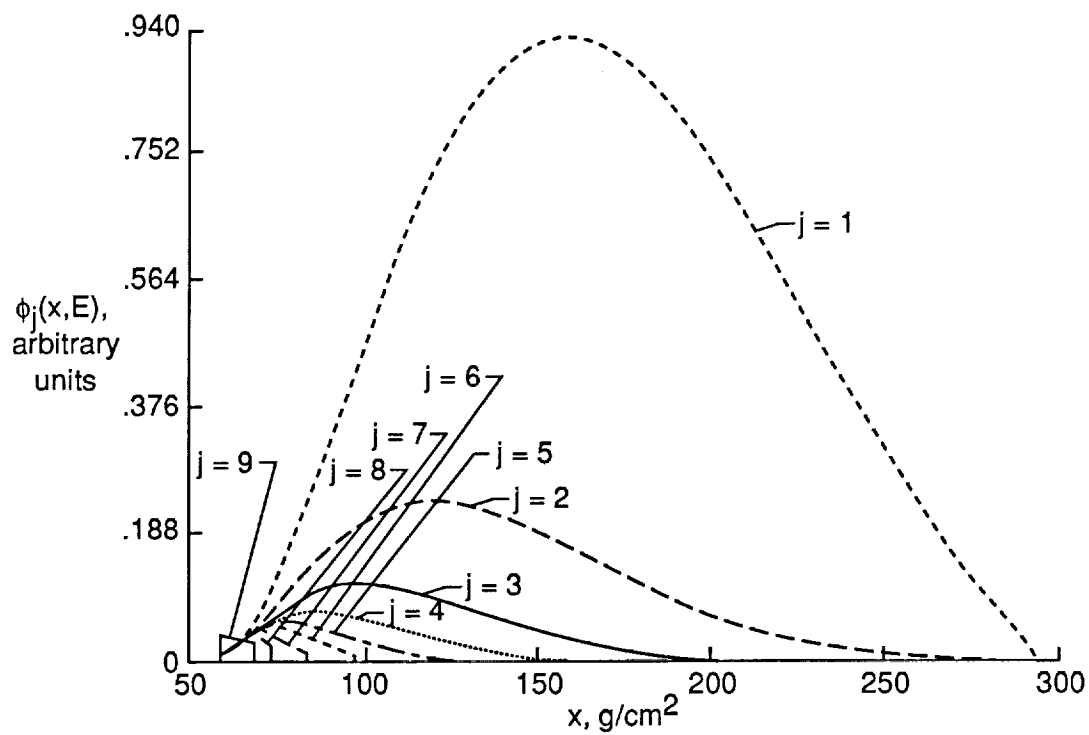


(a) $E = 995$ MeV/nucleon.

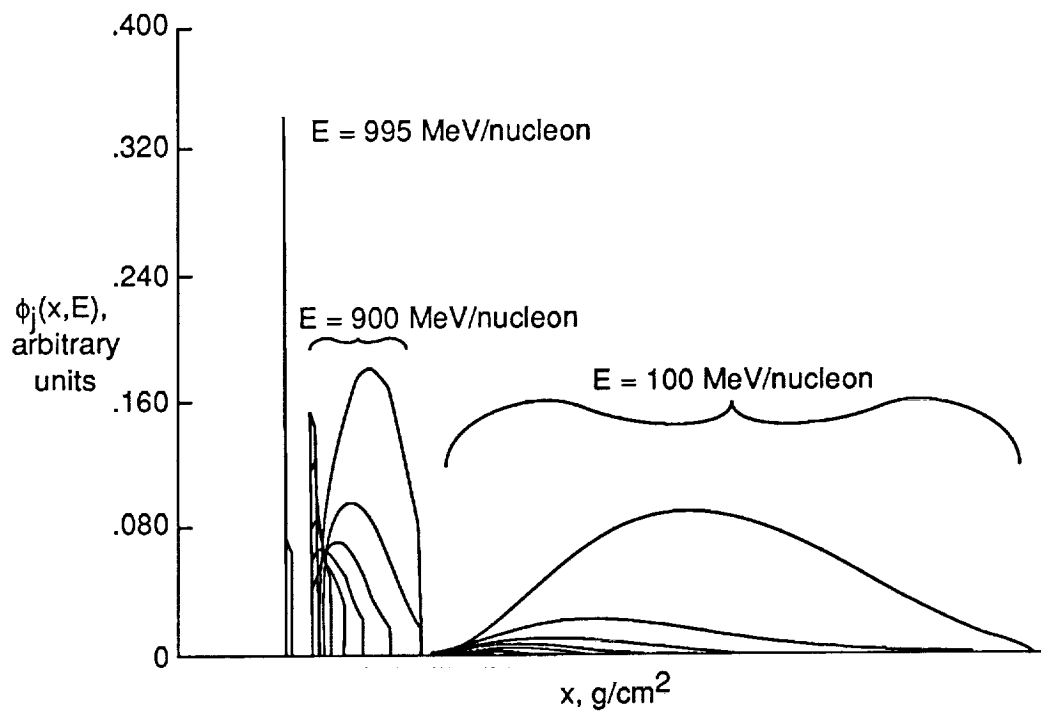


(b) $E = 950$ MeV/nucleon.

Figure 6. Variation of $\phi_j(x, E)$ with x for incident neon ($J = 10$) ions at 1 GeV/nucleon.

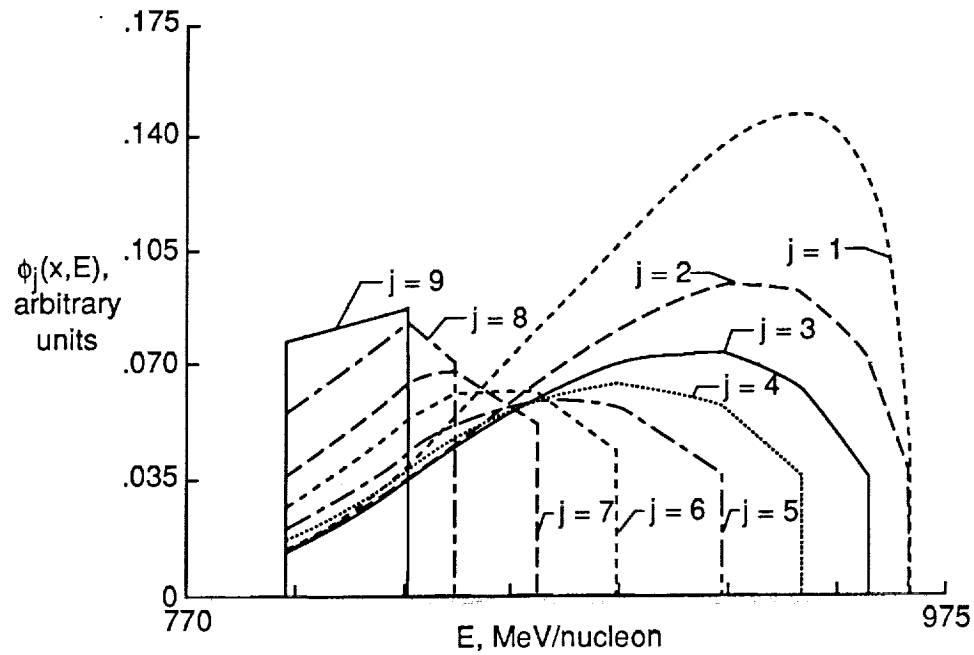


(c) $E = 100$ MeV/nucleon.

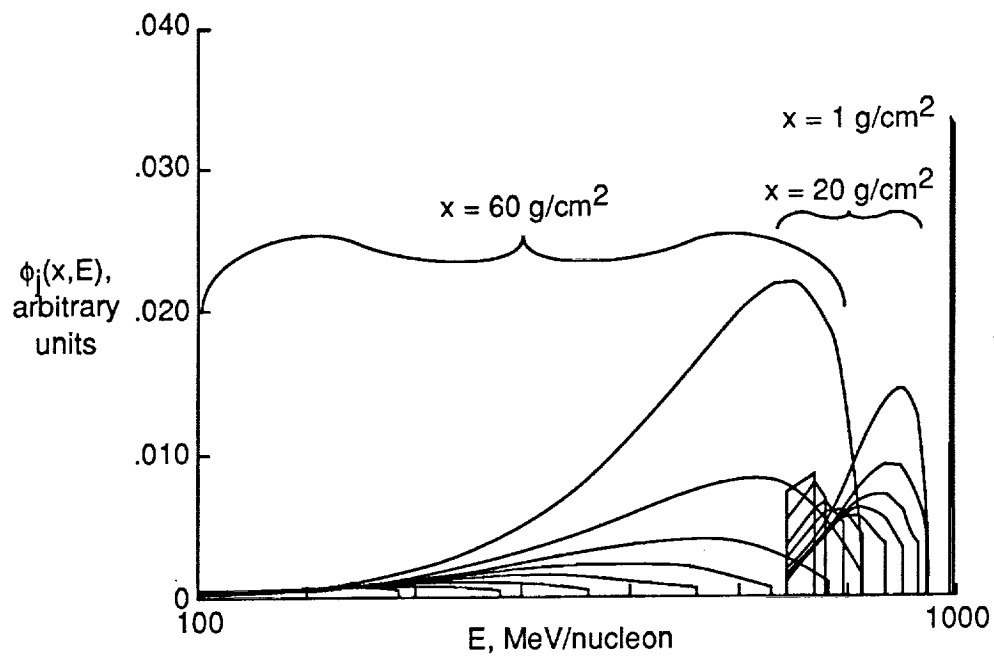


(d) Composite overlay of all three energies.

Figure 6. Concluded.

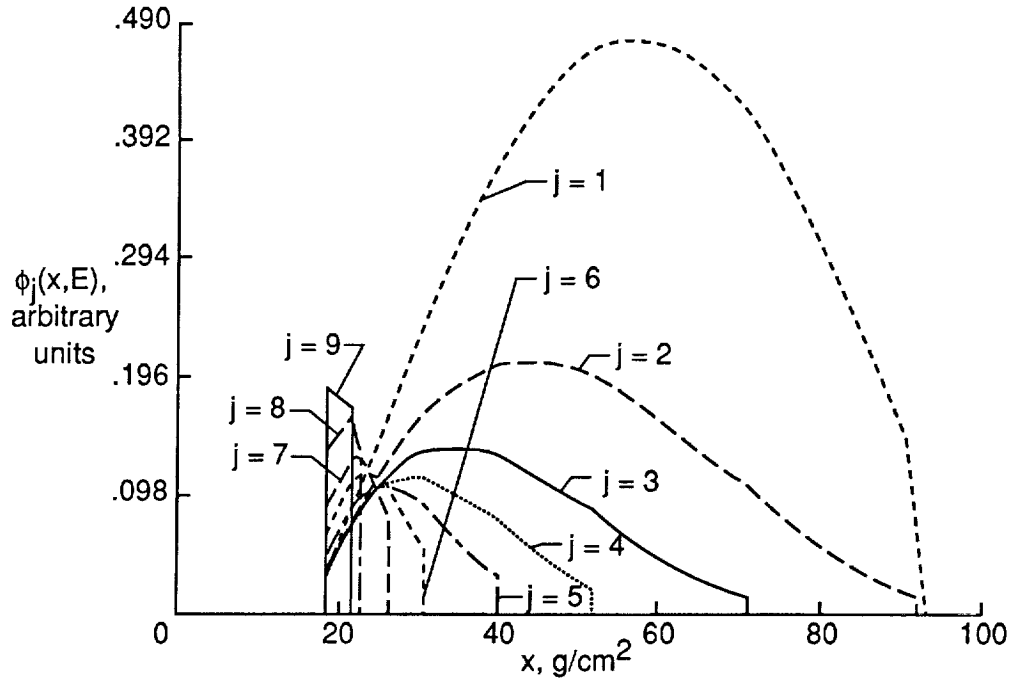


(a) $x = 20 \text{ g/cm}^2$.

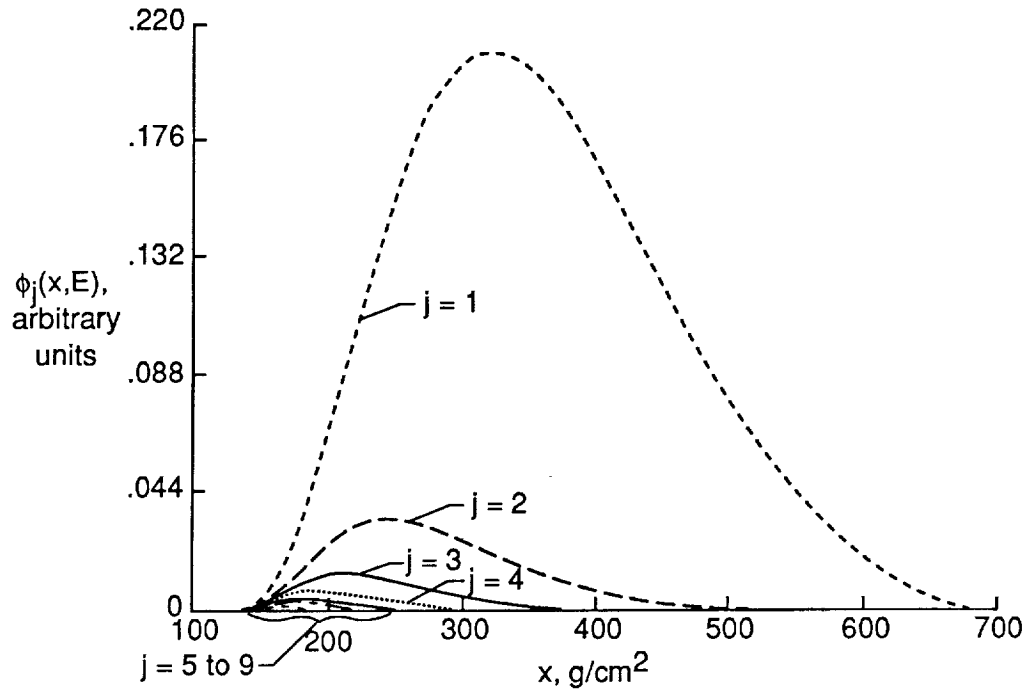


(b) $x = 1 \text{ g/cm}^2$, 20 g/cm^2 , and 60 g/cm^2 .

Figure 7. Variation of $\phi_j(x, E)$ with E for incident neon ($J = 10$) ions at 1 GeV/neutron.

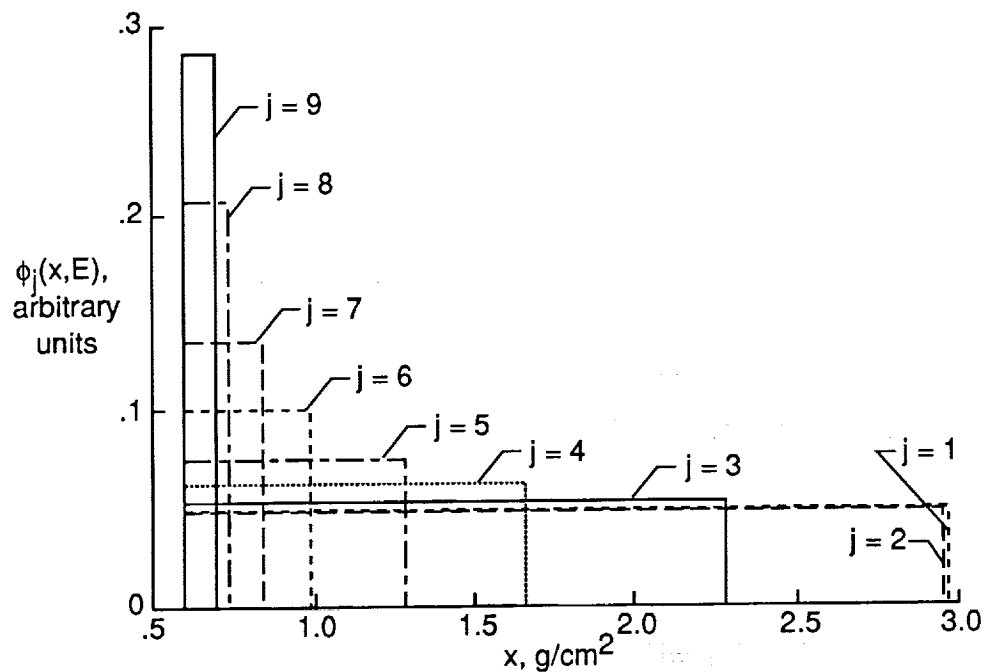


(a) $E_o = 500$ MeV/nucleon.

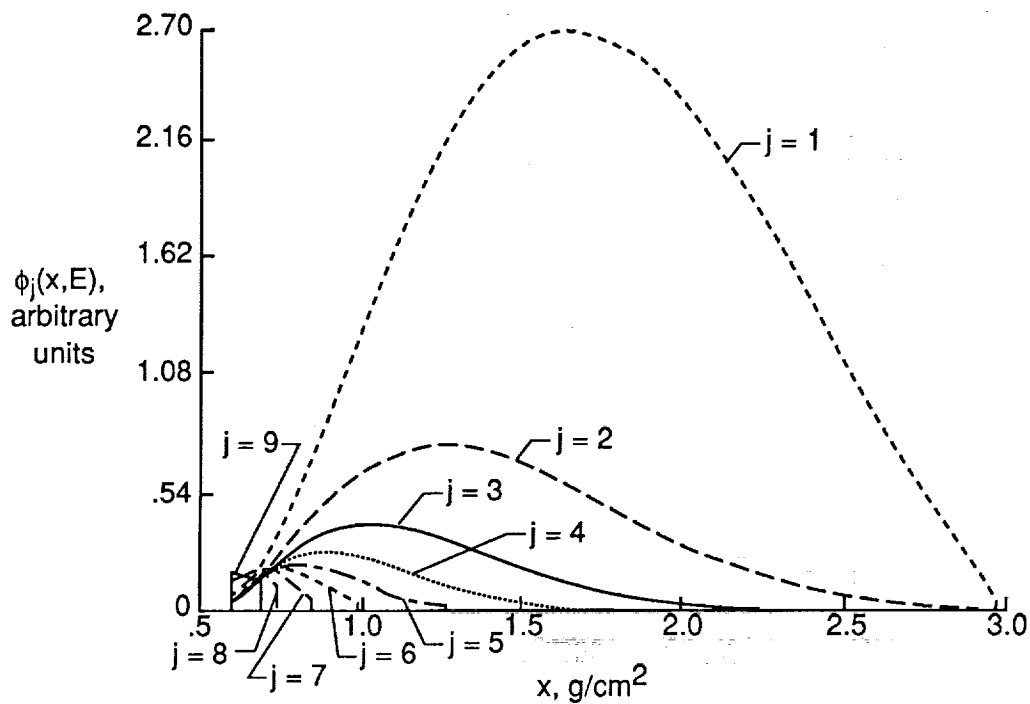


(b) $E_o = 2$ GeV/nucleon.

Figure 8. Sensitivity of flux at 100 MeV/nucleon to incident neon ($J = 10$) energy.

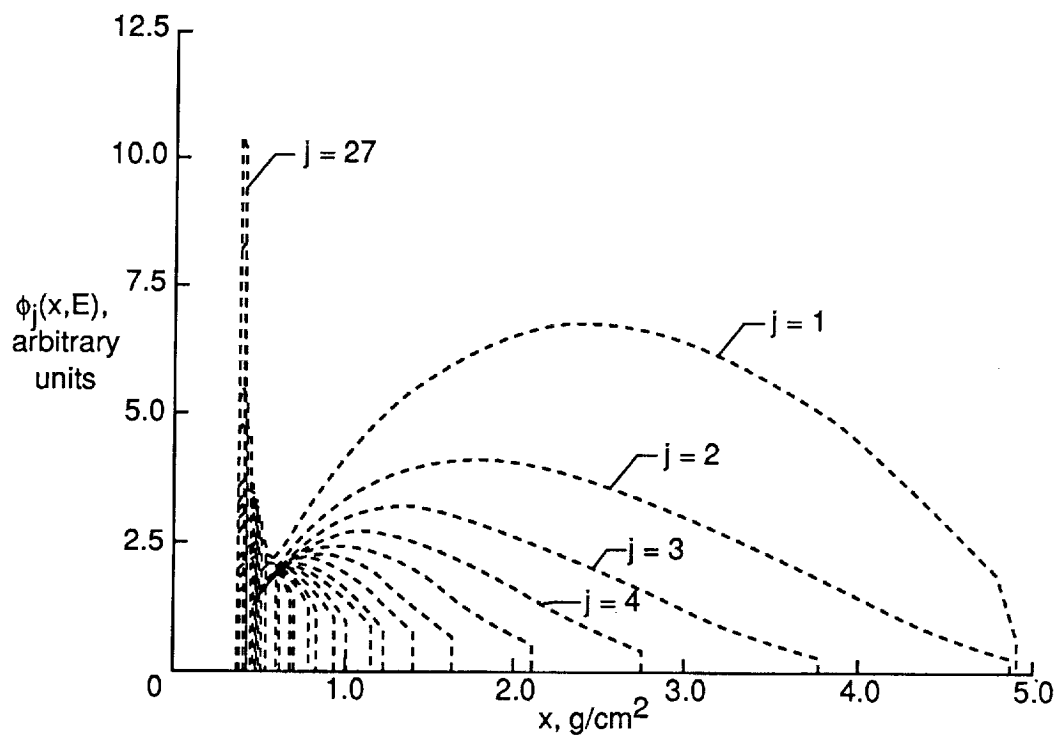


(a) $\bar{\sigma} = 10^{-4} \text{ cm}^2/\text{g}$ (rarefied shield).

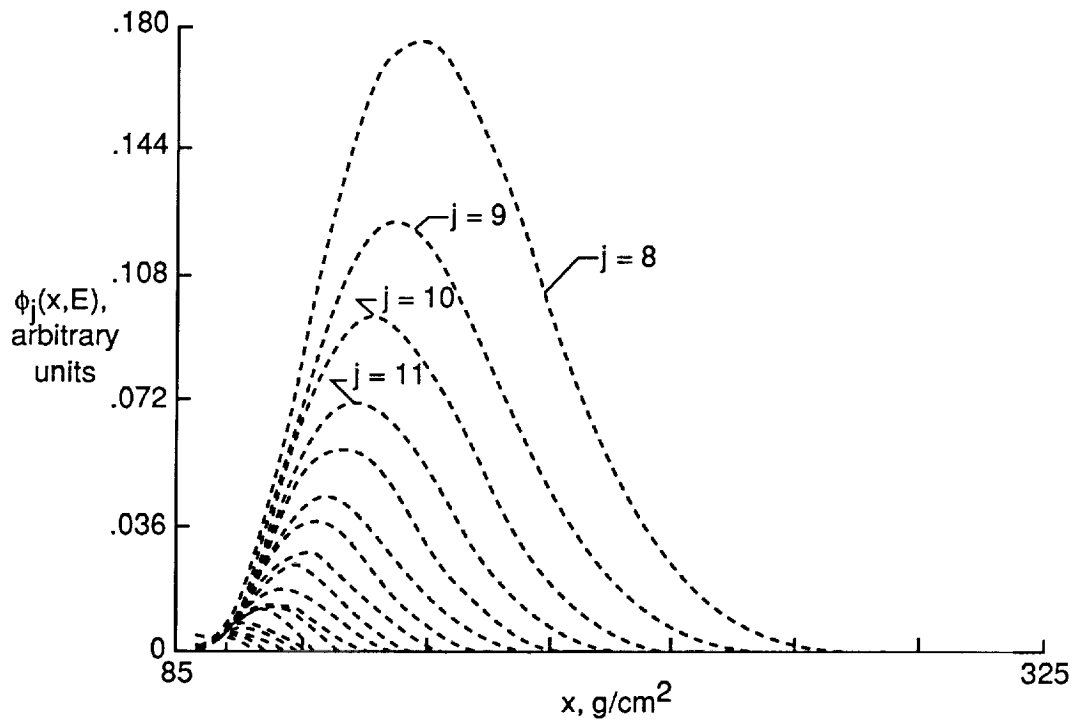


(b) $\bar{\sigma} = 1 \text{ cm}^2/\text{g}$ (dense shield).

Figure 9. Sensitivity of flux at 995 MeV/nucleon to incident neon ($J = 10$) ions at $E_0 = 1 \text{ GeV/nucleon}$ with cross-section normalization.

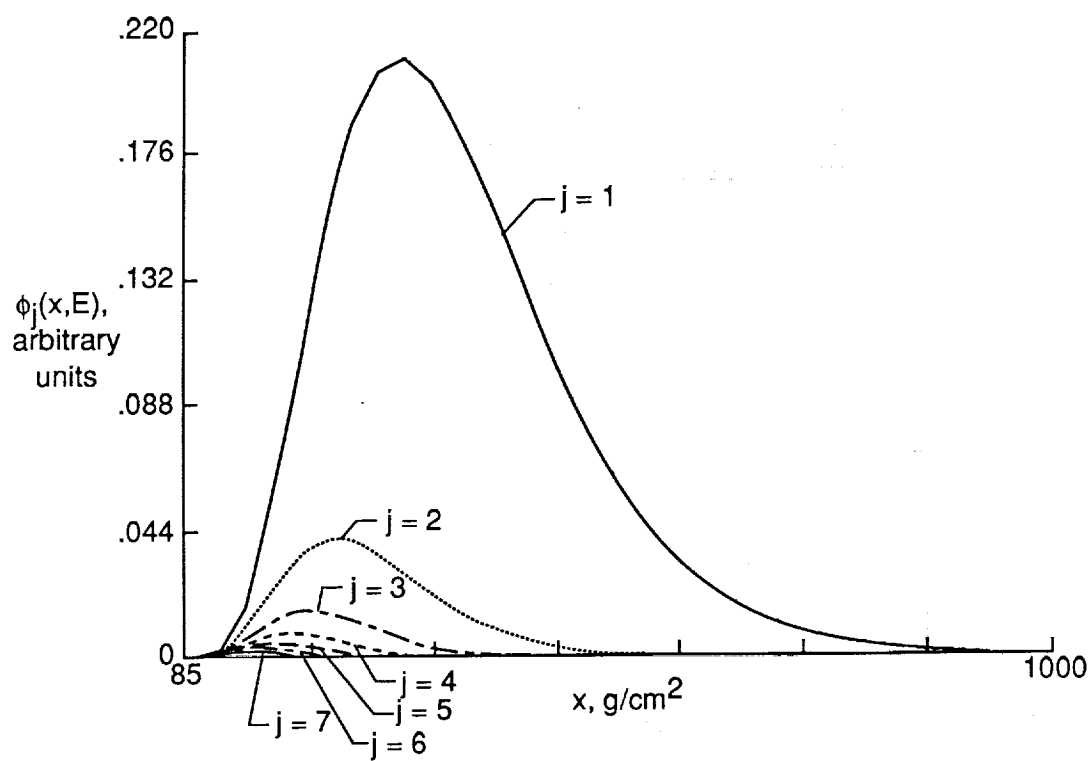


(a) $E = 4.995$ GeV/nucleon.



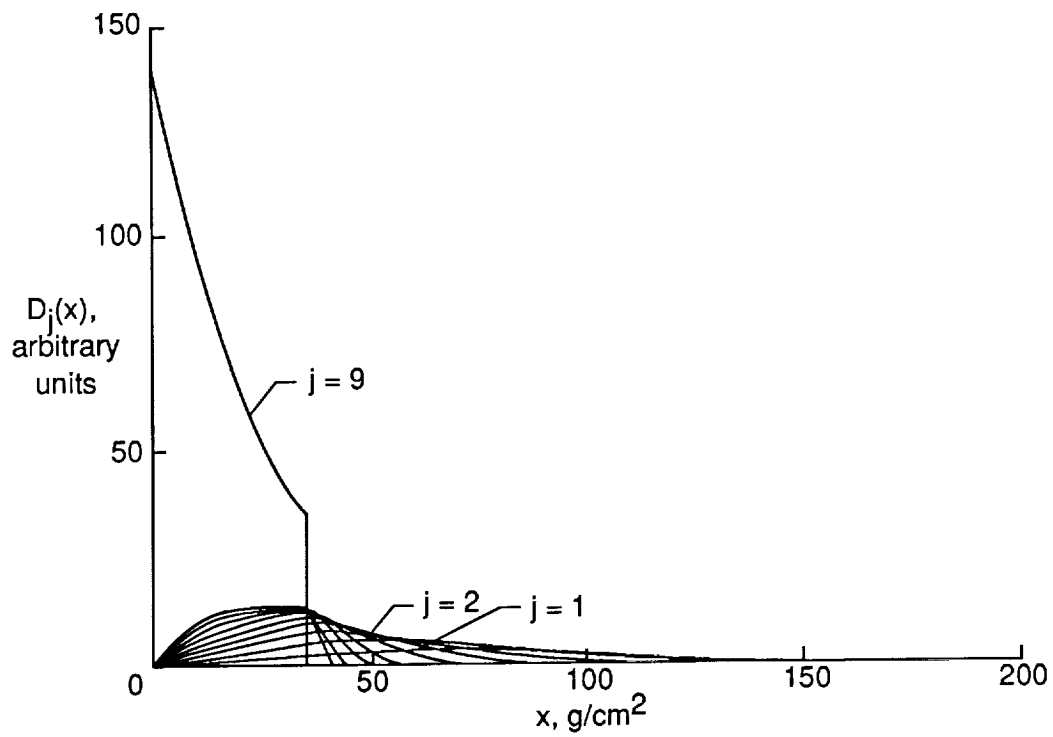
(b) $E = 2$ GeV/nucleon for $J \geq 8$.

Figure 10. Flux variation with x for incident nickel ($J = 28$) ions at 5 GeV/nucleon.

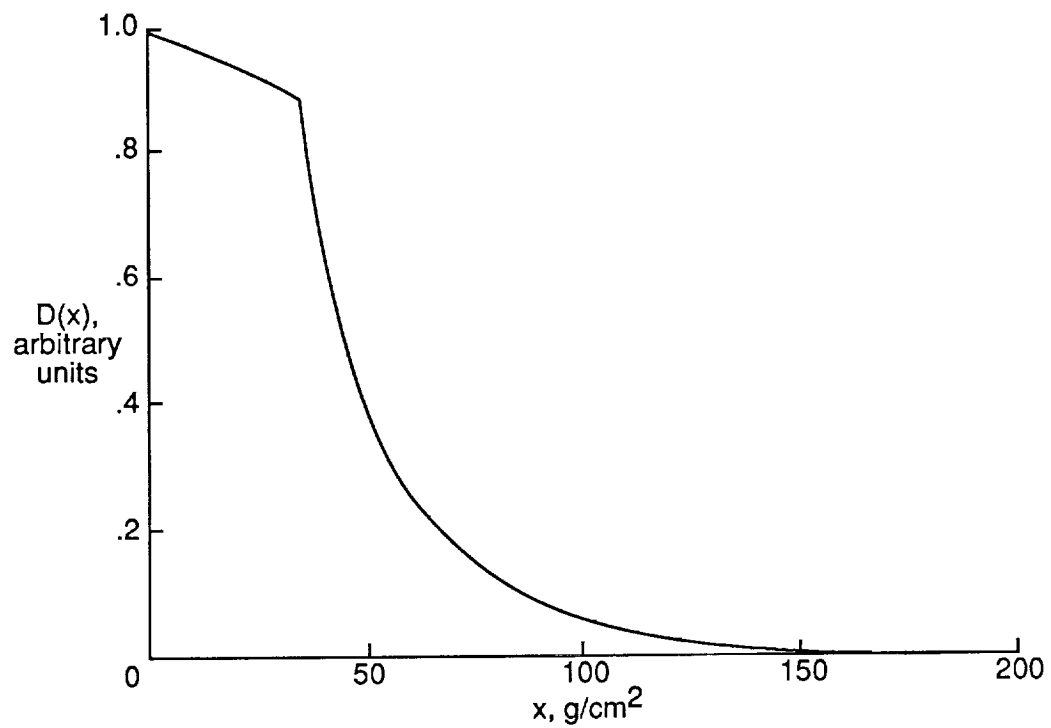


(c) $E = 2 \text{ GeV/nucleon}$ for $J \leq 7$.

Figure 10. Concluded.

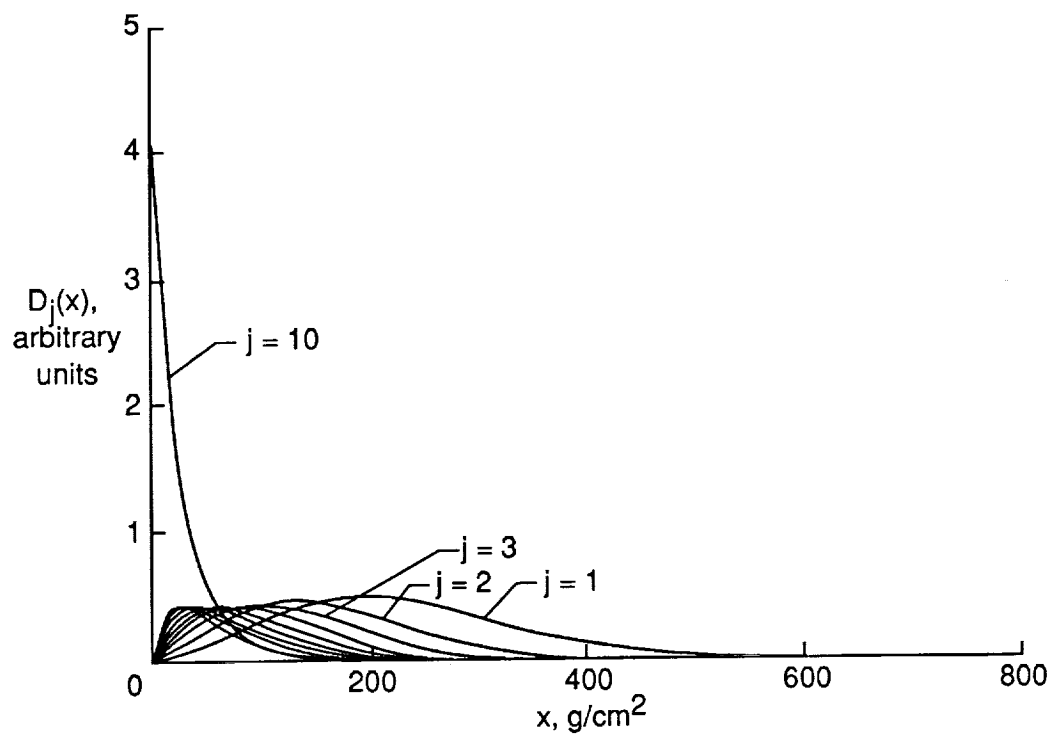


(a) Individual ions.

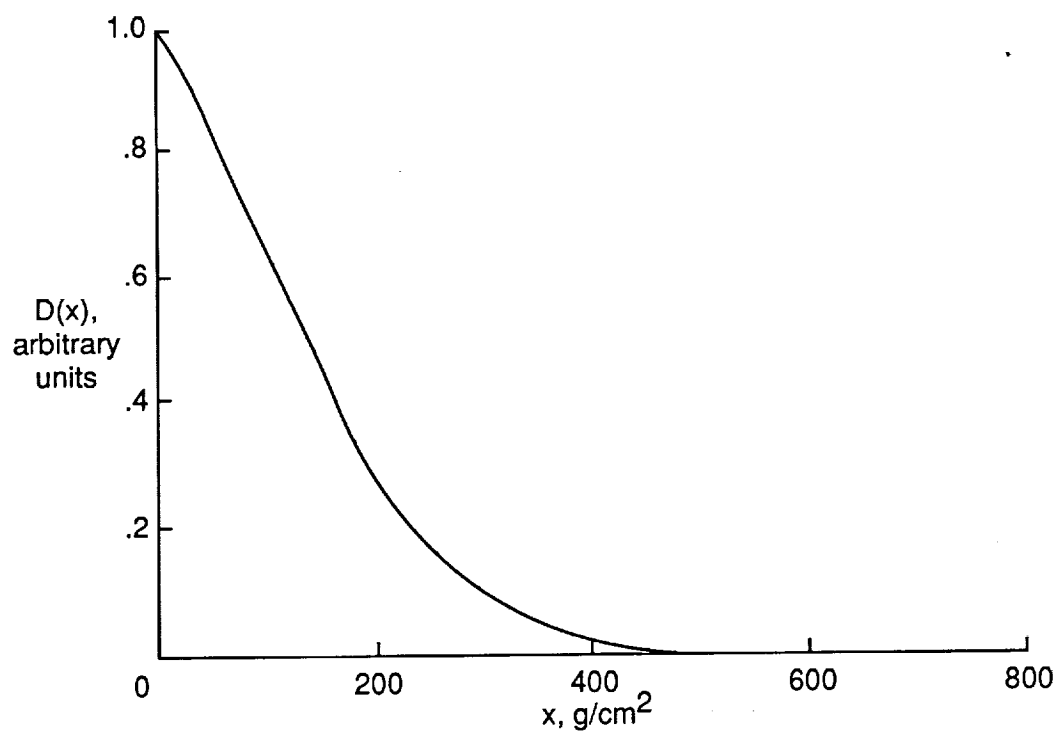


(b) Sum of all ions.

Figure 11. Dose profiles ($n_o = 1$) for incident neon ($J = 10$) ions at $E_o = 670$ MeV/nucleon.

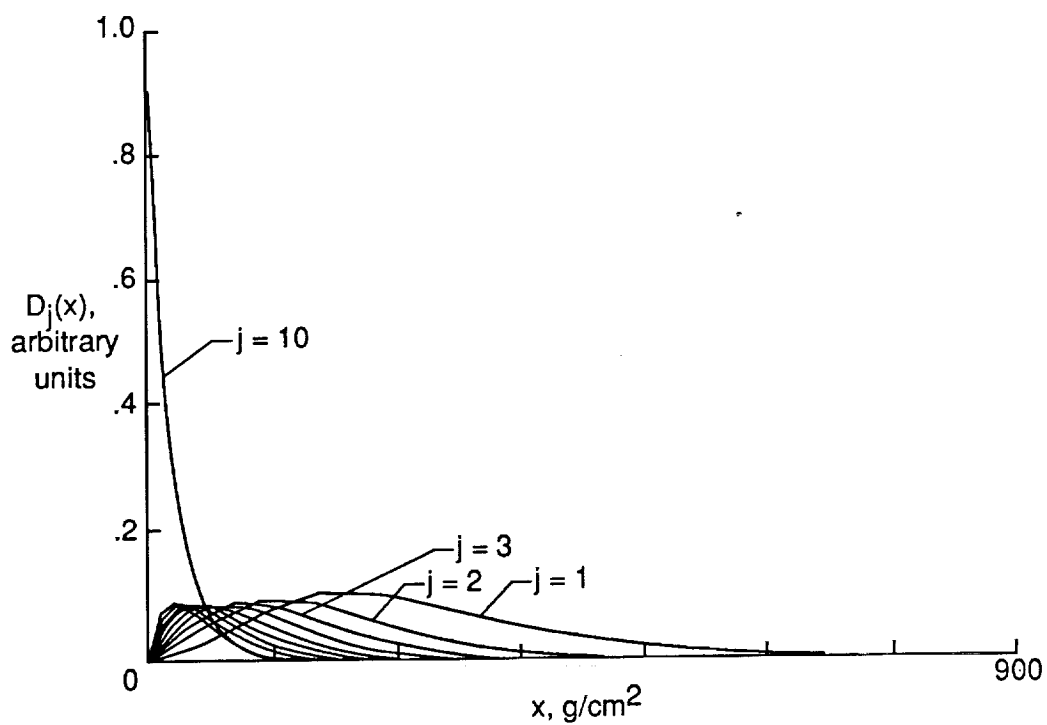


(a) Individual ions.

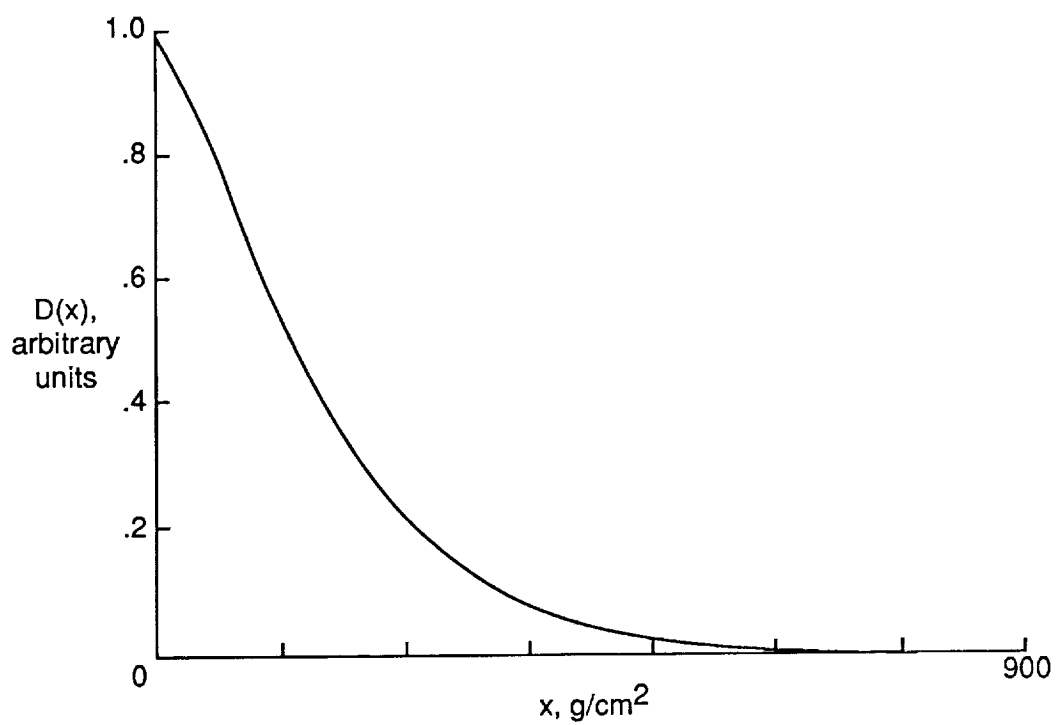


(b) Sum of all ions.

Figure 12. Dose profiles ($n_o = 1$) for incident neon ($J = 10$) ions at $E_o = 2$ GeV/nucleon.

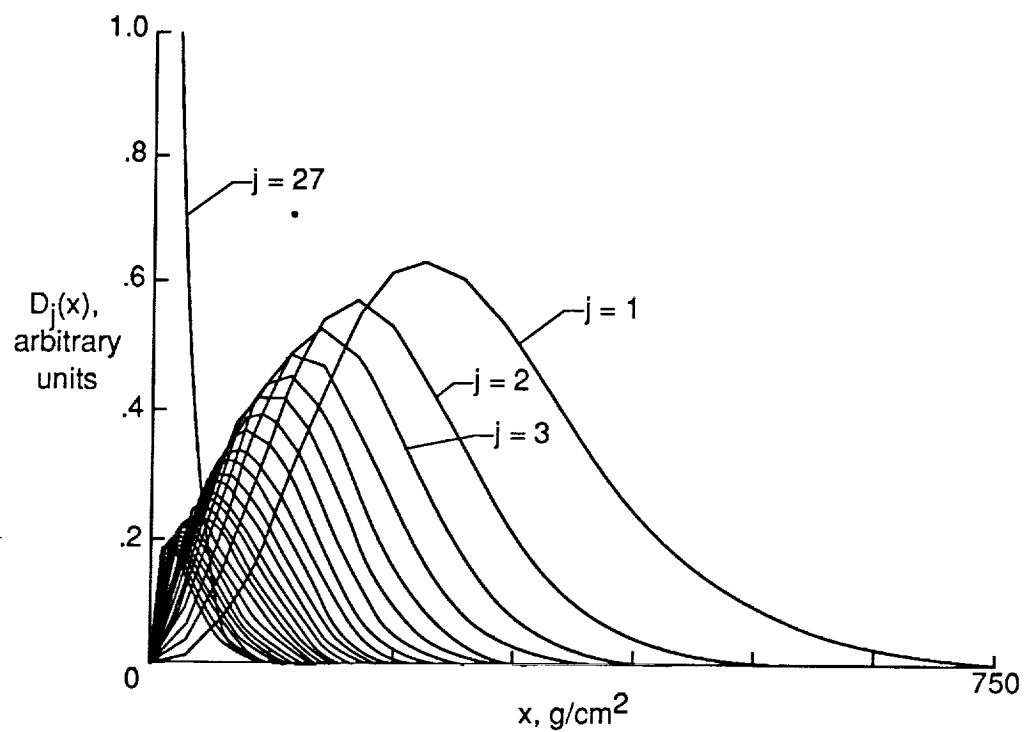


(a) Individual ions.

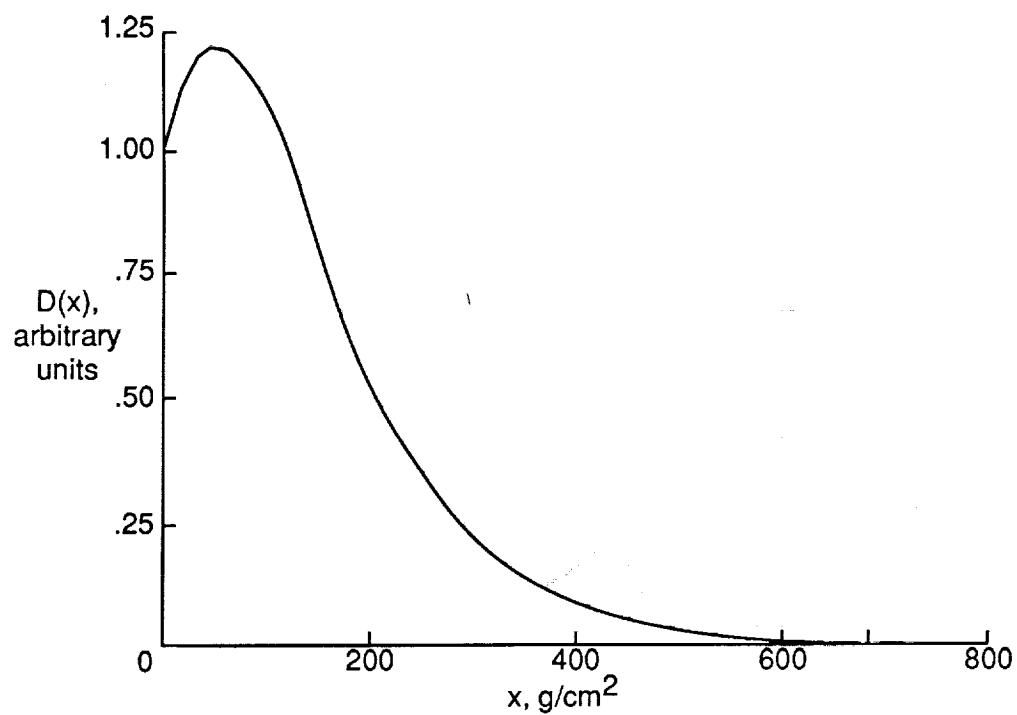


(b) Sum of all ions.

Figure 13. Dose profiles ($n_o = 1$) for incident neon ($J = 10$) ions at $E_o = 10$ GeV.

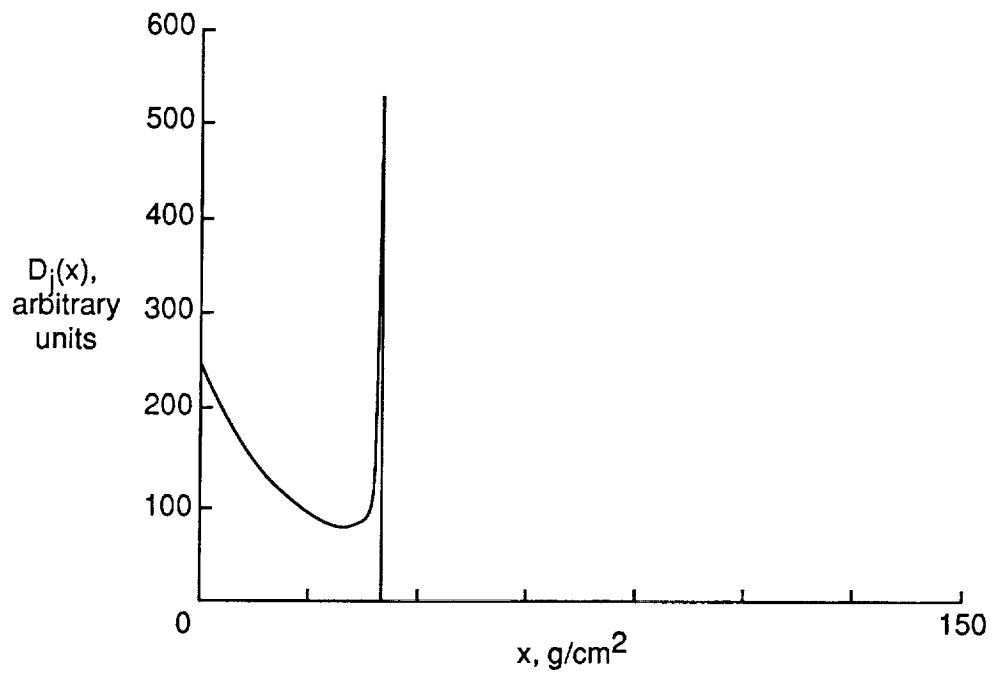


(a) Individual ions.

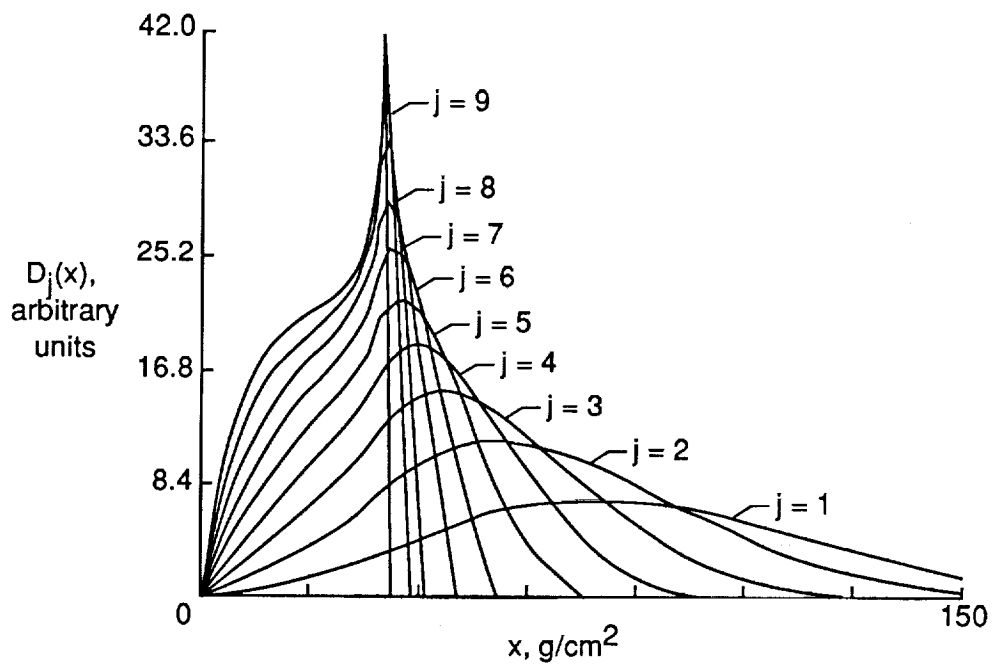


(b) Sum of all ions.

Figure 14. Dose profiles ($n_o = 1$) for incident cobalt ($J = 27$) ions at $E_o = 5$ GeV.

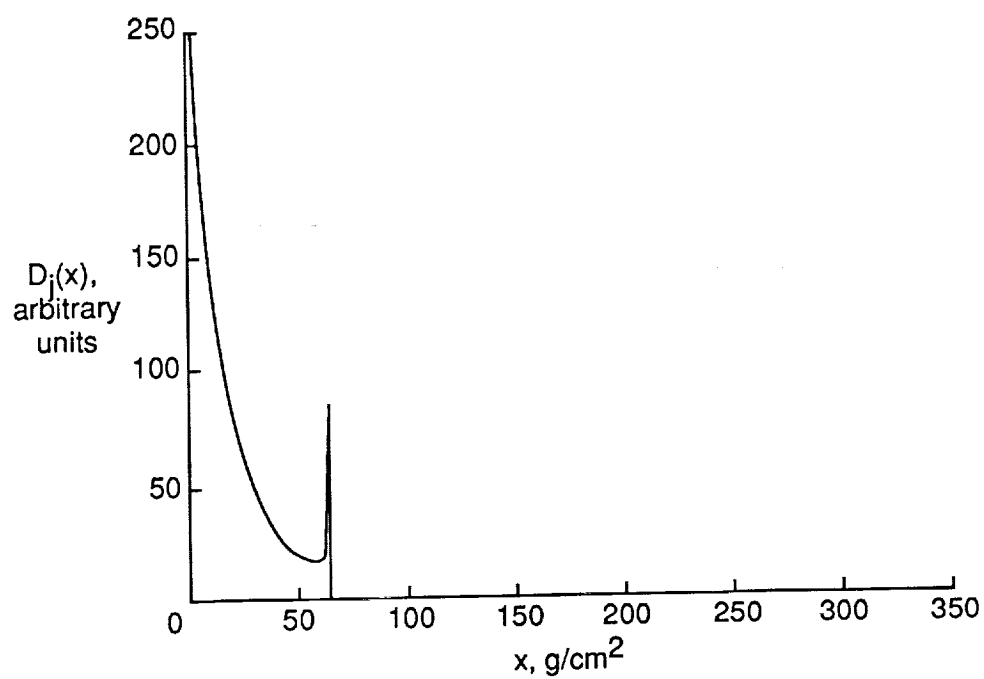


(a) $J = 10$.

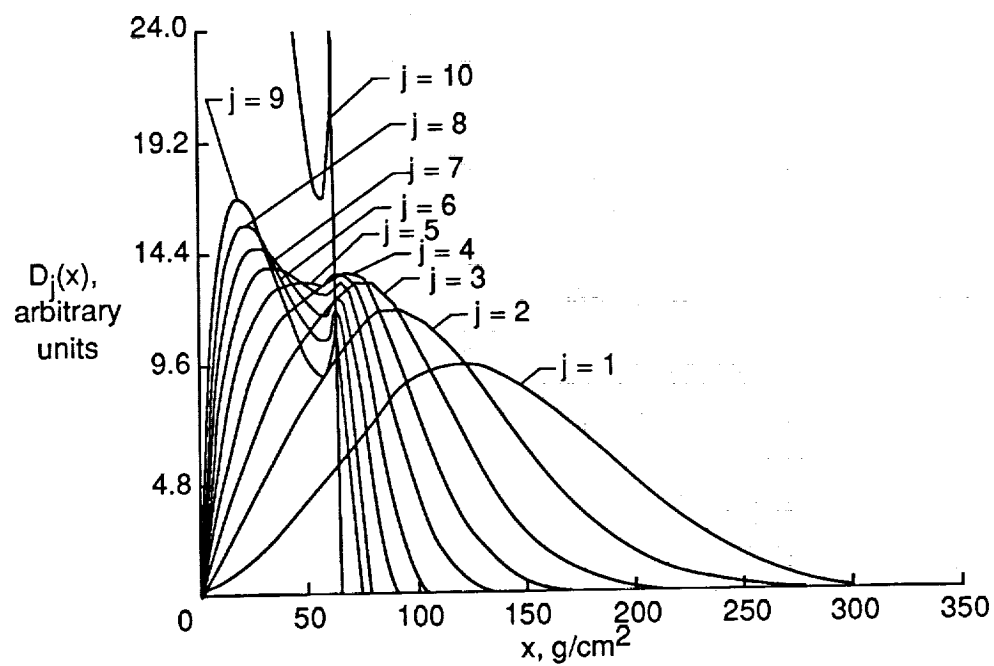


(b) $j < 10$.

Figure 15. Dose profiles ($n_o = 1.79$) for incident neon ($J = 10$) ions at $E_o = 670$ MeV/nucleon.

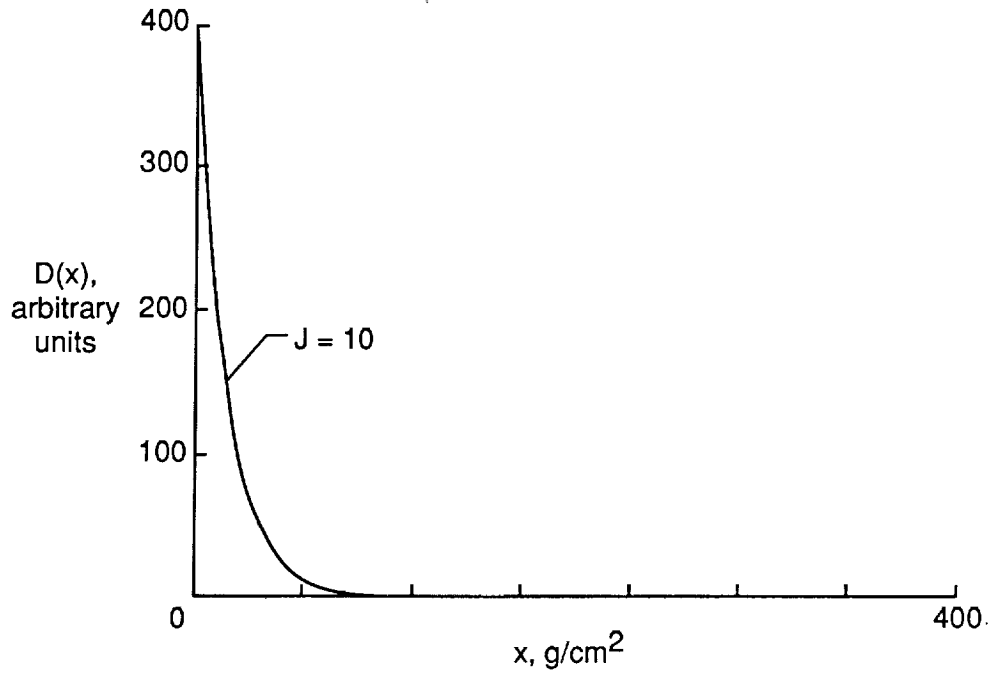


(a) $J = 10$.

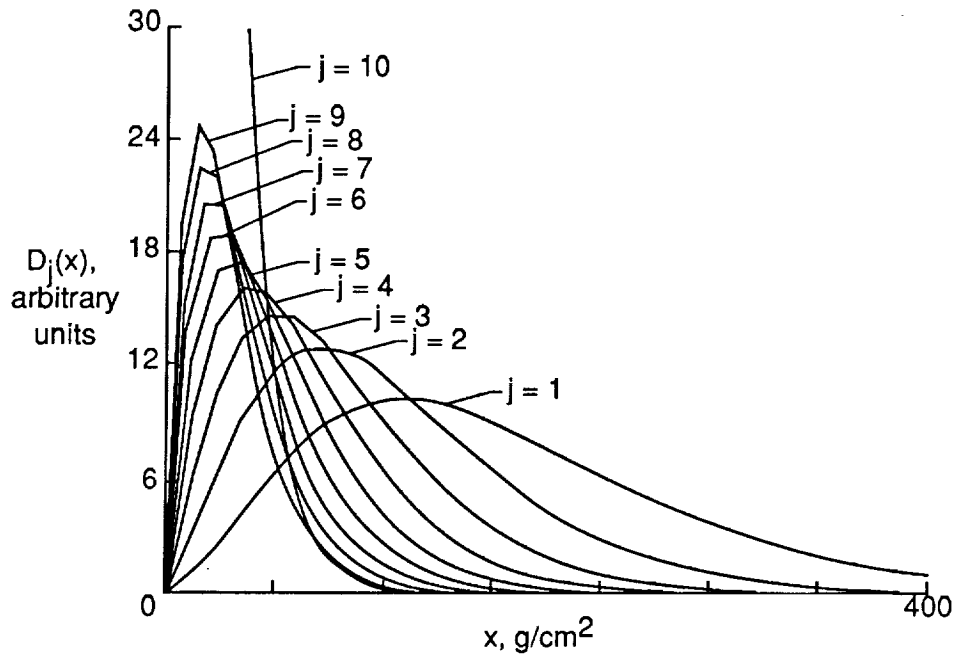


(b) $j \leq 10$.

Figure 16. Dose profiles ($n_o = 1.79$) for incident neon ($J = 10$) ions at $E_o = 1$ GeV/nucleon.



(a) $J = 10$.



(b) $j \leq 10$.

Figure 17. Dose profiles ($n_o = 1.79$) for incident neon ($J = 10$) ions at $E_o = 3 \text{ GeV/nucleon}$.

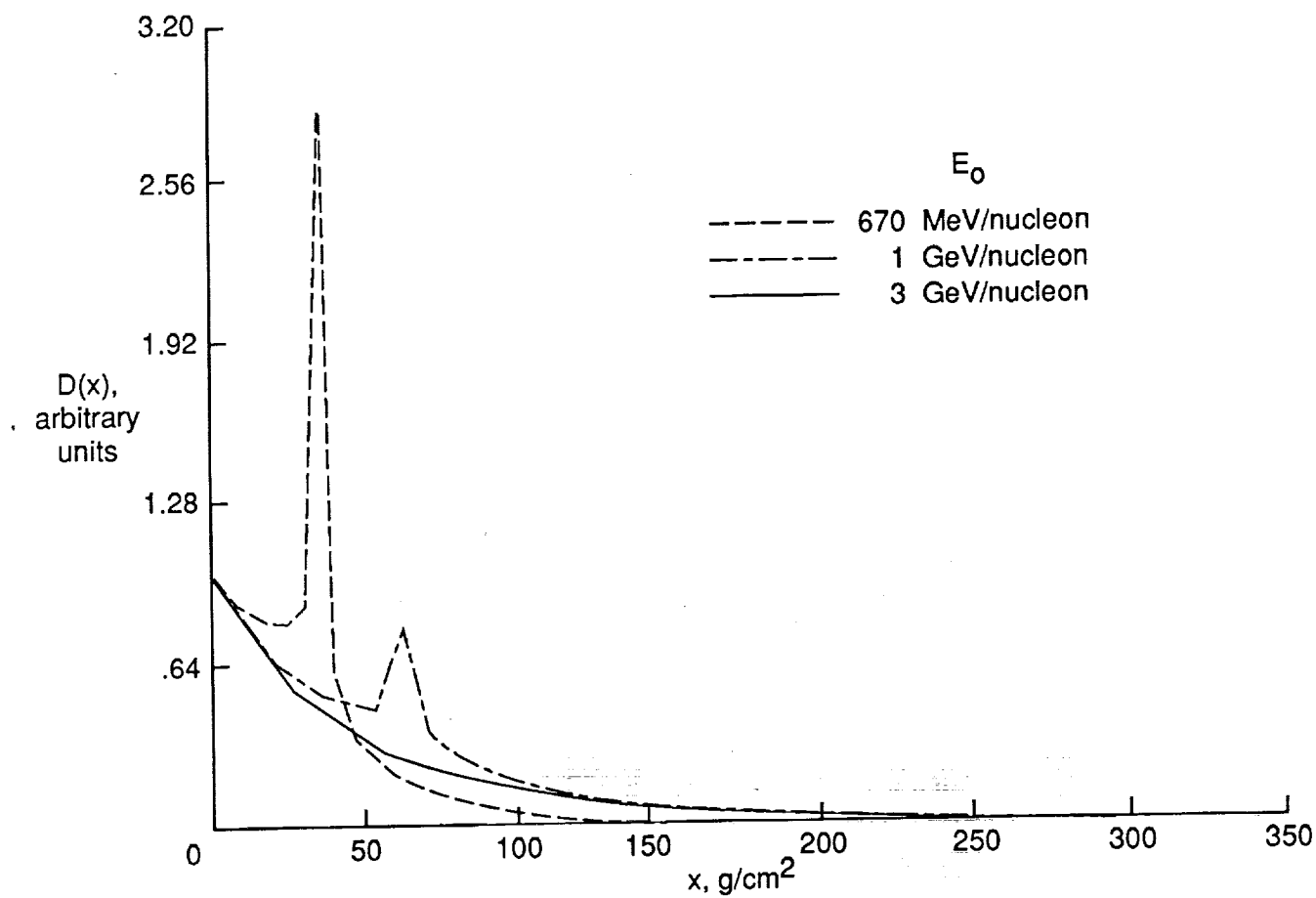
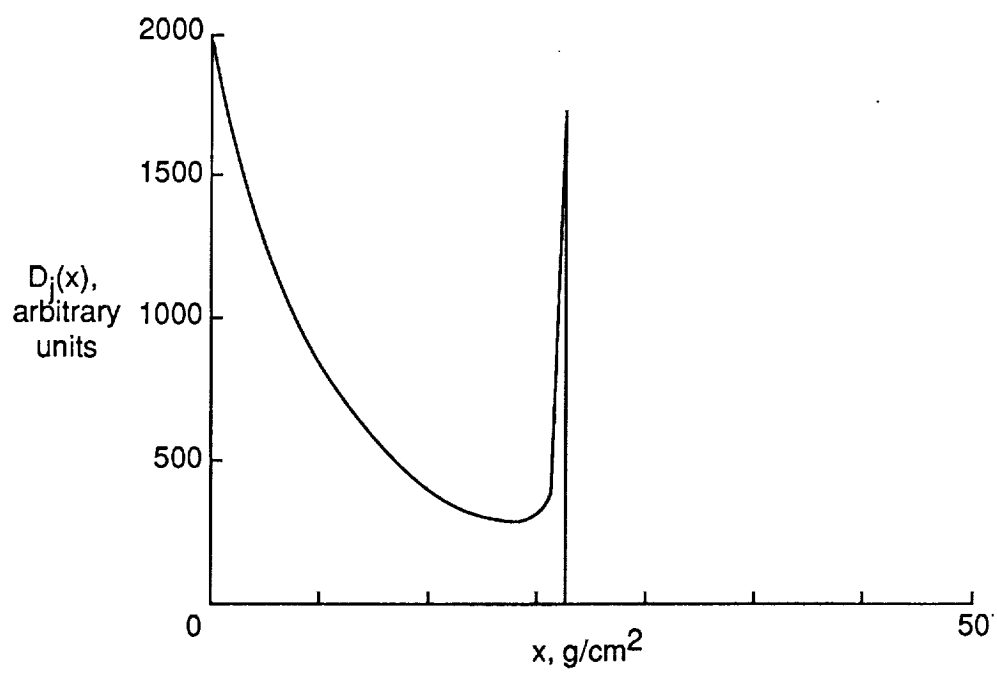
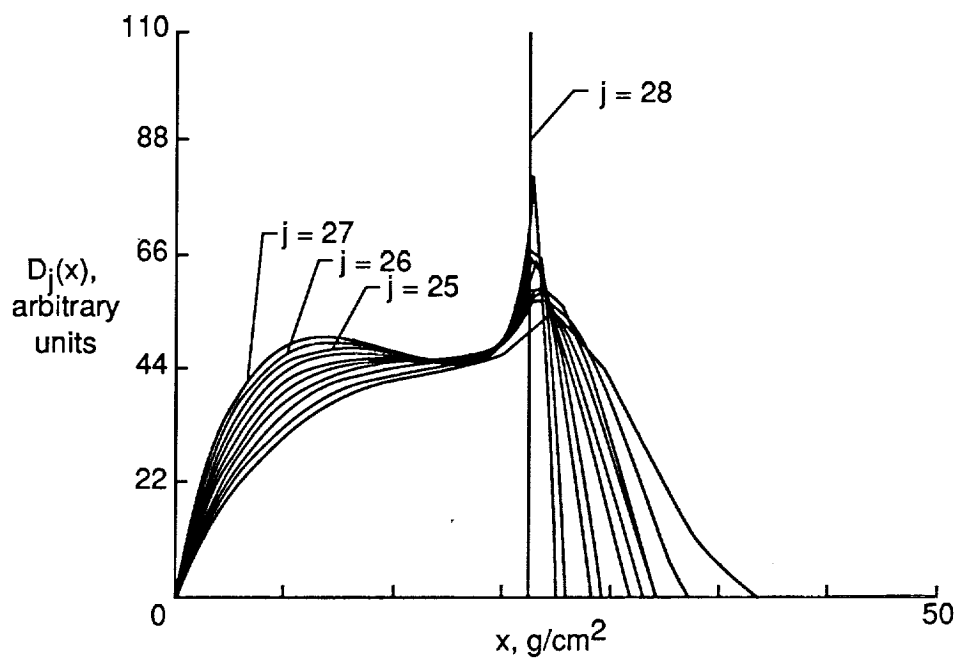


Figure 18. Total dose for previous cases.



(a) $J = 28$.



(b) $28 \leq j \leq 18$.

Figure 19. Dose profiles ($n_o = 1.79$) for incident nickel ($J = 28$) ions at $E_o = 1$ GeV/nucleon.

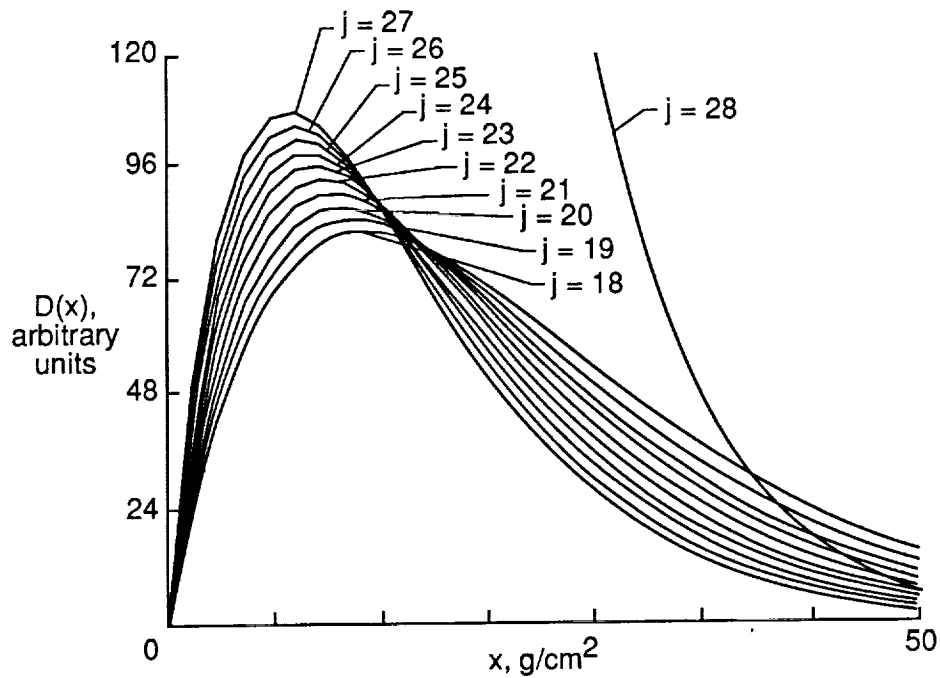


Figure 20. Dose profiles ($n_o = 1.79$) for incident nickel ($J = 28$) ions at $E_o = 5$ GeV/nucleon.

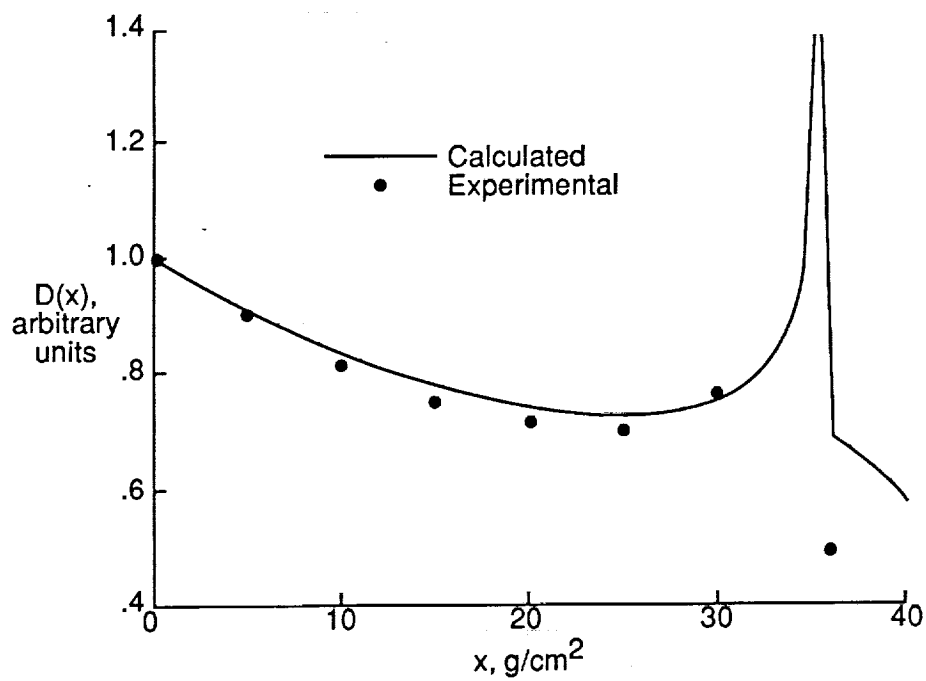
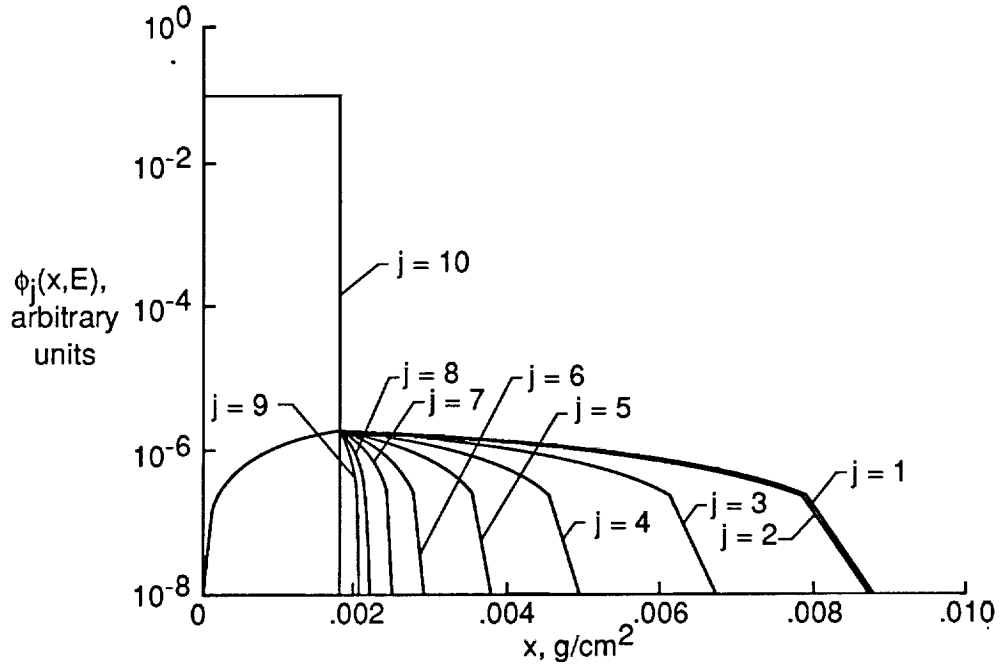
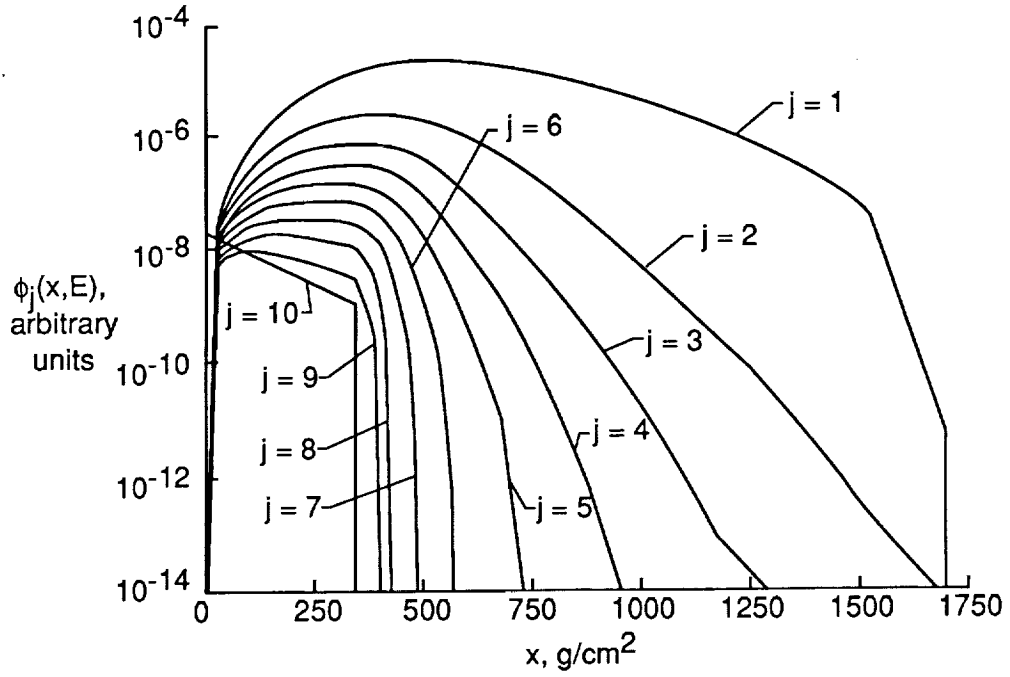


Figure 21. Experimental dose comparison for incident neon ions ($J = 10$) on water ($\bar{\sigma} \approx 1.5 \times 10^{-2} \text{ cm}^2/\text{g}$).

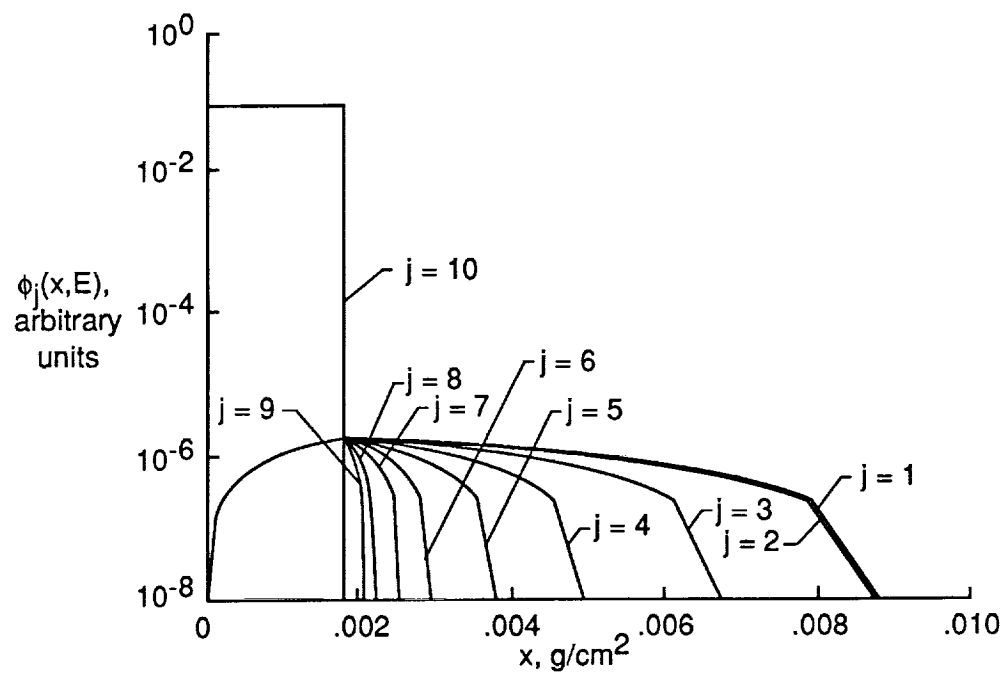


(a) $E = 9999.9$ MeV/nucleon.

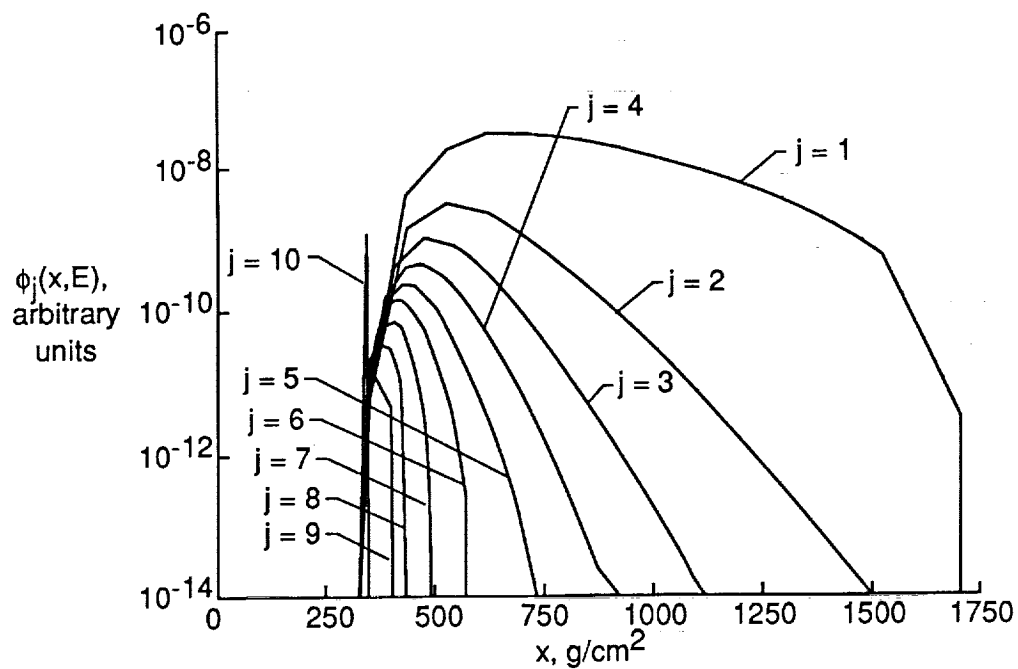


(b) $E = 1$ GeV/nucleon.

Figure 22. Flux profiles for analytic distributed source of incident neon ($J = 10$) ions with $M_o = 0.01$.

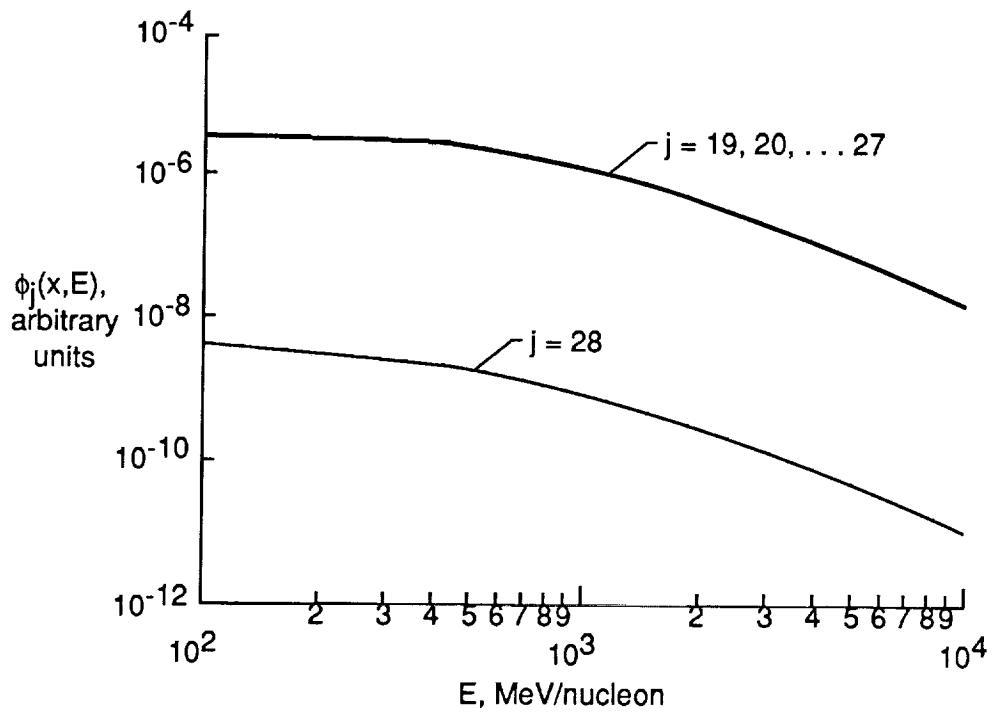


(a) $E = 9999.9$ MeV/nucleon.

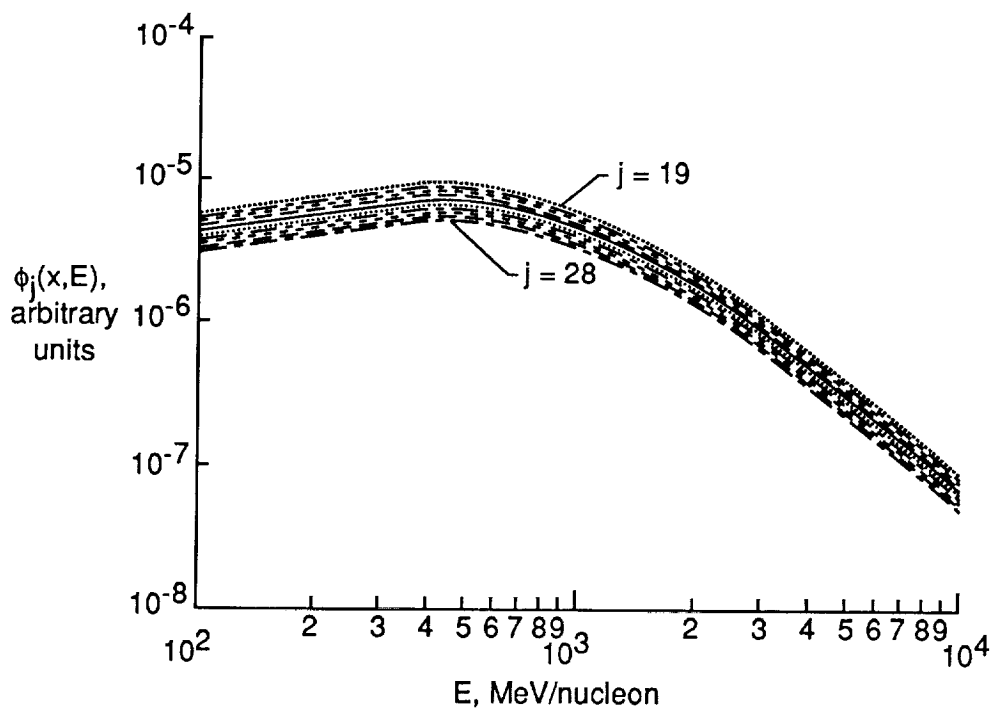


(b) $E = 1$ GeV/nucleon.

Figure 23. Flux profiles for analytic distributed source of incident neon ($J = 10$) ions with $M_o = 1.0$.

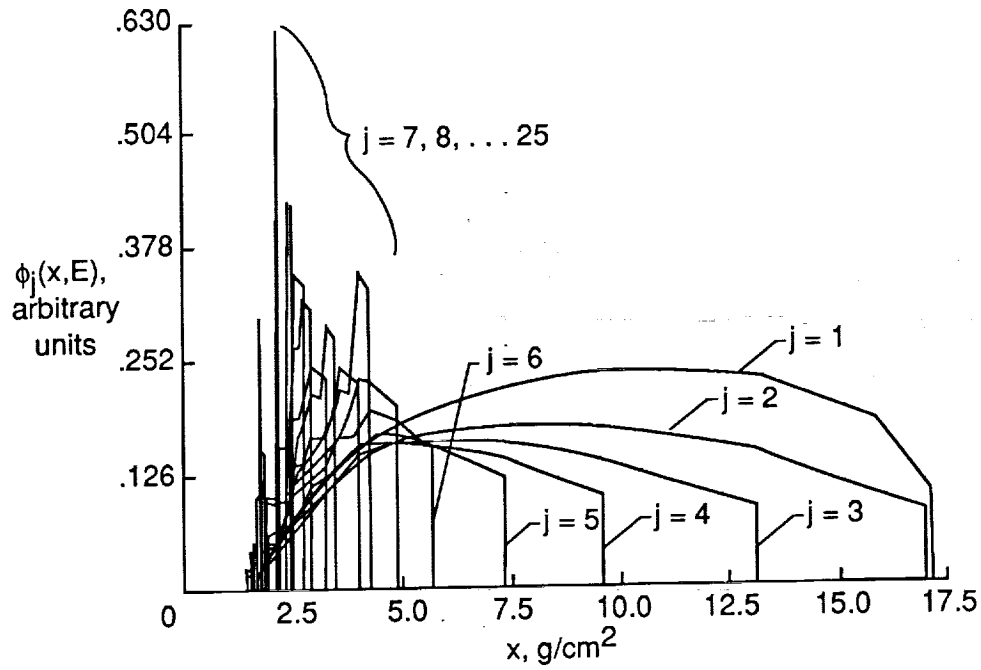


(a) $x = 1 \text{ g/cm}^2$.

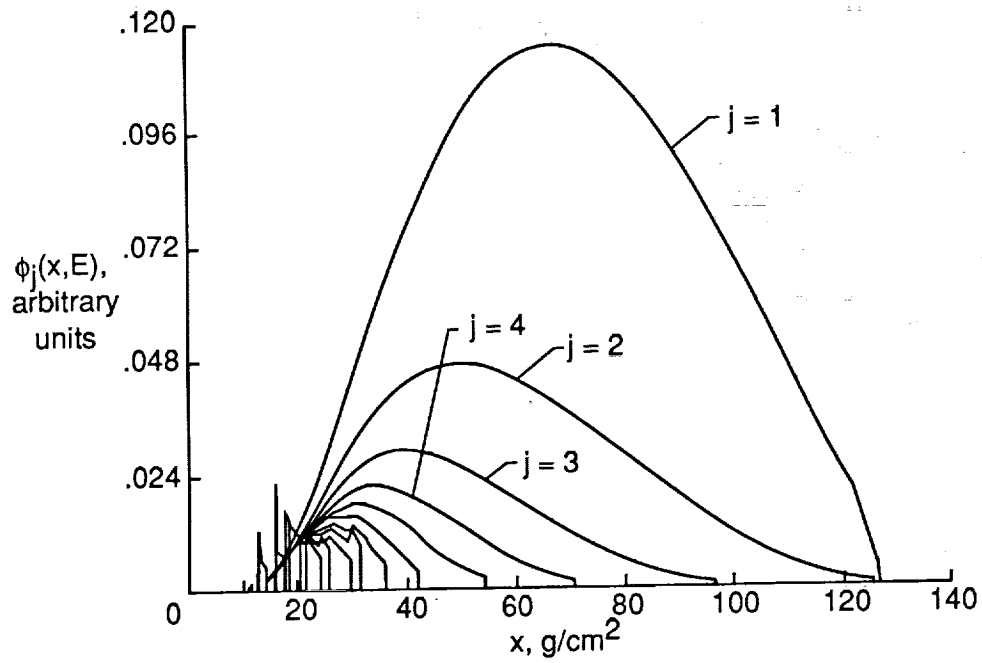


(b) $x = 10 \text{ g/cm}^2$.

Figure 24. Flux profiles for solar source for incident nickel ($J = 28$) ions.

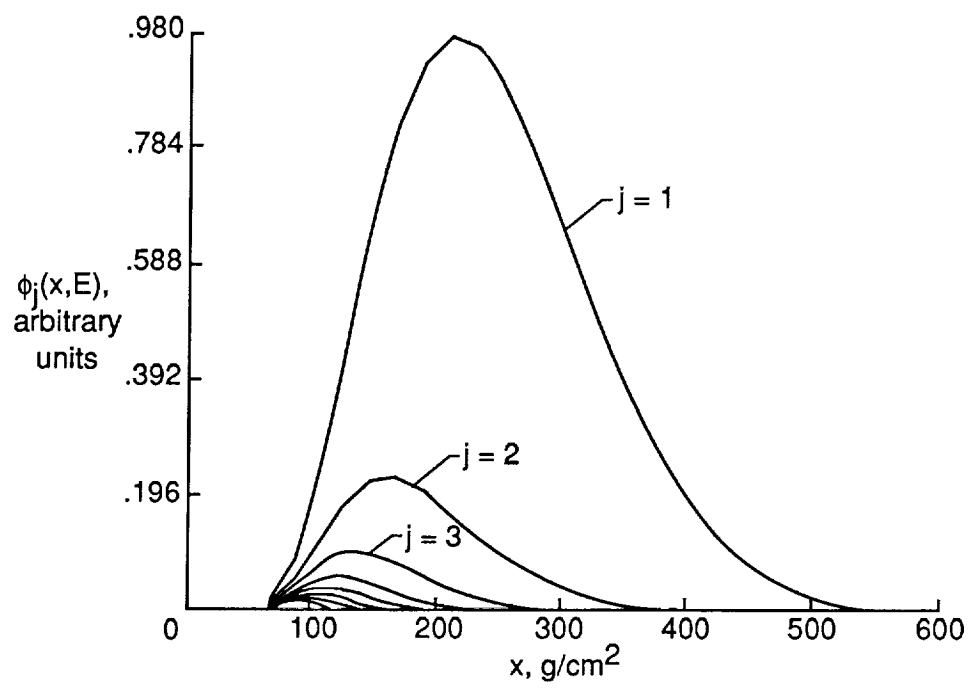


(a) $E = 4.9$ GeV/nucleon.



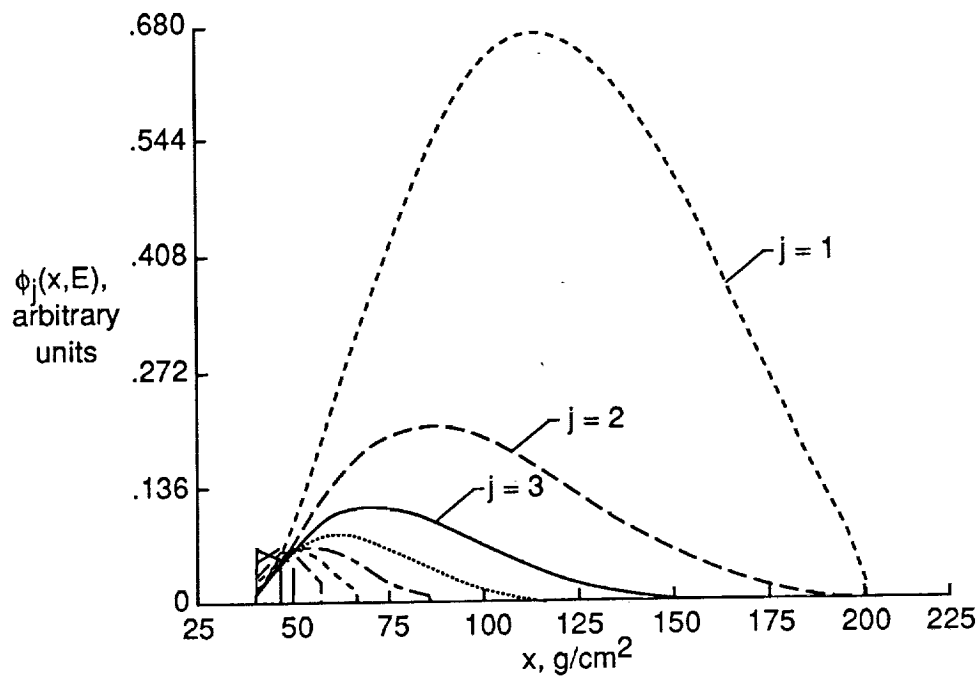
(b) $E = 4.3$ GeV/nucleon.

Figure 25. Flux profiles for a composite beam of neon through iron ions at $E_o = 5$ GeV/nucleon.

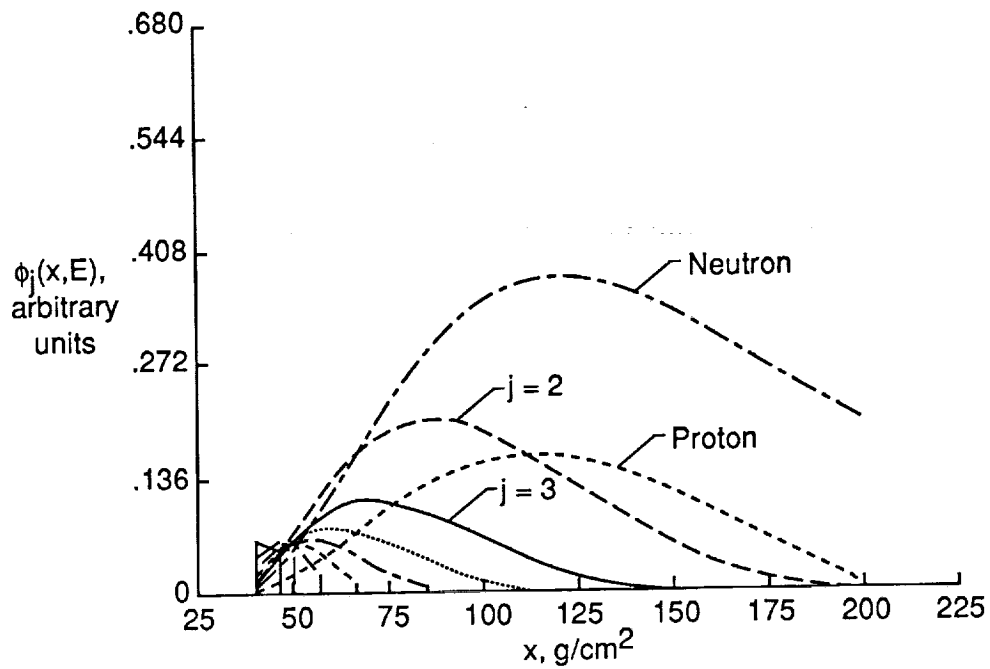


(c) $E = 2.5$ GeV/nucleon.

Figure 25. Concluded.

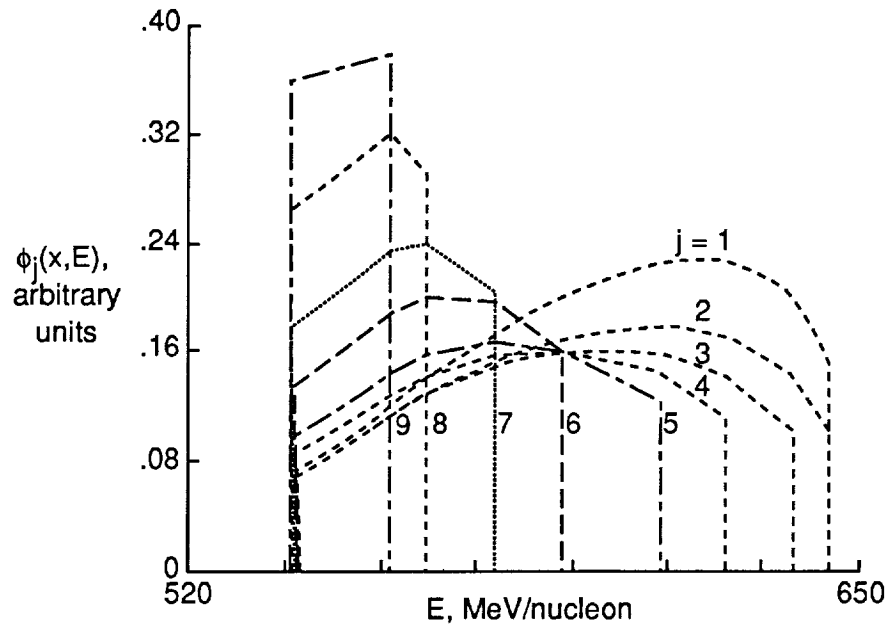


(a) $f_n = 0$ (no neutrons).

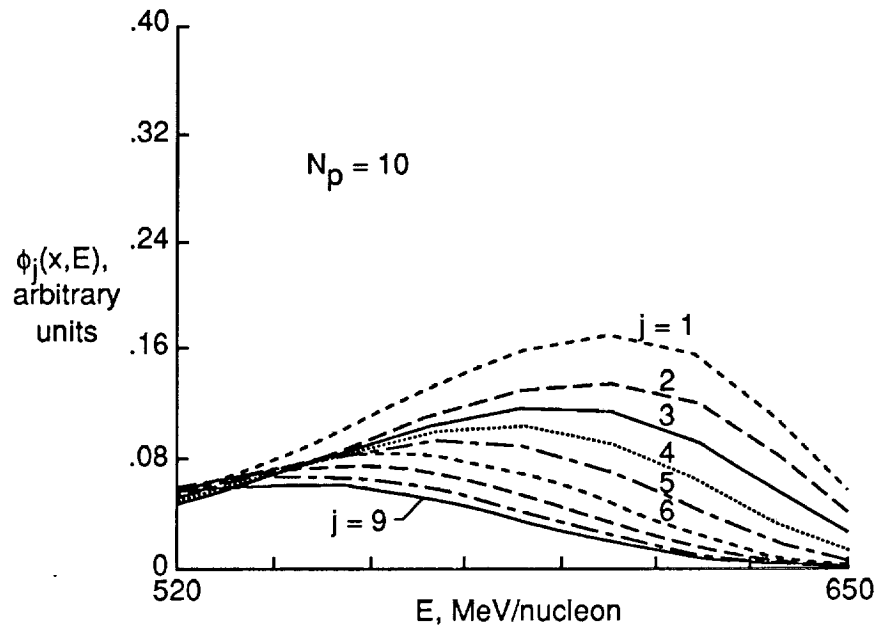


(b) $f_n = 0.5$.

Figure 26. Distinction between neutrons and protons at $E = 500$ MeV/nucleon for incident neon ($J = 10$) ions at $E_0 = 1$ GeV.

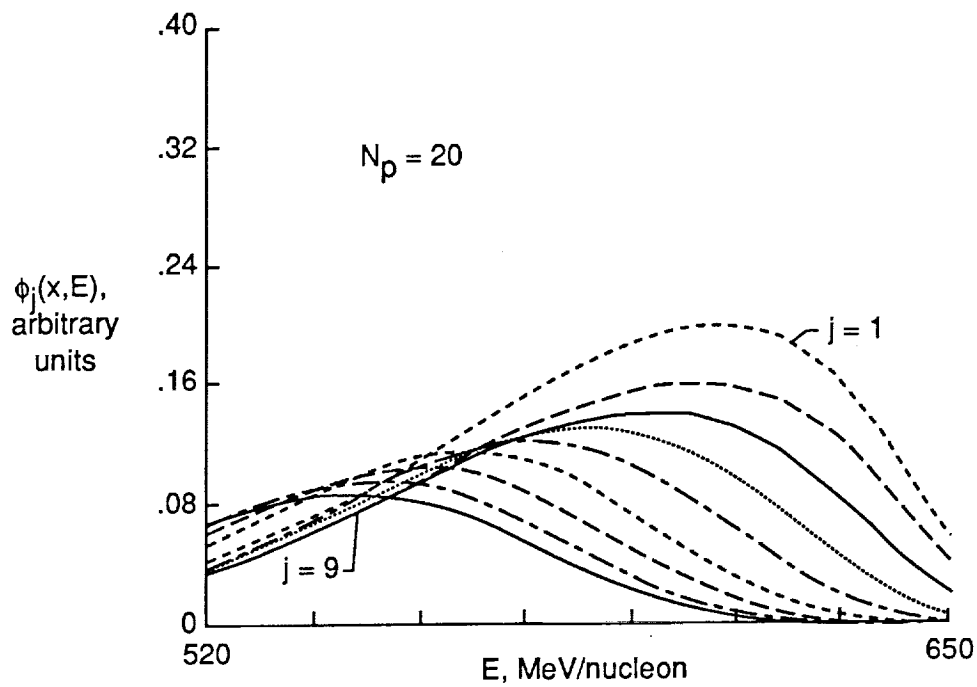


(a) Exact.

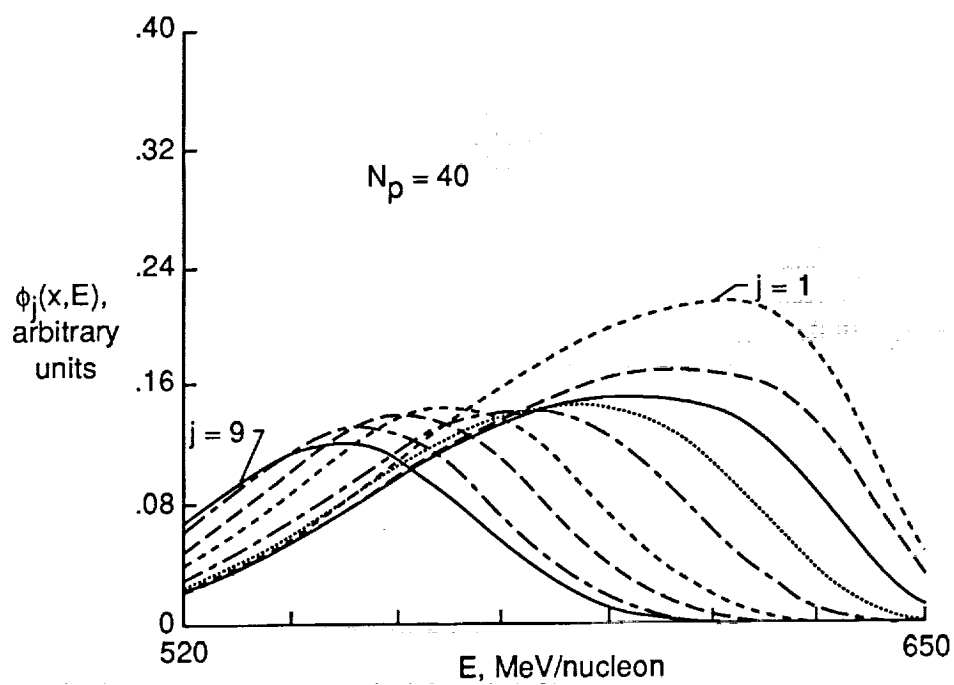


(b) $\Delta s = 6.414$.

Figure 27. Flux profile comparison with finite-difference calculation for an incident ($J = 10$) neon beam of $E_o = 670$ MeV/nucleon.

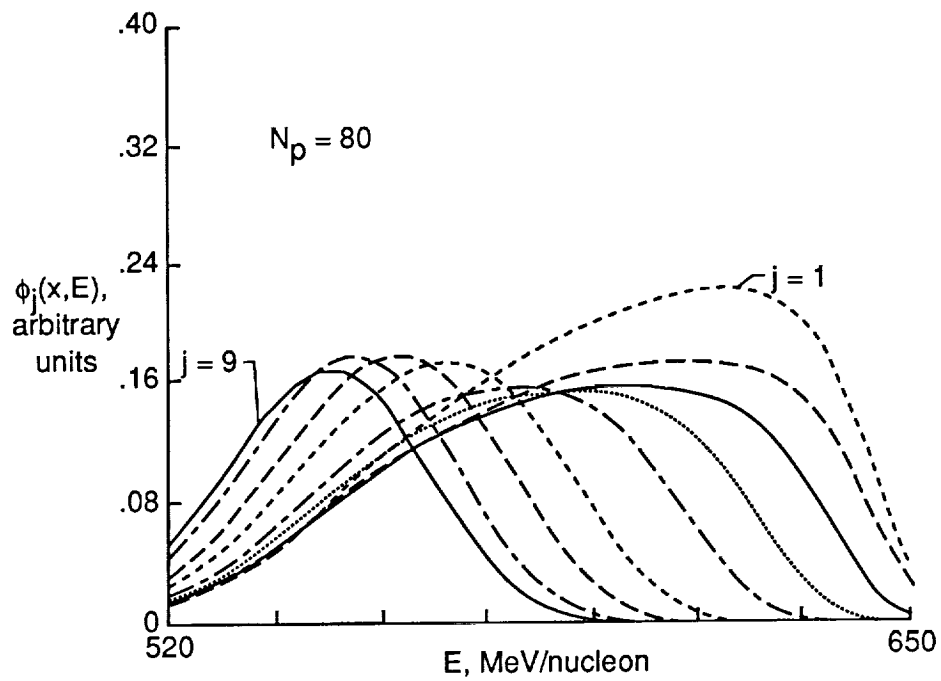


(c) $\Delta s = 3.207$.

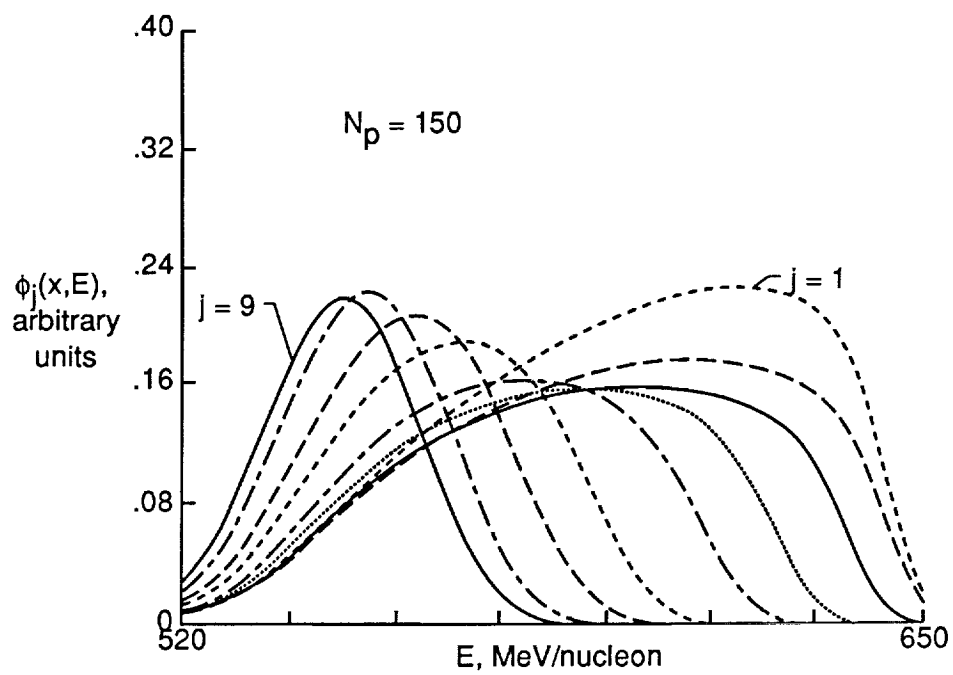


(d) $\Delta s = 1.604$.

Figure 27. Continued.

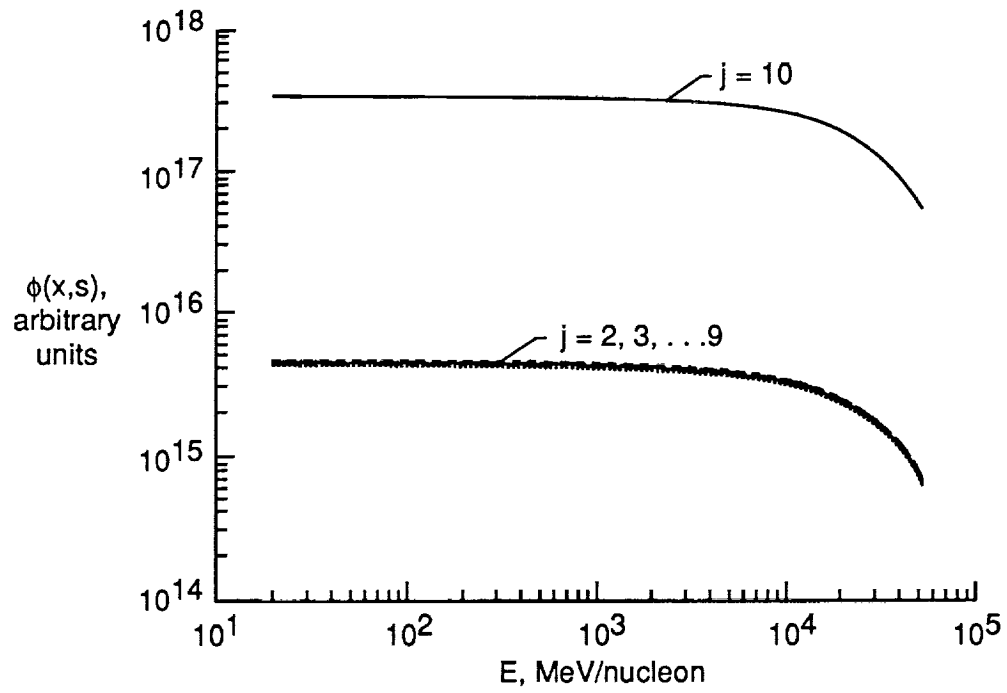


(e) $\Delta s = 0.802$.

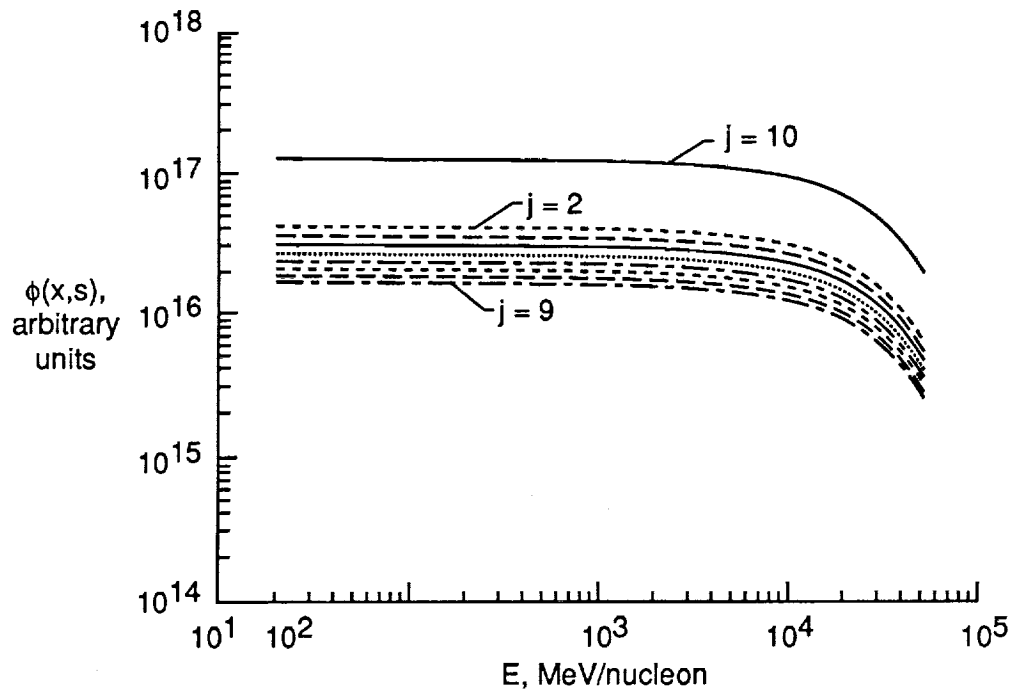


(f) $\Delta s = 0.428$.

Figure 27. Concluded.

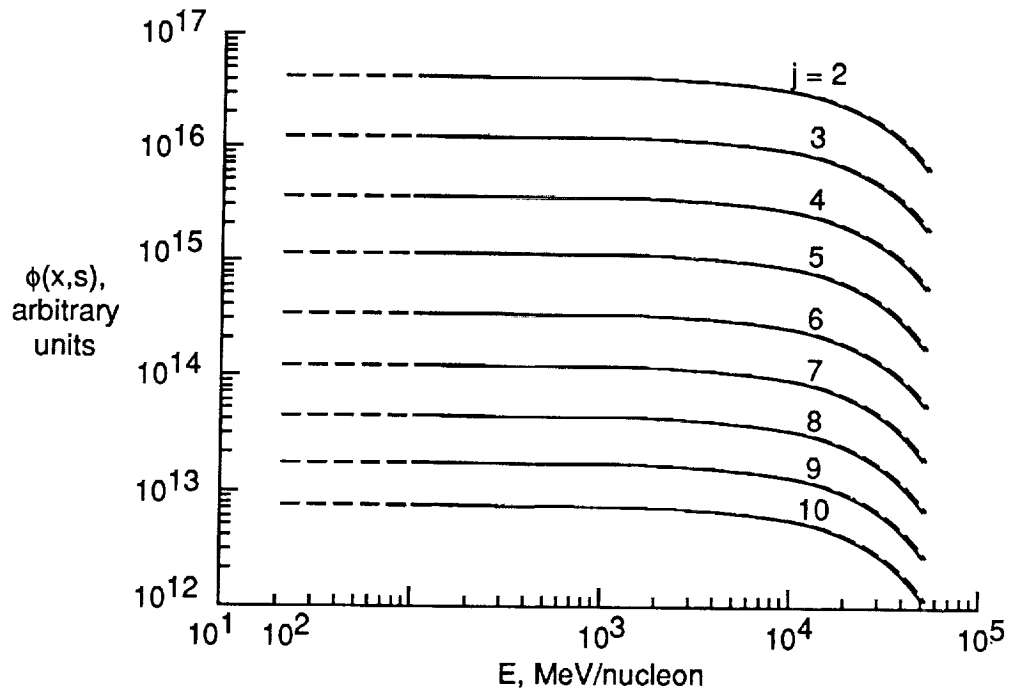


(a) 1 g/cm^2 .

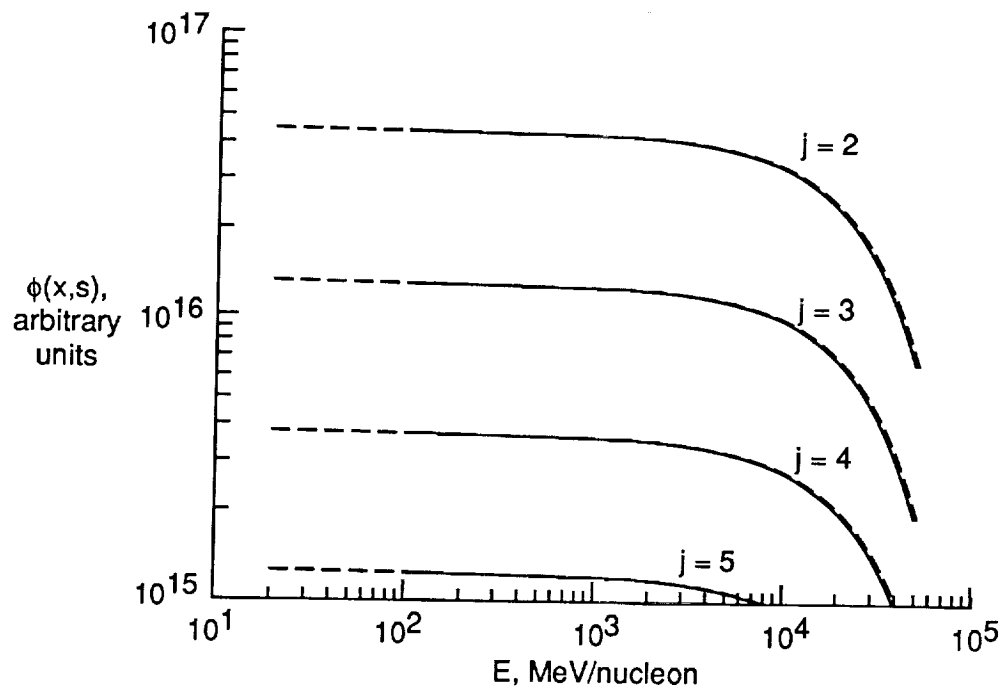


(b) 10 g/cm^2 .

Figure 28. Flux profile comparison with finite-difference solution for incident neon ($J = 10$) ions at $E_0 = 100 \text{ GeV/nucleon}$.



(c) 100 g/cm^2 .



(d) $j = 2, 3, 4, 5$ at 100 g/cm^2 .

Figure 28. Concluded.

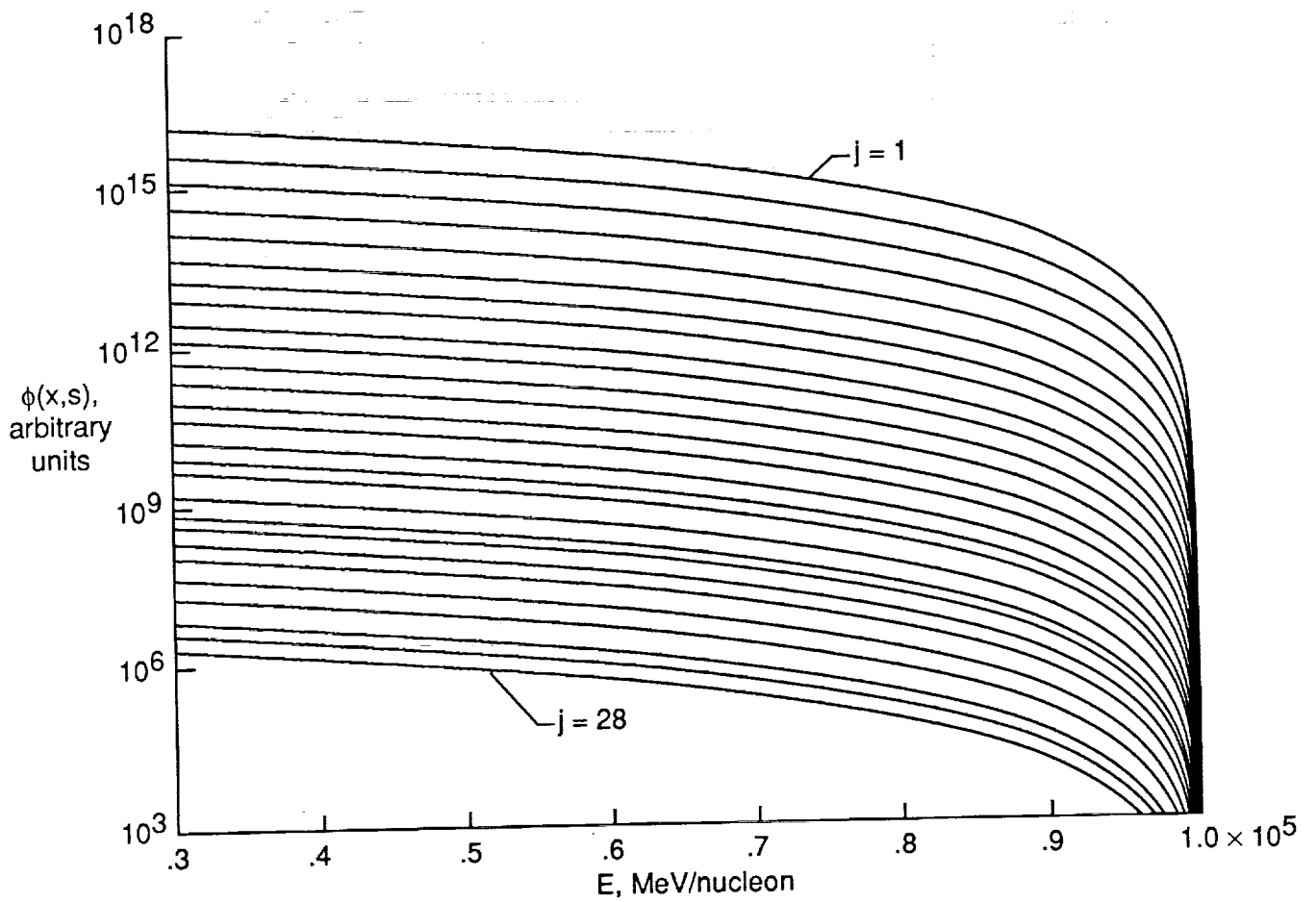


Figure 29. Flux profile comparison with finite-difference solution for incident nickel ($J = 28$) ions at $E_o = 100$ GeV/nucleon and 100 g/cm^2 .

REPORT DOCUMENTATION PAGE			Form Approved OMB No. 0704-0188	
Public reporting burden for this collection of information is estimated to average 1 hour per response, including the time for reviewing instructions, searching existing data sources, gathering and maintaining the data needed, and completing and reviewing the collection of information. Send comments regarding this burden estimate or any other aspect of this collection of information, including suggestions for reducing this burden, to Washington Headquarters Services, Directorate for Information Operations and Reports, 1215 Jefferson Davis Highway, Suite 1204, Arlington, VA 22202-4302, and to the Office of Management and Budget, Paperwork Reduction Project (0704-0188), Washington, DC 20503.				
1. AGENCY USE ONLY(Leave blank)	2. REPORT DATE October 1991	3. REPORT TYPE AND DATES COVERED Technical Paper		
4. TITLE AND SUBTITLE Benchmark Solutions for the Galactic Heavy-Ion Transport Equations With Energy and Spatial Coupling		5. FUNDING NUMBERS WU 199-04-16-11		
6. AUTHOR(S) Barry D. Ganapol, Lawrence W. Townsend, Stanley L. Lamkin, and John W. Wilson				
7. PERFORMING ORGANIZATION NAME(S) AND ADDRESS(ES) NASA Langley Research Center Hampton, VA 23665-5225		8. PERFORMING ORGANIZATION REPORT NUMBER L-16909		
9. SPONSORING/MONITORING AGENCY NAME(S) AND ADDRESS(ES) National Aeronautics and Space Administration Washington, DC 20546-0001		10. SPONSORING/MONITORING AGENCY REPORT NUMBER NASA TP-3112		
11. SUPPLEMENTARY NOTES Barry D. Ganapol: University of Arizona, Tucson, AZ; Lawrence W. Townsend and John W. Wilson: Langley Research Center, Hampton, VA; Stanley L. Lamkin: Old Dominion University, Norfolk, VA.				
12a. DISTRIBUTION/AVAILABILITY STATEMENT Unclassified-Unlimited Subject Category 70		12b. DISTRIBUTION CODE		
13. ABSTRACT (Maximum 200 words) Nontrivial benchmark solutions are developed for the galactic heavy-ion transport equations in the straight-ahead approximation with energy and spatial coupling. Analytical representations of the ion fluxes are obtained for a variety of sources with the assumption that the nuclear interaction parameters are energy independent. The method utilizes an analytical Laplace transform inversion to yield a closed-form representation that is computationally efficient. The flux profiles are then used to predict ion dose profiles, which are important for shield-design studies.				
14. SUBJECT TERMS Benchmark solutions; Space radiation; Heavy-ion transport			15. NUMBER OF PAGES 55	
			16. PRICE CODE A04	
17. SECURITY CLASSIFICATION OF REPORT Unclassified	18. SECURITY CLASSIFICATION OF THIS PAGE Unclassified	19. SECURITY CLASSIFICATION OF ABSTRACT	20. LIMITATION OF ABSTRACT	

NSN 7540-01-280-5500

Standard Form 298 (Rev. 2-89)
Prescribed by ANSI Std. Z39-18
298-102

